A STUDY OF THE PRODUCTION OF MASSIVE MUON PAIRS IN 225 GeV π^--NUCLEUS COLLISIONS

BY

HERBERT B. GREENLEE

JUNE, 1985

THE UNIVERSITY OF CHICAGO

A STUDY OF THE PRODUCTION OF MASSIVE MUON PAIRS IN 225 GEV π^--NUCLEUS COLLISIONS

A DISSERTATION SUBMITTED TO
THE FACULTY OF THE DIVISION OF THE PHYSICAL SCIENCES
IN CANDIDACY FOR THE DEGREE OF
DOCTOR OF PHILOSOPHY

DEPARTMENT OF PHYSICS

BY
HERBERT B. GREENLEE

CHICAGO, ILLINOIS
JUNE, 1985

ACKNOWLEDGMENTS

It is a pleasure to thank all of the people whose efforts have contributed to the research that is reported in this thesis and to my education. I thank my collaborators: Henry Frisch, Carla Grosso-Pilcher, Kurtis Johnson, Mac Mestayer, Pierre Piroué, Bernard Pope, Lindsay Schachinger, Mel Shochet, David Stickland, Dick Sumner and Morris Swartz. I also thank Nikos Giokaris, Jim Green, Chuck Whitmer, Gail Hansen and Ryan Rohm who worked with the group at various times. I especially thank Mel Shochet, my thesis sponsor, for his guidance and support, for many helpful suggestions, and for carefully reading this thesis.

I thank Dick Armstrong and the EFI Engineering Services Group, Harold Sanders and the EFI Electronics Development Group and the staff of the Princeton Elementary Particles Laboratory for their help in the design and construction of the apparatus. I also thank the staff of the Fermilab Proton Department for their help in the construction of the apparatus and the operation of the P-West beamline.

TABLE OF CONTENTS

LIST OF TABLES

LIST OF FIGURES

ABSTRACT

This thesis reports the results of an experiment to measure the differential cross section for the production of massive muon pairs in 225 GeV/c π^--nucleus collisions. Furthermore, we have interpreted this cross section in terms of the Drell-Yan quark-antiquark annihilation model in the mass continua between the ψ and Υ family of vector meson resonances (defined as 4.5 GeV/c^2<M<8.5 GeV/c^2) and above the Υ (defined as M>11 GeV/c^2).

We have measured the structure function of the pion and the K-factor in the ψ to Υ mass continuum. Our results are consistent with previous experiments.

We have compared our measurement of the high mass differential cross section with the predictions of the Drell-Yan model using structure functions measured in the ψ to Υ continuum. We find that the high mass cross section is consistent with the Drell-Yan model provided that QCD leading log M^2-evolution is included in the structure functions.

Finally, we have measured the transverse momentum dependence of the differential cross section and have reported mean values of p_T and p_T^2 in several mass ranges.

CHAPTER I

INTRODUCTION

Each of the hundreds of elementary particles that are currently known can be placed into one of the following categories: hadrons, leptons and gauge bosons. Of these, the hadrons are by far the most numerous and the least well understood. The complexity of the spectrum and interactions of hadrons is attributed to the fact that hadrons are composite, whereas leptons and gauge bosons are elementary at the current limits of resolution. Our understanding of the hadronic bound state, though incomplete, is nevertheless considerable. The basis of this understanding is the quark/parton model of hadrons.

The Quark Model

In 1964 Gell-Mann and Zweig proposed the quark model of hadrons as a means of explaining the hadron spectrum.[1] The quark model asserts that hadrons are composed of particles which Gell-Mann called quarks. Quarks are spin 1/2 fermions. They carry a charge of either +2/3 or -1/3 and a baryon number of 1/3. Baryons are composed of three quarks. Mesons are composed of a quark-antiquark pair. Just three kinds (flavors) of quarks were needed to account for all of the hadrons known in 1964. Today, five flavors of quarks are known, a sixth is likely and more are possible. The names and quantum numbers of the quarks are listed in Table 1.

In addition to flavor and charge quantum numbers, quarks carry an additional quantum number called color. The color degree of freedom is necessary to prevent the quarks in certain baryons from violating the Pauli exclusion principle. For example, were it not for color, the wave function of the Δ^{++}, which is composed of three up quarks, would be totally symmetric, in violation of Dirac statistics. Quarks come in three colors (e.g. red, green and blue by analogy with

the primary colors). In all known hadrons, the colors of the constituent quarks add up to zero (i.e. white).

The quark model was reasonably successful in explaining the spectrum and static properties of hadrons, but it is not a dynamical theory. The quark model says little about the interactions of hadrons or about what holds quarks together. The biggest problem with the quark model, however, is the fact that no quark has ever been directly observed.

The Parton Model

Another view of hadron structure comes from the parton model of Bjorken and Feynman.[2] The parton model was developed to explain the results of deep inelastic electron-nucleon scattering experiments at SLAC in the late 1960's. The cross section for electron-nucleon scattering can be written in the following general form in the single photon exchange approximation.

$$\frac{d^2\sigma}{d\nu dQ^2} = \frac{4\pi\alpha^2}{Q^4}\,\frac{E'}{E}\left[2W_1(\nu,Q^2)\sin^2\frac{\theta}{2} + W_2(\nu,Q^2)\cos^2\frac{\theta}{2}\right] \qquad \text{(I.1)}$$

The variables in this equation are as follows: $\alpha = 1/137$ is the fine structure constant; E is the laboratory energy of the incident electron; E' is the laboratory energy of the scattered electron; θ is the laboratory scattering angle of the electron; $Q^2 = 4EE'\sin^2\theta/2$ is the absolute value of the four momentum transfer squared; $\nu = E\text{–}E'$ is the energy loss of the electron in the laboratory; W_1 and W_2 are called structure functions. A complete theory of hadron structure and interactions would predict the dependence of W_1 and W_2 on ν and Q^2. No such theory exists.

The SLAC experiments[3] found the surprising result that at large ν and Q^2 νW_2 depended only on the ratio Q^2/ν. This phenomenon was predicted by Bjorken and is known as Bjorken scaling.[4] Bjorken scaling can be explained by assuming that the incident electrons scatter elastically off of pointlike, on-shell, spin 1/2 nucleon constituents called partons. Specifically, the parton model predicts that

$$\nu W_2(\nu,Q^2) = \sum_i e_i^2 f_i(x) \qquad \text{(I.2)}$$

and

$$2xmW_1(\nu,Q^2) = \nu W_2(\nu,Q^2) \tag{I.3}$$

where

$$x = \frac{Q^2}{2m\nu} \tag{I.4}$$

and m is the mass of the target nucleon. The variable x can be interpreted as the fraction of the nucleon momentum carried by the struck quark. Equation I.3 is called the Callan-Gross relation and is characteristic of spin 1/2 partons.[5] It has been verified by experiment.[6] The functions $f_i(x)$ are called parton density functions or structure functions for the flavor i. (Thus the term structure function describes both $f_i(x)$ and $W_1(\nu,Q^2)$ and $W_2(\nu,Q^2)$.) $f_i(x)/x$ is the probability of finding a parton of flavor i with momentum fraction x.

The Quark/Parton Model

It is natural and logical to identify partons with quarks. Since the early SLAC experiments, many elementary particle reactions have been studied within the framework of the quark/parton model.[7] Chief among these are reactions involving leptons and hadrons, including muon and neutrino deep inelastic scattering, electron-positron annihilation into hadrons and the Drell-Yan process (see below). The experimental results from each of these reactions supports the quark/parton model.

In neutrino deep inelastic scattering, the signatures for the various neutrino-quark and antineutrino-quark subprocesses differ to the extent that it is possible to disentangle the contributions of the various elementary subprocesses to the total reaction. Neutrino deep inelastic scattering provides the most detailed information about nucleon constituents currently available.

The total cross section for electron-positron annihilation is sensitive to the number and charges of quarks. The fact that there are three colors of quarks is reflected in the total cross section. Hadron jets, which were first observed in electron-positron annihilation, provide qualitative evidence for the existence of quarks in the final state.

The Drell-Yan Model

Soon after the initial success of the parton model, Drell and Yan realized that parton model ideas could be applied to the reaction that is now called the Drell-Yan process,[8] namely the production of large invariant mass lepton pairs via the electromagnetic annihilation of a quark-antiquark pair in hadronic collisions.

$$h_a + h_b \rightarrow l^+l^- + \text{anything}$$

The lowest order Feynman diagram for this reaction is shown in Figure 1.

In deep inelastic scattering the final state lepton is characterized by two non-trivial variables (e.g. ν and Q^2). In dilepton production five non-trivial variables are required to specify the final state leptons. In both cases there is also a trivial overall azimuthal angle. This means that one can obtain information from the Drell-Yan process that can not be obtained from deep inelastic scattering.

The invariant mass and longitudinal momentum of the lepton pair contain information about the longitudinal momenta of the annihilating quark and antiquark. The longitudinal momentum of the lepton pair is conventionally measured using a dimensionless variable called Feynman x.

$$x_F = \frac{2p_L^*}{\sqrt{s}} \tag{I.5}$$

where p_L^* refers to the longitudinal momentum of the pair in the hadron center of mass and s is the center of mass energy squared. There is also a dimensionless variable defined for the invariant mass, M, of the lepton pair:

$$\tau = \frac{M^2}{s} \tag{I.6}$$

There is a second pair of dimensionless variables, x_1 and x_2, which are related to τ and x_F as follows:

$$x_1 x_2 = \tau \tag{I.7}$$

$$x_1 - x_2 = x_F \tag{I.8}$$

or

$$x_1 = \frac{1}{2}(x_F + \sqrt{x_F^2 + 4\tau}) \tag{I.9}$$

$$x_2 = \frac{1}{2}(-x_F + \sqrt{x_F^2 + 4\tau}) \tag{I.10}$$

The variables x_1 and x_2 can be interpreted as the fraction of the nucleon's longitudinal momentum carried by the annihilating quarks from the beam and target hadrons respectively.

Two angular variables, $\cos\theta$ and ϕ, specify the direction of the negative lepton in the dilepton center of mass frame. These angles are measured relative to a set of coordinate axes which depend only on the hadron momenta. Various definitions of coordinate axes have been proposed in the literature.[9] They all have two things in common. The z axis is chosen to approximate the direction of the annihilating quarks and the hadrons lie in the xz plane. Note that the xz plane and therefore ϕ is undefined if the transverse momentum of the lepton pair is zero.

The magnitude and azimuth of the transverse momentum of the pair, p_T and ϕ_T, complete the set of kinematic variables.

A straightforward application of parton model ideas yields the following cross section for hadronic dilepton production.[8]

$$\frac{d^2\sigma}{dMdx_F} = \frac{8\pi\alpha^2}{9M^3(x_1 + x_2)} \sum_i e_i^2 \Big[f_i^a(x_1) f_{\bar{i}}^b(x_2) + f_{\bar{i}}^a(x_1) f_i^b(x_2) \Big] \tag{I.11}$$

The sum is over quark flavors. The superscripts on the quark densities refer to the hadron from which the quark comes. The factor in front of the sum includes the cross section for the annihilation of two pointlike, spin 1/2, unit charge fermions into muons (i.e. $\sigma_0 = 4\pi\alpha^2/3M^2$). The sum over structure functions is the probability for finding two quarks with momentum fractions x_1 and x_2. Equation I.11 also includes a factor of 1/3 for color.

The angular dependence of the cross section is predicted to be

$$\frac{d\sigma}{d(\cos\theta)} \propto (1 + \cos^2\theta) \tag{I.12}$$

This angular distribution corresponds to a transversely polarized spin 1

intermediate state.

If the parton densities are known, the Drell-Yan formula predicts the cross section without any free parameters and therefore provides an unambiguous test of the parton model. Alternatively, the Drell-Yan formula provides a way of measuring parton densities in unstable hadrons, such as pions and kaons, which can not be measured in deep inelastic scattering.

At this point it is useful to consider in detail the specific reaction which is the subject of this document,

$$\pi^- + N \rightarrow \mu^+\mu^- + \text{anything}$$

Here N stands for a nucleon in a heavy nuclear target (the experiment used tungsten).

It is conventional to separate quark densities into "valence" and "sea" distributions. Valence quarks determine the quantum numbers of a hadron. Sea quarks are virtual quark-antiquark pairs. In our experiment, we are not able to separate valence and sea distributions since we used only one type of beam particle. We must therefore make a number of assumptions to enable us to extract quark densities. We assume that the valence and sea quark densities of the pion and nucleon are isospin and charge invariant. In the absence of information to the contrary we assume that the strange sea of the pion is equal to the up and down sea. The contribution of charm and heavier flavors to the pion and nucleon sea is assumed to be negligible. We make the following definitions:

Pion valence structure function:

$$V^\pi(x) = f_{\bar{u}}^\pi(x) - f_u^\pi(x) = f_d^\pi(x) - f_{\bar{d}}^\pi(x) \tag{I.13}$$

Pion sea structure function:

$$S^\pi(x) = f_u^\pi(x) = f_{\bar{d}}^\pi(x) = f_s^\pi(x) = f_{\bar{s}}^\pi(x) \tag{I.14}$$

Nucleon valence structure functions:

$$U(x) = f_u^p(x) - f_{\bar{u}}^p(x) = f_d^n(x) - f_{\bar{d}}^n(x) \tag{I.15}$$

$$D(x) = f_d^p(x) - f_{\bar{d}}^p(x) = f_u^n(x) - f_{\bar{u}}^n(x) \tag{I.16}$$

Nucleon up and down sea structure function:

$$S^N(x) = f_{\bar{u}}^p(x) = f_{\bar{d}}^p(x) = f_{\bar{u}}^n(x) = f_{\bar{d}}^n(x) \tag{I.17}$$

Nucleon strange sea structure function:

$$\lambda(x) = f_s^p(x) = f_{\bar{s}}^p(x) = f_s^n(x) = f_{\bar{s}}^n(x) \tag{I.18}$$

The valence quark densities are subject to the following sum rules.

$$\int_0^1 \frac{V^\pi(x)}{x}\, dx = 1 \tag{I.19}$$

$$\int_0^1 \frac{U(x)}{x}\, dx = 2 \tag{I.20}$$

$$\int_0^1 \frac{D(x)}{x}\, dx = 1 \tag{I.21}$$

The Drell-Yan formula can now be written as follows.

$$\frac{d^2\sigma}{dM dx_F} = \frac{8\pi\alpha^2}{9M^3(x_1 + x_2)}[\, V^\pi(x_1)\, G(x_2) + S^\pi(x_1)\, H(x_2)\,] \tag{I.22}$$

where

$$G(x) = \frac{1}{9}[\, 1.6\, U(x) + 2.4\, D(x) + 5\, S^N(x)\,] \tag{I.23}$$

$$H(x) = \frac{1}{9}[\, 2.2\, U(x) + 2.8\, D(x) + 10\, S^N(x) + 2\, \lambda(x)\,] \tag{I.24}$$

We have assumed Z/A=.4 where Z and A are respectively the atomic number and atomic weight of the target.

The Drell-Yan formula is successful in explaining a number of features of the data.[10] The rapid fall-off of the cross section with increasing mass which is characteristic of the photon propagator is observed. Nucleon parton densities extracted from muon pair data agree with those measured in deep inelastic scattering. The angular distribution of equation I.12 is observed. The electromagnetic charge asymmetry predicted by equation I.11 is observed. The valence $\bar{u}$ antiquark of the π^- has twice the charge of the valence $\bar{d}$ antiquark of the π^+. Therefore, at high mass where the

annihilation of valence quarks and antiquarks dominates, the ratio of π^- to π^+ induced Drell-Yan production approaches the value four.

There are, however, two outstanding features of the data which are not accounted for by equation I.11. The first discrepancy is the fact that lepton pairs are observed to be produced with substantial transverse momentum. The original ("naive") Drell-Yan model has no mechanism by which the final state leptons may acquire transverse momentum over and above the intrinsic transverse momentum of the annihilating quarks. The intrinsic transverse momentum of the quarks is expected to be in the neighborhood of 300 MeV/c independent of hadron momentum. What is observed is that lepton pairs are produced with a mean transverse momentum substantially larger than $\sqrt{2} \times$ 300 MeV/c and that the mean transverse momentum increases with increasing hadron energy. Mean transverse momenta of about 1 GeV/c are typical at Fermilab and CERN energies. The second major discrepancy is the overall normalization of the cross section. The ratio of the measured cross section to the cross section predicted by the Drell-Yan model is called the K-factor. The K-factor is measured to be approximately 2 (with large systematic errors) almost independent of the kinematic variables.

Quantum Chromodynamics

It is likely that the failures of the Drell-Yan model are due to its failure to include strong interaction corrections. The only reasonable candidate theory of the strong interactions is Quantum Chromodynamics (QCD). QCD is the non-Abelian gauge theory based on the symmetry group SU(3) of color. QCD treats the color quantum number of quarks as a dynamical charge. The color force is transmitted by eight massless vector gauge bosons called gluons, which are analogous to the photon in QED. The gluons differ from the photon in that they themselves are colored, whereas the photon is electrically neutral. Figure 2 shows Feynman diagrams for several QCD sub-processes that contribute to the Drell-Yan process.

In order to make predictions from QCD using perturbation theory, it is necessary that the strong coupling constant, α_s, be small. It is possible to

meet this condition because the strong coupling constant is not really a constant at all. Its value depends on the distance/momentum scale at which it is measured. QCD is said to possess a running coupling constant. Leading order perturbation theory predicts the following dependence of α_s on the momentum scale, Q^2, at which it is measured, for large Q^2.

$$\alpha_s(Q^2) = \frac{12\pi}{(33-2n_f)\ln(Q^2/\Lambda^2)} \tag{I.25}$$

where n_f is the number of excited quark flavors and Λ is the QCD scale parameter. One sees from equation I.25 that as Q^2 goes to infinity, $\alpha_s(Q^2)$ tends to zero. This fact is known as asymptotic freedom.

Asymptotic freedom accounts for the success of the parton model. The smallness of $\alpha_s(Q^2)$ at large Q^2 explains why quarks behave as if they are nearly free in large momentum transfer reactions involving leptons. On the other hand, the fact that $\alpha_s(Q^2)$ grows at large distances (low Q^2) may explain why no quark has ever been liberated from a hadron. There is a hypothesis called color confinement which states that infinite energy is required to remove a quark from a hadron. Color confinement has not been proved. In fact, little is known about the long distance/low energy limit of QCD (including the structure of hadronic bound states) due to the extreme mathematical difficulty of the theory when α_s is large. In the short distance/high energy limit, however, there is hope that perturbation theory can be used to make reliable predictions.

There is no really clean test of QCD because experiments are not able to observe quarks and gluons directly. The current strategy for testing QCD is to "factorize" cross sections into "hard" and "soft" pieces. The hard piece consists of perturbatively calculable scattering subprocesses involving quarks and gluons. The soft piece consists of phenomenological quark and gluon densities that describe the distribution of partons in initial state hadrons and fragmentation functions that describe how final state partons evolve into hadron jets.

Despite an appealing physical motivation and despite the success of the parton model, it is not intuitively obvious that factorization is valid in QCD.

For a while, factorization was the subject of a theoretical controversy. Bodwin, Brodsky and Lepage pointed out that initial state interactions over long distance and time scales could induce correlations between the wave functions of the incoming hadrons and spoil factorization in the Drell-Yan process.[11] Recently, however, Collins, Soper and Sterman have proved the validity of factorization in the Drell-Yan process to all orders in perturbation theory.[12]

If factorization is valid, then the Drell-Yan cross section can be calculated as a perturbation series in $\alpha_s(M^2)$. (M^2 plays the role of the momentum scale in the Drell-Yan process.)

$$\sigma = A_0 + \alpha_s(M^2)A_1 + \alpha_s^2(M^2)A_2 + \cdots \tag{I.26}$$

Furthermore, at each order in perturbation theory, the coefficient of $\alpha_s^n(M^2)$ can be expanded in a series of logarithms of the large number M^2/Λ^2.

$$A_n = B_{n,n}\ln^n(M^2/\Lambda^2) + B_{n,n-1}\ln^{n-1}(M^2/\Lambda^2) + \cdots \tag{I.27}$$

These large logarithms physically correspond to multiple hard collinear gluon radiation. It can be seen from equation I.25 that the large logarithm, $\ln(M^2/\Lambda^2)$ is proportional to $1/\alpha_s(M^2)$. Thus, to take into account all terms which are proportional to any given power of $\alpha_s(M^2)$ requires summing over an infinite number of terms of the perturbation series. In the so-called leading log approximation (LLA) one retains only the largest power of $\ln(M^2/\Lambda^2)$ at each order in perturbation theory (i.e. those terms that contain zero powers of $\alpha_s(M^2)$). The leading log approximation leads to the remarkable result that the naive Drell-Yan cross section is unmodified except that the quark densities acquire a calculable M^2-dependence that violates scaling.[13] Furthermore, the M^2-dependence of the Drell-Yan quark densities is the same as the Q^2-dependence of the quark densities in deep inelastic scattering.

$$\left[\frac{d\sigma}{dMdx_F}\right]_{LLA} = \frac{8\pi\alpha^2}{9M^3(x_1+x_2)}$$

$$\times \sum_i e_i^2\left[f_i^a(x_1,M^2)f_{\bar{i}}^b(x_2,M^2) + f_{\bar{i}}^a(x_1,M^2)f_i^b(x_2,M^2)\right] \quad \text{(I.28)}$$

The actual form of the M^2-dependence of the structure functions is given to first order by the Alterelli-Parisi equations.[14]

The next to leading log ($O(\alpha_s)$) terms are large. Their main effect at experimentally accessible values of τ and x_F is to change the overall normalization of the Drell-Yan cross section by a factor (the theoretical K-factor) of 1.6.[15] It has been argued that the largest contributions to the K-factor are the first term in an exponential power series.[16] If this is true, then QCD predicts a K-factor of about 1.9, in rough agreement with experiment.

QCD accounts reasonably well for the p_T integrated Drell-Yan cross section. QCD retains the successes of the naive Drell-Yan model and provides an explanation for the K-factor. QCD has also been used to try to account for the measured p_T spectrum in Drell-Yan production. Unlike the naive Drell-Yan model, QCD allows Drell-Yan pairs to acquire transverse momentum by recoiling against gluons.

First order QCD calculations predict effects that are qualitatively similar to those observed in the data.[17] In particular, first order QCD predicts the existence of a high-p_T tail in the cross section and the growth of mean p_T with energy. However, first order QCD does not satisfactorily account for the data quantitatively.[18] The QCD prediction for the cross section diverges at p_T=0, but it can be regularized by convoluting it with an intrinsic quark p_T-distribution. One problem is that unreasonably large values of mean intrinsic p_T ($<p_T^2>\sim 1(\mathrm{GeV/c})^2$) are required to fit the pion data. Another problem is that even after regularization, the theory underestimates the normalization of the pion data at high p_T by a factor of about 2. With respect to the latter problem, it appears that second order QCD renormalizes the first order prediction by a factor (called K') of about 2.[19] This is analogous to the way first order QCD renormalizes the p_T-integrated prediction

by the K-factor.

There is a fundamental difficulty in applying QCD to the problem of the Drell-Yan p_T-spectrum. Perturbation theory is only applicable at very large p_T ($p_T \sim M$). When two large momentum scales are present (e.g. when $\Lambda \ll p_T \ll M$), large logarithms of the form $\ln(M^2/p_T^2)$ appear. These large logarithms generate large contributions at all orders in perturbation theory. Physically this corresponds to multiple soft gluon radiation. Much theoretical work has been in trying to sum the leading $\ln(M^2/p_T^2)$ contributions to all orders in perturbation theory.[20] Soft gluon predictions for the Drell-Yan p_T-spectrum appear to reproduce the data reasonably well with moderate values of mean intrinsic p_T,[21] although the problem is not yet completely solved.

The Experiment

This document reports a portion of the results of Fermilab experiment 326. The experiment has measured the production of muon pairs by 225 GeV/c negative pions incident on a tungsten target. The subject of this document is a measurement of the differential cross section for the above reaction in the high mass continuum region where the Drell-Yan process is the dominant production mechanism. We define the high mass continuum by the following cuts.

$$4.5 < M < 8.5 \text{ GeV/c}^2$$

$$M > 11 \text{ GeV/c}^2$$

These cuts are designed to eliminate the contribution of J/ψ and Υ vector meson production to the dimuon signal.

Chapter II describes the apparatus. Chapter III describes the primary analysis (i.e. the extraction of the dimuon signal). Chapter IV describes how the dimuon signal was converted into a differential cross section. Chapter V describes the interpretation of the differential cross section and presents the final results.

CHAPTER II

THE EXPERIMENT

The experiment was performed in the proton west high intensity area at Fermilab. An intense beam of negative pions with an energy of 225 GeV was focussed onto the experimental tungsten target. Muons produced in the target were detected by a solid steel magnetic spectrometer located downstream of the target. A diagram of the apparatus is shown in Figure 3.

The detector consisted of a steel collimator followed by seven solid steel toroidal magnets. There was a 20 mrad conical vacuum pipe down the middle of the apparatus. To be detected, muons were required to penetrate the collimator and at least four magnets. Other detectable secondaries were absorbed in the steel, or, together with the non-interacted beam, they went down the 20 mrad hole.

Following each of the seven magnets, there was a gap which was instrumented with a scintillation counter hodoscope (for triggering) and a set of drift chambers (for tracking). The muons' momentum was inferred from the magnetic bend as the muons traversed the magnets.

Viewed from the front (beam's eye view), the spectrometer had an eight-fold azimuthal symmetry. The eight octants were instrumented independently. To be detected, the muons from a muon pair were required to go into separate octants.

The Beam

The secondary beam consisted of negative hadrons (mainly pions) produced by the interaction of the 400 GeV/c primary proton beam with a one interaction length berylium production target. The secondary beamline collected and momentum analyzed forward produced hadrons and transported them 740 feet to

the experimental target (see Fig. 4). A more complete description of the secondary beamline can be found in Ref. 22.

The nominal momentum of the beam was 225 GeV/c. A Monte Carlo calculation yielded a mean momentum of 221 GeV/c with a FWHM of 20 GeV/c.[23] The spot size at the experimental target was typically .3" horizontal by .5" vertical (FWHM). In addition to negative pions, the beam contained approximately 5% negative kaons and less than 1% anti-protons.[24]

The beam was accompanied by a "halo" of muons, of both signs, arising from the decay of beam hadrons and from the decay of hadrons in the vicinity of the production target. A system of spoiler magnets reduced the flux of halo muons to about 1% of the beam flux. Special care had to be taken both in the trigger and in the analysis to minimize the effect of the halo muons.

The accelerator delivered beam in one second long spills about twelve seconds apart. Because of the RF used to accelerate the primary protons, the beam arrived in "RF buckets" less than two nanoseconds long and about 18 nsec apart. Typical intensities were 2×10^{12} primary protons per spill at the production target and 5×10^{8} pions at the experimental target.

Beam Monitors

A number of devices were used to monitor the primary and secondary beams. Segmented wire ionization chambers (SWIC's) measured the profiles of the primary and secondary beams at several points in the beamlines, including immediately upstream of the targets. The intensity of the primary proton beam was measured by a secondary emission monitor (SE700) located immediately upstream of the production target. The intensity of the secondary beam was measured by two ionization chambers (IC710 and IC711/712/713) located in front of the experimental target.

The electrodes of both ionization chambers were 4" diameter circles. The anode of IC711/712/713 was divided into a set of concentric rings which measured separately the pion flux within a radius of .25", from .25" to .5" and from .5" to 2.0". This enabled us to determine the fraction of the beam which hit the .5" radius target. Typically 90% of the beam hit the target. The absolute

normalization of the pion flux was obtained from IC710. The scale factor of this device was measured in a previous experiment. A detailed report of the measurement of the scale factor can be found in Ref. 22. Briefly, the scale factor was measured using four independent methods: counting of beam particles at low intensity, foil calibration using protons, foil calibration using pions and theoretical calculation. The four methods gave consistent results. The quoted error of the scale factor is $\pm 10\%$.

Finally, the pion beam which interacted in the experimental target was monitored by a scintillation counter telescope (called ME for monitor east) which viewed the experimental target at 90°. The output of ME, alone and in coincidence with the experimental livetime gate, was scaled. This information enabled us to correct the integrated pion flux for deadtime.

The Target

The data which are reported in this thesis were taken with a single tungsten target. The shape of the target was a cylinder 1.04" in diameter and 8.04" long. The target was composed of an alloy of 97% tungsten sintered in a copper-nickel matrix. The absorption length of this alloy is 4.63" and the radiation length is .15".

Collimator and Magnets

Immediately downstream of the target there was a 48" steel collimator. The front face of the collimator was 13.5" downstream of the center of the target. There was a 1.5" diameter cylindrical hole down the center of the collimator.

Behind the collimator were seven toroidal steel magnets. See Table 2 for the dimensions of these magnets. There was a 30 mrad conical hole down the center of the magnets inside of which was the 20 mrad conical vacuum pipe. The apex of the cones was located 7" downstream of the center of the target. The space between the magnets and the vacuum pipe was packed with lead shielding. The outer surfaces of the first two magnets were cylindrical. The outer surfaces of the last five magnets were octagonal. The octagonal magnets were originally part of the Brookhaven Cosmotron. All of the magnets were approximately 56" long

with about 12" between the magnets. The magnetic field in the magnets was approximately that of saturated iron (i.e. about 18 kG), producing a transverse momentum kick of about .75 GeV/c per magnet. The detailed shape of the magnetic field was calculated numerically from Maxwell's equations using the measured permeability of the steel. The total magnetic flux through the steel of each magnet was measured by integrating the voltage induced on a large induction loop as the magnet current was changed from forward to reverse. The agreement between the calculation and the measurements was better than 2%.

Trigger Scintillators

The apparatus was instrumented with 272 trigger scintillation counters (34 per octant). These counters were arranged in hodoscopes placed in the gap behind each of the seven magnets. Each hodoscope was segmented azimuthally into octants and radially within each octant. Each octant and gap position contained from 4 to 7 counters. Figure 5 shows the gap 3 trigger hodoscope. Table 3 gives the dimensions of the counters in each gap. The counters were constructed out of .25" thick NE 110 plastic scintillator. Light was collected by lucite light guides optically coupled to the scintillator and an Amperex 2232B or 56AVP photomultiplier tube. The high voltage to each tube was adjusted to produce a signal of 75 mV from a Co^{60} source.

Trigger

The task of the trigger was to indicate when target produced muons had penetrated through at least four magnets in each of two octants. This task was made difficult by the presence of halo muons. Target muons and halo muons populated different regions of phase space. Halo muons were nearly always almost parallel to the beam axis and need not have gone close to the target while target muons could only be accepted if they were produced at angles in excess of about 30 mrad. The trigger was designed to be efficient only in regions of phase space populated by target muons.

A functional block diagram of the trigger is shown in Figure 6. The trigger logic was organized into two levels. Each level decided whether there was a

target muon in at least two octants. The two levels differed in speed and level of sophistication. A detailed description of the trigger can be found in Ref. 25.

Signals coming from each of the photomultipliers were discriminated against a 30 mV threshold and reshaped into a 10 nsec wide logic pulse. The resulting signals were fanned out three ways. One signal was sent to a set of multiplexed scalers. The second signal was stored in a 100 nsec delay line to await the decision of the first level trigger logic. The third signal went to the first level trigger.

The first level trigger logic consisted of three fast coincidence matrices called M_{12}, M_{23} and M_4 in each octant followed by the so-called post matrix logic (PML). Figures 7 and 8 are diagrams of the matrices and PML respectively. The purpose of the coincidence matrices was to identify target muons in each octant. M_{12} formed coincidences between counters in gap 1 and gap 2. Each matrix point could arbitrarily be turned on or off, but ordinarily only those points populated by target muons were turned on. Likewise M_{23} formed coincidences between counters in gap 2 and gap 3. M_4 formed coincidences between counters in gap 4 and a logical "true" with all coincidence points allowed. Signals from each of the 24 matrices went to the PML. In the PML, the M_{12}, M_{23} and M_4 signals were placed in coincidence to create a single matrix signal for each octant. This "matrix AND" represented the first level trigger's estimate of whether there was a target muon in a given octant. The eight matrix signals were combined to form an eight bit address for a programmable 256 by 1 bit lookup table. Logical 1's were normally loaded into addresses which corresponded to two or more octants with muons. For 38% of the data, all octant pairs were allowed by the PML. For the rest of the data, the three hottest adjacent octant pairs were excluded. This allowed us to significantly reduce our trigger rate without affecting our high mass acceptance. A true output from the PML constituted a first level trigger. The first level trigger was pipelined so that it could make a decision whether to trigger or not for every RF bucket without any deadtime.

Three things happened when a first level trigger occurred. First, the counter signals which had been stored in the 100 nsec delay lines were latched. This latch information was used by the second level trigger and was read out with each event. Second, the first level trigger was sent to the drift chamber encoder

system via delay line. This caused the drift chamber information to be frozen while the second level trigger was engaged. Third, the first level trigger caused the second level trigger to be invoked.

The second level trigger consisted of the trigger processor and final decision logic (FDL). A diagram of the second level trigger is shown in Figure 9. The trigger processor compared the actual pattern of struck counters in each octant with a Monte Carlo generated list of 310 patterns that were consistent with the propagation of a target produced muon. Extra counters were allowed. In addition to deciding whether there was a muon in each octant, the trigger processor also determined the most probable sign of the muon. Trigger processor information from each octant was sent to the FDL which required matches in at least two octants. Most of the time, the FDL was programmed to reject muon pairs with the same charge. The second level trigger took 15 μsec to reach a decision, during which time the detector was dead. The second level trigger was typically invoked 10,000 times per spill, producing a 15% deadtime. If the FDL was satisfied, it interrupted the on-line computer and the event was read out. Otherwise, the FDL sent a fast reset to the rest of the detector electronics and data-taking was resumed.

Drift chambers

The detector was instrumented with 120 drift chambers containing 3616 sense wires for the precise measurement of muon trajectories. The drift chambers were of two different designs. 112 of the chambers were part of the original detector design. Two of these were upstream of the trigger counters in each octant and gap position. In gaps 2-7, the wires in the upstream chamber were perpendicular to the octant bisector. These chambers were known as X chambers. The downstream chambers in each octant were called U chambers and had their wires inclined at an angle of 100 mrad to the X wires. Information from the X and U chambers allowed us to reconstruct the muon's azimuthal coordinate. In gap 1 the order of the X and U chambers was reversed. In addition gap 1 had eight smaller X chambers which were added to improve the ability of the detector to take high rates. The 112 old chambers differed in their dimensions and number of sense wires (see Table 4) but used the same basic cell. The

basic cell was a 2" by .75" rectangular tube with a .001" diameter gold-plated tungsten sense wire running down its center. Each chamber contained two planes of cells offset by half of a cell to resolve left-right ambiguity (see Fig. 10). The long sides of each cell were aluminum planes which were held at ground. The short sides of each cell were aluminum I-beams which acted as cathodes for the cell. The I-beams were insulated from the ground planes by G10 strips and were held at a potential of -1200 volts. The sense wires were held at a potential of 2300 volts. The gas used was an equal mixture by volume of argon and ethane. The maximum drift time in a cell was .5 μsec.

The basic cell of the newer gap 1 chambers was a .25" stainless steel drift tube with the same kind of sense wire as the old chambers at its center. The drift tubes were stacked in two half-offset planes (see Fig. 11). The tubes were held at ground and the sense wires were held at 2400 volts. The gas was the same as in the old chambers. Unlike the old chambers, which met squarely and had a dead region at the octant boundary, the new chambers overlapped at the octant boundary. The new chambers were located upstream of the old chambers and covered only the inner 8" of gap 1.

Drift Chamber Readout

The drift chamber readout is described more completely elsewhere.[26] Here I will only give a summary.

Signals originating on the drift chamber sense wires were capacitively coupled inside the chambers to twisted pair transmission lines which carried the signals to the outside of the chamber. Amplifier/discriminator cards for the old chambers were mounted directly on the chamber frame. The amplifiers for the new chambers communicated with the chambers via 10 foot long coaxial cables. The amplifiers converted raw signals from the sense wires into 75 nsec long differential ECL logic pulses. These pulses were transmitted to the drift chamber encoder system via twisted pair ribbon cables.

The encoder system was basically a set of digital delay lines which kept a .625 μsec history of the hits for each wire in the system. These delay lines stored the presence or absence of a wire hit in time bins of half of an RF bucket (9

nsec). After each hit there was an encoder deadtime of between 75 and 150 nsec for that wire, which is similar to the amplifier deadtime.

The encoder system was frozen after every first level trigger (after a delay to allow for the maximum drift time). If the second level trigger subsequently rejected the event, the FDL generated a fast reset which would cause the drift chamber encoder system to resume the logging of drift chamber hits. If the second level trigger was satisfied with the event, the hits stored in the encoder system were read out and eventually written onto magnetic tape.

Data Acquisition

The experiment was controlled by a PDP-9 computer which communicated with the detector electronics using CAMAC. This computer was responsible for programming the trigger, reading in data from the detector and writing data onto magnetic tape. Each second level trigger generated a priority interrupt to the PDP-9. During the interrupt, the PDP-9 read out the fixed data for the event. The fixed data primarily consisted of the counter latch information and trigger processor information. The PDP-9 also instructed nine 8X300 microprocessors to begin a sparse data scan of the drift chamber hits stored in the drift chamber encoder system. Each microprocessor had access to the memory locations associated with up to 512 drift chamber wires. The microprocessors wrote hit information into a large buffer memory located next to the encoder electronics in the experimental hall. During idle time during and after a spill, the PDP-9 read hit information from the buffer memory and wrote it to magnetic tape. Computer deadtime was approximately 4 msec per event. A typical trigger rate of 50 per spill produced a deadtime of 20% (in addition to the typical trigger processor deadtime of 15%). At the end of each spill the PDP-9 also wrote spill information onto magnetic tape, including scalers and beam information obtained from the Fermilab control system (e.g. magnet currents and beam monitors).

Detector Inefficiencies

During the course of the analysis we found evidence that several pieces of the detector were inefficient. These inefficiencies are described in this section.

We measured the efficiency of our drift chambers using single muon data taken periodically throughout the run. To measure the efficiency of the drift chambers in a particular gap, we searched for tracks while ignoring the drift chamber data from that gap. If a track was found that went through the fiducial volume of the drift chamber in the gap under test, we asked if there was a hit within the resolution of the track fit. The raw efficiency was defined as the probability that there was a hit. The raw efficiency was corrected for the effect of random hits to give the "true efficiency".

We found significant drift chamber inefficiencies in the first three gaps. In the second and third gaps these inefficiencies were confined to wires that were close to the beam pipe. In the first gap, the original drift chambers (with the 1" drift cell) were found to be inefficient over their entire volume. The new chambers (with the .25" drift cell) were not found to have significant inefficiency, but they only covered gap 1 out to a distance of 12.625" from the beam axis. Figures 12-14 show the measured efficiency of the (original) chambers in gaps 1-3 respectively as a function of distance from the beam axis.

We believe that the drift chamber inefficiencies were caused by the buildup of space charge due to excessive rate. This is logical since the inefficiencies occurred in those regions of the chambers where the singles rates were high. Radiation damage may also have been a factor, as the inefficiencies seemed to get worse with each run.

We do not regard our drift chamber efficiency measurements as 100% reliable. For example, we know that there must have been short term variations in the drift chamber inefficiencies due to pion beam intensity changes. There may also have been a long term efficiency decline. We did not attempt to measure such effects, nor would it have been feasible to do so. We therefore attempted to analyze the data in such a way as to minimize the systematic error from our imperfect knowledge of the drift chamber inefficiencies. The specific steps we took to accomplish this are described later, however, I will note here that the

most important of these was a set of drift chamber fiducial cuts that removed most of the inefficient regions of the drift chambers. It was for the purpose of determining these cuts that the drift chamber efficiency measurements were most important.

The other inefficiency we found was a trigger inefficiency. Evidence for this came from the octant distribution of events. Because of the eightfold symmetry of the apparatus we expected (almost) equal numbers of muons in each of the eight octants. Instead, we found a significant departure from eightfold symmetry. Figure 15 shows our observed octant distribution of muons, together with the octant distribution predicted by our Monte Carlo program (the Monte Carlo is described in chapter 4). Known sources of asymmetry in the apparatus were unable to account for the octant asymmetry in the data.

Actually, we were never able to definitively pin down the source of this asymmetry, although we eliminated many possible sources. One of the first things we checked was the octant dependence of the drift chamber efficiencies. Although we found differences between the octants, they were not enough to explain the octant asymmetry.

During the analysis, we undertook a large program of trigger efficiency studies. During the run we had taken data with several special triggers to enable us to measure the efficiency of various pieces of the trigger. Included in the special runs were "external trigger" runs which used a trigger almost wholly independent of our normal trigger. The external trigger was based on three large scintillation counters in coincidence that were not normally part of the detector. During the trigger efficiency studies, we measured the efficiencies of the individual trigger scintillator counters and the coincidence matrices: M_{12}, M_{23} and M_4.

The result of the trigger efficiency studies was that we found that a handful of our 272 trigger counters were inefficient. The worst counter had an efficiency of about 50%. We removed this counter by a software fiducial cut. Of the remaining counters, four had efficiencies less than 90% (the worst was 80%) and most of the rest were in the high 90%'s. None of the coincidence matrices were found to have a significant inefficiency. These slight inefficiencies were insufficient to explain our octant asymmetry.

Because of these negative results, we attributed the octant asymmetry to some other inefficiency in the trigger. The most likely candidate is the octant coincidence circuit within the PML, whose efficiency we have no way of measuring. In any case we invented several ad hoc schemes to describe this inefficiency, whatever its source. Each of these schemes assigned overall efficiencies to particular octants and octant pairs.

The simplest scheme was to assign an overall efficiency to each octant. This scheme was not totally satisfactory because it did not result in a (+,–) octant correlation matrix that was azimuthally symmetric. In comparing the measured octant correlation matrix to the one predicted by the Monte Carlo, we noticed that most of the discrepancy (after putting in octant efficiencies) came from the following five octant pairs: (+,–) = (6,1), (7,2), (8,3), (1,4) and (2,5). We therefore invented two other schemes that treated these five octant pairs specially. The first of these was to remove these five octant pairs by a fiducial cut. The second scheme was to assign an additional inefficiency to these five octant pairs. This was the scheme that we used to obtain our final results. Table 5 summarizes the various octant efficiency schemes we used to describe the octant asymmetry. We used the differences between the various schemes and the absence of a correction as a measure of our systematic error.

CHAPTER III

PRIMARY ANALYSIS

The analysis of the data for this experiment divided naturally into two steps: the extraction of the dimuon signal and the interpretation of the dimuon signal. We call the former task the primary analysis. It is the subject of this chapter. The interpretation of the dimuon signal is described in the next two chapters. The dimuon signal is defined as the number of correlated, target produced, opposite sign muon pairs per unit of phase space. Measuring the dimuon signal involved three separate steps. These were event selection, event reconstruction and background subtraction.

The Reconstruction Program

The spring 1982 run, on which this thesis is based, produced approximately 400 800BPI magnetic taps of raw data containing about 4,000,000 events. Fewer than .5% of these events were good dimuons. A computer program (the reconstruction program) was written to perform the first pass analysis of these data. The purpose of this program was to find target muon tracks and perform a preliminary event selection to reduce the volume of data.

The heart of the reconstruction program was the track-finder. The purpose of the track-finder was to search drift chamber hits for muon tracks. The track-finder was capable of finding at most one muon track per octant. (The probability of a second distinct findable track was negligible.) The track-finder could be called in two modes: constrained and unconstrained. These modes differed in the mathematical model that they used to describe muon tracks. Constrained mode used a three parameter track model which required the muon to pass through the center of the experimental target. Unconstrained mode used a four parameter track model which did not require the muon to pass through the target, but

required it to be coplanar with the beam axis. The two modes gave complementary information about an event. The constrained mode gave maximum resolution for target tracks, but was insensitive to halo muons. The unconstrained mode could find both target and halo muons, but with poorer resolution. The reason for having the unconstrained mode was to help distinguish target and halo muons (which was not always easy).

The reconstruction program used constrained mode tracks to decide whether to retain each event. Any event with at least one positive and one negative constrained track was retained. Information about each retained event was written to an output file called a DST (data summary tape). Information written to the DST included all of the raw data for each event plus any constrained and unconstrained tracks which were found by the track-finder. Spill information (e.g. scalers and control system information) was also written to the DST. Of the 4,000,000 raw data events, about 22,000 made it to the DST's.

Track-Finding

Each octant contained 15 drift chambers located in seven gaps following the seven toroid magnets. Each gap had at least one X and one U drift chamber. The 15th drift chamber was a small X chamber in gap 1. The first task performed by the reconstruction program was the conversion of drift chamber raw data (i.e. the time history of hits on each sense wire) to X and U coordinates. Normally a muon passing through a drift chamber produced hits on both of that chamber's sense wire planes. The times of these hits had a characteristic sum which was independent of the track position. The reconstruction program searched the drift chamber raw data for all such sum of times pairs and calculated an X or U coordinate from each one. The reconstruction program converted any leftover hits which were not part of a sum of times pair into two X or U coordinates (because of the unresolved left-right ambiguity). To reduce the number of out of time hits, all reconstructed hits were required to be within 1.5" of a struck scintillation counter (except at the inner edge of gap 1 where a scintillation counter was not required by the trigger). Reconstructed drift chamber hits were catalogued by octant and drift chamber plane number. For the purpose of this catalogue, the two X drift chambers in gap 1 were considered to belong to a

single plane.

Catalogued X and U hits were used as input to the track-finder proper. The job of the track-finder was to decide which hits (if any) were part of a muon track and to determine its track parameters. Both jobs were performed with the help of the track-fitter.

The track-fitter fit a given set of track coordinates to a mathematical model of an ideal muon track. The track-fitter performed a χ^2 minimization using a non-diagonal definition of χ^2. The non-diagonal χ^2 took into account gap to gap correlations in deviations from the ideal track due to multiple scattering and energy loss. A more complete description of the track-fitter can be found in appendix A. The output of the track-fitter consisted of a complete set of track parameters and χ^2. The track-finder used the value of χ^2 to decide whether a given set of track coordinates was consistent with the hypothesis of a muon track.

The drift chamber data in a particular octant usually contained more hits than were caused by, or could have been caused by, a single muon track. The track-finder called the track-fitter to evaluate possible combinations of track coordinates. If several sets of coordinates were consistent with the hypothesis of a muon track, the track-finder remembered the longest track, or among tracks of equal length, the track with the smallest χ^2.

The challenge in solving the pattern recognition problem was not just to get the right answer, but to get the right answer fast enough. It would have taken far too long to call the track-fitter for every possible combination of track coordinates. We developed a number of techniques to reduce the number of fitter calls that were required.

First of all, the hit combinations were arranged in a tree structure. Each node of the tree corresponded to a single combination of hits. Different levels of the tree corresponded to hit combinations with different numbers of gaps. The root of the tree was the null combination (i.e. no hits). Successively lower levels of the tree each added a single gap until by the bottom of the tree all seven gaps had been added. The track-finder checked the nodes of the tree, starting at the root, by moving downward until it came to a bad node (or the bottom of the

tree) and then backing up until it could find a new node by moving downward again. It continued in this way until it had searched the entire tree or the number of fitter calls exceeded 200. It was frequently possible, by eliminating a node fairly high up in the tree, to eliminate whole branches of the tree, thus saving many fitter calls.

Another way we saved time was by developing a set of criteria for the acceptability of hit combinations not based on the track-fitter. These new criteria saved time because they were much faster than the track-fitter and because they needed less information and therefore could be applied higher up in the tree. (The track-fitter required at least three gaps of hits.)

The simpler of these was a drift chamber fiducial volume cut. That is, the X and U coordinates in the most recently added gap were required to correspond to a point in the fiducial volume of the drift chamber. This cut was applied at each node where the most recently added gap had both an X and a U coordinate.

The other criterion was more sophisticated. It was a smoothness criterion that was applied to nodes that had at least two gaps. The basic idea was to find linear combinations of X and U coordinates that did not depend strongly on the track parameters and place cuts on these. A more complete description of these linear precuts can be found in appendix B.

It was frequently possible by the use of these non-fitter cuts to eliminate garbage events without even a single track-fitter call.

Another problem faced by the track-finder was inefficient drift chambers. As explained in chapter 2, some regions of the first three gaps were inefficient. Obviously, one effect of these inefficient drift chambers was to cause us to lose events. An even more serious problem than loss of statistics was the systematic error caused by the uncertainty in track-finding efficiency. We attempted to measure these inefficiencies, of course, but a complete and unbiased measurement was not possible. The track-finder was designed to make optimum use of information from the efficient regions of the drift chambers to find as many tracks as possible and to limit the systematic error. In gap 1, where the inefficiency was greatest, tracks were only required to have an X or U hit alone. (In the other six gaps, both an X and a U hit were required.) Also, the track-finder specifically looked

for tracks which went through the inefficient regions of gap 1 or gap 2, but did not have hits in these gaps. The minimum length for these skipped gap tracks was increased from four to five gaps.

Event Selection

The signal to noise ratio of events on the DST was much improved over the raw data, but there was still considerable background. We estimate that about 40% of the events on the DST were background. Much, though not all, of this background was removed by a set of cuts, which are described in this section. The remaining background was removed by a statistical subtraction. The background subtraction required an accurate estimate of the background, which is described in the next section. We used the background estimate not only for performing the background subtraction, but also for optimizing the cuts. In describing the cuts, I have shown their effect on both signal and background.

The cuts were designed with specific failure modes of the track-finder in mind. It had been observed from hand scanning events that bad events on the DST were usually associated with halo muons or lots of extra drift chamber hits or both. For example, a positive halo muon close to the beam axis could look like a positive target track. A halo muon at a large radius, together with a random drift chamber hit at small radius in gap 1 could be mistaken for a negative target track. Sometimes there were so many extra drift chamber hits that some random collection of them could pass for a track.

The cuts were applied independently in each octant where there was a constrained track. The use of correlating cuts (i.e. cuts on quantities derived from both tracks) was avoided. This was reasonable, since the target was small compared to our target resolution.

The first cut on the DST tracks was a cut on the number of reconstructed drift chamber hits in the first four gaps that were associated with struck scintillation counters. Figures 16 and 17 show the distribution of the number of hits for DST events, together with the background, for positive and negative tracks respectively. For positive tracks the data and background distributions have almost the same shape and therefore a cut on this distribution would have been

ineffective. For negative tracks, on the other hand, the background saturates the data at large numbers of hits. We cut this distribution at 35 hits, as shown.

The remaining cuts made use of the information from the unconstrained track fit. The philosophy of these cuts was to use the unconstrained track fit to veto events in which a constrained track was associated with a halo muon. This was accomplished by requiring the parameters of the constrained and unconstrained track to be consistent, within resolution. Two quantities were defined which measured the difference between the constrained and unconstrained track in a given octant. These were $P_c \cdot (\theta_c - \theta_u)$ ($P \cdot \Delta\theta$ for short) and $(P_c - P_u)/P_u$ ($\Delta P/P$ for short). P refers to the momentum and θ to the polar angle of the track. The subscripts c and u refer to constrained and unconstrained. Figures 18 and 19 show the distribution of $P \cdot \Delta\theta$ for positive and negative tracks and the cuts. The cuts were -1.5 and 1.2 for positives and -1.2 and 1.5 for negatives. Figures 20 and 21 show $\Delta P/P$. The cuts were $\pm .3$ for both positive and negative. These cuts were not applied if an unconstrained track was absent or had fewer planes than the constrained track. In that case the constrained track was accepted regardless.

We did not apply a χ^2 cut over and above that applied by the track-finder. The track-finder had already applied a fairly tight χ^2 cut to make it as fast as possible. The χ^2 cut applied by the track-finder was 3/d.o.f. for four gap tracks and 3.75/d.o.f for longer tracks. Various distributions of χ^2/d.o.f. are shown in Figures 22-25. Figure 22 shows the χ^2 distribution for four gap positive tracks. Figure 23 shows the χ^2 distribution for positive tracks that were longer than four gaps. Figures 24 and 25 show the χ^2 distributions for short and long negative tracks.

We also applied a set of drift chamber fiducial volume cuts with the idea of reducing the systematic uncertainty in the track-finding efficiency due to drift chamber inefficiencies. The idea of these cuts was to eliminate tracks which went through the inefficient region of at least one gap. For the purpose of this cut, the inefficient regions of the drift chambers were defined as $12.625" < x_1 < 20"$, $x_2 < 13"$ and $x_3 < 13"$. The variable x_n refers to the octant x coordinate in gap n. In gaps 1 and 2, these cuts were applied only to four gap tracks, since tracks

with five or more gaps did not require hits in the inefficient regions of gaps 1 and 2. The gap 3 cut was applied to all tracks regardless of length. The effect of these cuts was that each accepted track was reconstructed with an efficiency that did not depend strongly on the drift chamber efficiency measurements.

Background

There were two sources of background associated with the dimuon signal from the experiment. These were dimuons produced outside the experimental target (i.e. in the collimator) and accidental coincidences of uncorrelated tracks.

The background from collimator induced dimuons was relatively unimportant. We measured the rate of collimator induced dimuons by taking data with the target removed. These target-out data runs were interspersed with our normal data runs and amounted to 6% of our total exposure. After all cuts, we were left with only 10 target out events which were themselves contaminated by an estimated accidental background of 4.5±2.0 events. This represents an event rate that is 1.2±0.8% of our target-in rate. Measurements with our split ion chamber showed that the number of pions hitting the collimator was about 10-15% of the number hitting the target. Because of differing nuclear absorption, pions hitting the steel of the collimator were only about three-quarters as effective in producing Drell-Yan pairs as pions hitting our tungsten target. Nevertheless, it is clear that collimator-induced dimuons were detected with a much lower efficiency than target-induced dimuons. Because of the limited statistics of the target-out sample, it is difficult to compare shapes of the target- and collimator-induced spectra, however there is some indication that the collimator-induced dimuons were concentrated at lower mass. Of the 10 target out dimuons, only 3 had a mass greater than 4.5 GeV/c^2 and none had a mass greater than 7 GeV/c^2. For masses greater than 4.5 GeV/c^2, the ratio of the rate of collimator to target dimuons is 0.6±0.6%. We did not make any correction for collimator- induced dimuons.

The accidental background was much more important. Understanding the accidental background was important both for tuning the event selection cuts (as in the previous section) and for statistically subtracting the background from the

final sample. We developed a method that we believe correctly measured both the shape and normalization of this background.

The starting point of the method was the observation that the production rate of accidental dimuons was basically the product of the production rates of positive and negative single muons. Some possible sources of single target muons were decays of secondary pions and kaons in the space between the target and the collimator, prompt single muon production via heavy flavor or vector meson decay, and misidentified halo. The most direct way of obtaining the accidental background would have been from the positive and negative single muon spectra. Although we took single muon data for just this purpose, we eventually settled on a less direct method that was compatible with our normal dimuon trigger. There were two advantages that came from using the same trigger to measure our data and background. The first was that our background measurement was automatically normalized. The second, less obvious, advantage was that the resulting single muon spectra were influenced by (almost) the same trigger biases as the real background.

The basic idea of the method was to derive the accidental coincidence rate of opposite sign target muons ($[T^+ \cdot T^-]$) from three accidental coincidence rates involving target and halo muons ($[T^+ \cdot H^-]$, $[H^+ \cdot T^-]$, and $[H^+ \cdot H^-]$). The basic formula is given below.

$$[T_i^+ \cdot T_j^-]\,[H_k^+ \cdot H_l^-]\,P_{ij}A_{kl}A_{il}A_{kj} = [T_i^+ \cdot H_l^-]\,[H_k^+ \cdot T_j^-]\,P_{ij}A_{kl}A_{il}A_{kj} \qquad \text{(III.1)}$$

The subscripts (i,j,k,l) refer to octant number. The factors P_{ij}, A_{kl} etc. have been inserted to insure octant compatibility. The factor P_{ij} refers to the hardware octant trigger requirement. P_{ij} is 1 if octants i and j can trigger and 0 otherwise. A_{ij} is 1 if octants i and j are non-adjacent and 0 otherwise. Theoretically, A_{ij} could be replaced by P_{ij}. The more restrictive non-adjacency requirement was used to reduce the probability of the halo coincidence rates being contaminated by correlated sources. Equation III.1 can be solved for the total number of background dimuons, B.

$$B = \sum_{ij} P_{ij}\,[T_i^+ \cdot T_j^-] = \sum_{ijkl} w_{ijkl}\,[T_i^+ \cdot H_l^-]\,[H_k^+ \cdot T_j^-] \qquad \text{(III.2)}$$

where

$$w_{ijkl} = \frac{P_{ij}A_{kl}A_{il}A_{kj}}{\sum_{mn} A_{mn}A_{in}A_{mj}\,[H_m^+ \cdot H_n^-]} \qquad \text{(III.3)}$$

This formula gave only the total number of dimuons. In practice, the background was calculated on a run by run basis by making a list of single target muons from $T{\cdot}H$ events, and then forming all possible pairs of positive and negative target muons. Each pseudo-event was given a weight w_{ijkl}. This yielded the correct total background and also permitted us to calculate background distributions. Errors were calculated by assigning a different variance weight to each pseudo-event such that the variance weights added up to the correct total variance, based on propagation of errors. This procedure for calculating the error of the background was not strictly correct, since it ignored correlations between bins of phase space, but in most bins the error of the background was small compared to the error of the signal.

We tested the validity of the background calculation method using same sign dimuon data. About one third of our data were taken with a trigger that allowed same sign dimuons. These data contained 1268 same sign positive dimuons and 3 same sign negative dimuons. We believe that the same sign dimuons were almost entirely accidental, there being no plausible physics mechanism capable of producing same sign dimuons at the observed rates. We used a slightly modified version of the background formula to calculate the same sign positive background. The result was an estimated background of 1296 ± 59.2, in agreement with the data. Figures 26-29 compare the distributions of the same sign positive data and background for five dimuon variables. The shapes of these distributions also agree.

CHAPTER IV

EXTRACTION OF CROSS SECTIONS

This chapter describes how we converted our raw counting rates into differential cross sections.

The Monte Carlo

The result of the primary analysis was the raw distribution of events accepted by the apparatus. To compare this experiment with theory or other experiments it is necessary to express the result in a form that is independent of the details of the apparatus (e.g. as a differential cross section). That is, it is necessary to correct the raw event distribution for acceptance and resolution smearing. This was accomplished with the help of a Monte Carlo program.

The Monte Carlo randomly generated events in the target using a particular differential cross section. This cross section was chosen to be self-consistent with our data. Self-consistency was achieved by iterating the analysis until the result agreed with the input to the Monte Carlo. For the pion valence structure function, we used our own result. For the pion sea structure function, we used the measurement of the NA3 collaboration.[27] For the nucleon structure function we used the M^2-dependent parameterizations of Eichten, Hinchliffe, Lane and Quigg (EHLQ).[28] The p_T spectrum was assumed to be independent of any other variable. It was set to our result in the mass range $4.5 < M < 8.5$ GeV/c^2. The angular dependence of the differential cross section was assumed to be $1+\cos^2\theta$ in the Collins-Soper frame.

The Monte Carlo also took into account the energy spread of the pion beam and its degradation by absorption and secondary production, and nuclear Fermi motion. The momentum spectrum of the pion beam was calculated by Monte Carlo simulation.[23] Nuclear absorption was based on the absorption cross section

measurements of Carroll et al.[29] From these measurements we calculated an exponential absorption length, λ_{abs}, of 11.75 cm for our composite target. This implied a luminosity per incident pion (assuming a linear A-dependence) of $L = N_0\rho\lambda_{abs}(1-e^{-l/\lambda_{abs}}) = 1.10\times10^{26}\text{cm}^{-2}$. N_0 is Avagadro's number; $\rho = 18.8\text{g/cm}^3$ is the measured density of our target; $l = 20.4$ cm is the length of our target. The absorption cross sections measured by Carroll et al. are total inelastic cross sections (i.e. they have been corrected for elastic and quasi-elastic scattering). In order to estimate the importance of pions produced in inelastic collisions, we included a model of this effect in the Monte Carlo. The details of this model are described elsewhere.[30] The model calculated the flux of inelastically produced pions as a function of pion momentum and position within the target for pions with momenta greater than 140 GeV/c. The inclusion of these secondary pions resulted in an 8% increase in the luminosity per incident pion. Of course, the number of Drell-Yan pairs induced by secondary pions was less than 8% of the total since the cross section is smaller at lower energy. According to the Monte Carlo, pions in the momentum range 140-200 GeV/c accounted for about 3% of the total dimuon production. Furthermore, this fraction was nearly flat over the acceptance of the apparatus.

Nuclear Fermi motion was assumed to be a T=0 Fermi gas with a Fermi momentum of 265 MeV/c.[31] That is, nucleon momenta were uniformly distributed in a sphere in momentum space with a radius equal to the Fermi momentum. Recent results concerned with the EMC effect have cast doubt on the idea of extracting nucleon cross sections from data taken with heavy nuclear targets.[32] We therefore decided to use the simplest model for nuclear Fermi motion to minimize the size of this correction.

The generation of a Monte Carlo event consisted of randomly choosing values for 13 variables. These were the longitudinal momentum of the interacting pion (the transverse components of the pion momentum were assumed to be zero), the vector momentum of the nucleon, the spatial coordinates of the interaction vertex, and six dimuon variables: mass, Feynman-x, the transverse momentum vector, and the decay angles.

Next, the development of the event in the apparatus was modeled. The final state muons were propagated out of the target and through the apparatus. The propagation included random multiple scattering and fluctuating energy loss[33] and took into account the detailed geometry of the apparatus. The passage of the muons through the apparatus was used to generate simulated drift chamber and counter hits, including the effects of known inefficiencies. If the muon tracks hit enough counters to satisfy the trigger requirement, then the event was analyzed as if it had been a real data event. The simulated drift chamber hits were reconstructed by the reconstruction program and the same event selection cuts as were used in the data were applied to the reconstructed Monte Carlo event. The distribution of the surviving Monte Carlo events was called the output spectrum.

In addition to the output spectrum, which represented the distribution of events after detection, we defined an input spectrum which represented the distribution of events before detection. The input spectrum was generated the same way as the output spectrum, except that the effect of the detector (except for the target) was not modeled and all of the events were accepted.

Figures 30-43 compare various distributions derived from the data and the Monte Carlo output spectrum. Figures 30-33 show the distribution octant x-coordinates for positive tracks in the first four gaps. Figures 34-37 do the same for negative tracks. Figures 38 and 39 show the constrained χ^2 distributions for positive and negative tracks respectively. Figures 40 and 41 show unconstrained χ^2 distributions for positive and negative tracks. Figures 42 and 43 show the distribution of octant x-coordinates for unconstrained tracks at z-coordinate of the target. Figures 30-37 show good agreement between the data and the Monte Carlo output spectrum. Figures 38-41 show that χ^2 distributions are slightly fatter in the data than in the Monte Carlo. Figures 42 and 43 show worse target resolution in the data than the Monte Carlo. We believe that the worse resolution in the data results from extra drift chamber hits (i.e. the track-finder chooses the wrong hit sometimes). Monte Carlo studies have confirmed this. They have also shown that constrained track-finding is less susceptible to disruption by extra hits than unconstrained track-finding.

Data Corrections

The Monte Carlo was used to correct the data for resolution smearing and acceptance. I will consider smearing first.

Our data are affected by two kinds of resolution smearing, namely the uncertainty in the momenta of the initial and final state particles. Final state smearing was caused by the error in event reconstruction, which was dominated by the multiple scattering and energy loss of muons in iron. Initial state smearing was caused by the momentum spread of the pion beam and nuclear Fermi motion. The correction factor for final state smearing was calculated by taking the ratio of the output spectra binned according to reconstructed (smeared) and true (unsmeared) variables. The correction factor for initial state smearing was calculated by taking the ratio of input spectra generated with and without Fermi motion and a pion beam momentum spread. That is, the unsmeared input spectrum was generated assuming each interacting pion had a momentum of exactly 225 GeV/c and that the interacting nucleon was at rest. The size of the unsmearing corrections for mass, p_T and x_F are shown in Figures 44-46.

Acceptance is the probability that an event generated in a given bin of phase space will be detected. It was calculated from the ratio of the (unsmeared) output spectrum to the (smeared) input spectrum. That is, both spectra contain initial state but not final state smearing. The total correction factor for both smearing and acceptance is the product:

$$\left[\begin{matrix}\text{initial state}\\ \text{unsmearing}\end{matrix}\right] \times \left[\frac{1}{\text{acceptance}}\right] \times \left[\begin{matrix}\text{final state}\\ \text{unsmearing}\end{matrix}\right]$$

$$= \left[\frac{\text{unsmeared input}}{\text{smeared input}}\right] \times \left[\frac{\text{smeared input}}{\text{unsmeared output}}\right] \times \left[\frac{\text{unsmeared output}}{\text{smeared output}}\right]$$

$$= \frac{\text{unsmeared input}}{\text{smeared output}}$$

In practice, resolution smearing and acceptance were corrected simultaneously using the last ratio. In the remainder of the thesis, unless otherwise noted, the term acceptance refers to the ratio of the smeared output spectrum to the unsmeared input spectrum.

The average differential cross section in a given phase space bin was derived by dividing the number of events by the product of the (smearing corrected) acceptance, the total luminosity and the size of the phase space bin. It is true that this involved circular reasoning, since the differential cross was required as input to the Monte Carlo. In order to have confidence in the answer, it was necessary that the calculated acceptance depend only weakly on the input model, and that the derived answer be consistent with the input model.

A final correction converted the average differential cross section to the cross section at the bin center. The bin center correction was based on a parameterization of the differential cross section. The correction factor was the ratio of the parameterization at the bin center to its average over the bin. The χ^2 function that was minimized in calculating the parameterization was defined in terms of the difference between the (uncorrected) differential cross section and the average of the parameterization for each phase space bin so that it was not necessary to iterate the fit.

Systematic Errors

There are uncertainties in the model of our apparatus which cause uncertainties in our calculated acceptance. We have estimated these by making what we estimate to be "one sigma" changes in some parameters of the apparatus model and rerunning the Monte Carlo. We took the difference in the acceptance calculated by the original and changed Monte Carlo as an estimate of the systematic error due to the uncertainty in the changed parameter. The following list summarizes the systematic errors we have studied this way.

1. Magnetic field

   We assigned a $\pm 1\%$ systematic error to the normalization of the magnetic field based on the reproducibility of total magnetic flux measurements

2. Mean energy loss

   We assigned a $\pm 5\%$ systematic error to the mean energy loss of muons in iron based on differences among various calculations of energy loss.[34]

3. Geometry

   We observed a 1.5 inch systematic shift between the average target z-position as reconstructed in the data and the Monte Carlo (see Fig. 47). Because of this we assigned a ± 1.5 inch systematic error to the target z-position. We do not actually believe that there is such a large error in the measurement of the target z-position relative to the detector. Rather, we use this shift as a metaphor for other, unknown, systematic errors connected with the geometry of the apparatus.

4. Drift chamber inefficiencies

   Our normal Monte Carlo was reconstructed using our measured drift chamber inefficiencies. We also reconstructed the Monte Carlo without any drift chamber inefficiency. The systematic error from the uncertainty in the measurement was estimated as one third of the difference between these two reconstructions. Because of the way the data was cut, this turned out to be the smallest of the systematic errors we considered.

5. Trigger inefficiency

   The systematic error from the trigger inefficiency was estimated by comparing different correction schemes with themselves and with the absence of any correction.

6. Beam energy

   The beam energy was never measured. Our only knowledge of it comes from a Monte Carlo calculation based on the geometry of the beamline elements. A different experiment in the same beamline (E-615) has estimated the beam energy by measuring the spectrum of halo muons.[35] Their result (at a slightly higher momentum setting) was that the beam energy was 7% higher than it should have been. Based on this, we have assigned a 7% systematic error to the beam energy.

Normalization

Our raw counting rate and the differential cross section are related by the following equation.

$$dN = LA d\sigma$$

where L is the integrated luminosity and A is the acceptance. Both L and A have their own normalization systematic errors. Several sources of acceptance systematic error were discussed in the previous section. In this section I am concerned with a different class of systematic errors, namely, those having to do with overall detection efficiency.

The integrated luminosity is the product of the luminosity per incident pion and the number of pions (live and on target). The devices we used to monitor the beam are described in chapter II. Chief among these was a calibrated ion chamber. The overall error in the number of incident pions is determined by the error in the scale factor of this device, which has been quoted at 10%.[22] We calculate that the total number of live pions on target was 2.05×10^{13}.

In a thick target experiment like ours, the luminosity per incident pion depends strongly on the degradation and absorption of the pion beam in the target. Experimental uncertainties in the absorption cross section for pions are in the 3-4% range.[29] These contribute directly to an uncertainty in the luminosity per pion. Also there are practical ambiguities involved in trying to separately account for the effects of elastic, quasi-elastic and inelastic pion-nucleus interactions. We have assigned a 5% systematic error to our luminosity per unit pion. We calculate a luminosity per incident pion of 1.21×10^{26} events/pion-cm^2 for an integrated luminosity of 2.47×10^{39} events/cm^2.

Besides the acceptance systematic errors that were considered previously there is a potential normalization error resulting from event reconstruction inefficiency. The event reconstruction efficiency is hard to measure. The Monte Carlo predicts a high reconstruction efficiency ($\sim$98%), however, there may be losses that were not modeled properly. One effect that we did not put in the Monte Carlo was extra hits. Small scale Monte Carlo studies suggested a 6-7% loss of events flat over phase space from this effect. Another possible source of inefficiency was the constrained χ^2 cut. Figures 38 and 39 show that the data χ^2 distributions are fatter than the Monte Carlo χ^2 distributions. The reason for this is not known, but it could be due to any of a variety of imperfections in the model of the apparatus. Because of this, we could be losing some good events in

the tails of the χ^2 distributions. On the other hand, it is not obvious that we want to retain the events in the tails of the χ^2 distributions (they could be collimator induced dimuons, for example). The best χ^2 distributions to use for judging the efficiency of the χ^2 cut are the four gap χ^2 distributions. This is because the track-finder looks for short tracks first, and then tries to extend them. If a long track fails the χ^2 cut, the track-finder still knows about any shorter version of the track it has found. Figures 22 and 24 show that the four gap χ^2 distributions substantially cut off before the cut, although there is still some tail. As far as cuts based on the unconstrained fit are concerned, Figures 16-21 show no significant loss. In cases where the unconstrained fit may have been lost altogether, the track is retained.

We have not assumed any event reconstruction inefficiency, but we have assigned a 10% one-sided systematic error to the overall normalization for reconstruction efficiency. This gives a total normalization systematic uncertainty (added in quadrature) of +15% and -11%.

CHAPTER V

RESULTS AND CONCLUSIONS

This chapter contains our results on the differential cross section for Drell-Yan production, our interpretation of these results and our conclusions.

General Features of the Data, Background and Acceptance

Figure 48 shows the raw mass spectrum and calculated background from our entire data sample, together with the acceptance. Several features of this plot are notable. The background is large at low mass, but falls much more rapidly than the data. The background falls from about 30% of the data just above the ψ to less than 1% of the data for masses greater than 7 GeV/c^2. The mass acceptance, which is very small for low masses, is first a steeply rising and then a more slowly rising function of mass with a knee around 7-8 GeV/c^2.

The capabilities and limitations of this experiment are related to the mass dependence of the background and acceptance curves. At low mass, the rapidly varying acceptance and large background make the interpretation of the data more difficult and amplify systematic errors. This thesis is concerned with the two mass continua that are accessible to the experiment. These are the ψ to Υ continuum (defined as the mass range $4.5<M<8.5$) and the high mass continuum (defined as $M>11$). Most of the ψ to Υ continuum lies below the knee of the acceptance curve and also has substantial background. the high mass continuum has a relatively flat acceptance and negligible background, but also much less data.

Figure 49 shows the raw p_T spectrum and its background in the ψ to Υ mass range. The background falls less rapidly than the data at high p_T. The background saturates the data for p_T greater than 4 GeV/c.

Figure 50 shows the raw x_F spectrum and its background in the ψ to Υ mass range. The background is greatest at low x_F and saturates the data just above the low x_F edge of the data. This plot shows that the data are confined to the range of central x_F values.

The small acceptance at low mass affects different areas of phase space unequally. Figures 51 and 52 show the p_T and x_F acceptances in several mass ranges. At low mass, the p_T acceptance is small for low p_T, but rises steeply as a function of p_T. At higher mass, the p_T acceptance becomes flatter as well as larger. The x_F acceptance also becomes flatter and covers a greater x_F range as the mass is increased. The upturn at high p_T and x_F in the highest mass bin is caused by a large unsmearing correction.

Structure Function of the Pion

The pion valence structure function was extracted by fitting the M and x_F dependence of the differential cross section in the ψ to Υ mass range to the Drell-Yan model.

Data were histogramed in a rectangular grid of M vs. x_F. The size of each bin was .5 GeV/c^2 in mass and .05 in x_F. The boundaries of the fit region at low and high mass were 4.5 and 8.5 GeV/c^2 respectively. Data with $x_F < -.2$ were cut because of large background and rapidly varying acceptance. Data with $x_1 < .25$ were cut to minimize the dependence of the fit on the pion sea structure function. To keep things simple, as the x_1 cut did not correspond to bin boundaries, this cut was applied to bins as a whole. Finally, the high x_F boundary of the fit region was determined by the acceptance edge. This cut, also applied only to whole bins, varied from x_F=.2 to x_F=.4. The resulting grid had 69 bins. The number of events contained within this grid is 3327 with an estimated background of 87$\pm$10. The grid is shown in Figure 53 superimposed over a scatter plot of the data in M and x_F.

The differential cross section in each bin, $d\sigma/dMdx_F$, was extracted by the method described in chapter IV. The results are summarized in Table 6.

The differential cross section was fit to the following form.

$$\frac{d\sigma}{dMdx_F} = K\frac{8\pi\alpha^2}{9M^3(x_1+x_2)}[\ V^\pi(x_1)\ G(x_2) + S^\pi(x_1)\ H(x_2)\ ] \qquad \text{(V.1)}$$

For the definitions of the structure functions appearing on the right side of this equation, refer to chapter I, Eqs. I.13, I.14, I.23 and I.24. We fit the data using three different nucleon structure functions. The first of these was the EHLQ parameterization.[28] It is the result from this fit that we take as our main result. (It was this fit that was used to perform the bin center correction and as input to the Monte Carlo.) We also fit the data using the two nucleon structure functions used by the NA10 experiment[36] in analyzing their dimuon data. These three structure functions are described in detail in appendix C. In addition, we introduced a free parameter into the nucleon structure function G by multiplying the EHLQ parameterization by the factor $(1-x_2)^{\beta'}$. The various nucleon structure functions were used to test the sensitivity of our result to variations in the nucleon structure functions and, in the case of the last two, to compare our result with NA10. EHLQ and the first NA10 parameterization are based on CDHS neutrino data.[37] The second NA10 parameterization is based on CCFRR neutrino data.[38]

The pion valence structure function was parameterized as follows:

$$V^\pi(x_1) = {x_1}^{\alpha^\pi}(1-x_1)^{\beta^\pi}/B(\alpha^\pi,\beta^\pi+1) \qquad \text{(V.2)}$$

where B is Euler's beta function. As our data were insufficient to determine α^π and β^π independently, we fixed the parameter α^π at a particular value (usually .5).

In QCD in the leading log approximation the pion structure function acquires a logarithmic M^2-dependence. We parameterized this M^2-dependence using the method of Buras and Gaemers.[39] That is, we allowed the exponents α^π and β^π to vary with M^2 according to the following equations:

$$\alpha^\pi = \alpha_0^\pi + \bar{s}\alpha_1^\pi$$

$$\beta^\pi = \beta_0^\pi + \bar{s}\beta_1^\pi$$

where $\bar{s} = \log[\log(M^2/\Lambda^2)/\log(M_0^2/\Lambda^2)]$. We set M_0^2 to 44 GeV/c^2 (the mean M^2

of our data in the ψ to Υ mass range). Λ is the QCD mass scale parameter. The values of the exponent slope parameters, α_1^π and β_1^π, were obtained by solving the Alterelli-Parisi equations[14] for the M^2-evolution of the pion valence (i.e. non-singlet) structure function. We have fit the pion valence structure function without and with QCD leading log M^2-evolution (using Λ=.2).

For the pion sea, we used the measurement of the NA3 experiment[27] which was parameterized as follows:

$$S^\pi(x_1) = B(1-x_1)^{\gamma^\pi} \tag{V.3}$$

The normalization constant B is set by the momentum sum rule:

$$\int_0^1 [\, 2V^\pi(x_1) + 6S^\pi(x_1) \,]\, dx_1 = 1-<g^\pi> \tag{V.4}$$

where $<g^\pi>$ is the fraction of the pion momentum carried by gluons. NA3 reported γ^π=8.4±2.5 and $<g^\pi>$=.47±.15 with error correlation coefficient ρ=-.16. We ignored the M^2-evolution of the pion sea, even when the valence was allowed to evolve (except for the M^2-dependence of the normalization constant implicit in the sum rule).

Our fit results are shown in Table 7. The results of the first fit in the table (i.e. our standard fit) are shown in Figures 54 and 55. These figures compare the data and the fit values of $d\sigma/dx_1$ and $d\sigma/dx_2$. Several conclusions can be drawn from these results. First, the presence or absence of QCD leading log scaling violations in either the pion or nucleon structure functions makes little difference in the fit results over our range of mass and x_F at our level of statistical precision. Second, the various choices of nucleon structure functions have a modest effect on K, but almost no effect on β^π. In the case where we fit for G our result is consistent with EHLQ (i.e. β^N=-.16±.19 is consistent with zero). Also, the small value of the error correlation coefficient between β^π and β^N (ρ=.065) is further evidence that the shape of the pion structure function doesn't depend strongly on the nucleon structure function. Finally, changing α^π has a strong effect on the other fit parameters. It is precisely this strong correlation between α^π and β^π, which is due to the lack of data at small x_1, that prevents us from extracting them independently with a reasonable error.

Our results are subject to various systematic errors, which can be broadly classified as apparatus (acceptance) and physics model systematic errors.

Various apparatus systematic errors that contribute to errors in the acceptance were described in chapter IV. We have calculated the effect of these systematic errors on the fit parameters K and β^{π}. The results are shown in Table 8. The total error ,obtained by adding the individual errors in quadrature, is +.46 and -.37 in K and $\pm.18$ in β^{π}.

We have also measured the sensitivity of our acceptance calculation to changes in the physics model used as input to the Monte Carlo. Our conclusion is that the acceptance is quite insensitive to the physics model. Reasonable changes in the pion and nucleon structure functions resulted in negligible changes in the final fit results. Changes in orthogonal variables also had little effect. For example, stiffening the p_T spectrum so that the mean p_T was increased by 10% resulted in a change in the fit results of ΔK=-.03 and $\Delta\beta^{\pi}$=-.03. Changing the angular distribution from $1+\cos^2\theta$ to isotropic resulted in the changes ΔK=-.38 and $\Delta\beta^{\pi}$=+.03. (i.e. the assumed angular distribution mainly affects the normalization.)

We have also estimated the systematic errors resulting from uncertainties in physics models used in the fit. One of these uncertainties is the nucleon structure functions. This systematic error is hard to quantify. We have used several nucleon structure functions in an attempt gain some insight into the sensitivity of our results to changes in the nucleon structure functions. As noted previously, the different choices of nucleon structure function affect K, but do not significantly affect β^{π}. Because of this, we are confident that the uncertainty in the nucleon structure functions do not contribute a significant systematic error to β^{π}. As for K, we take the difference between the two NA10 parameterizations,[36] namely .36, as as indication of the systematic error due to nucleon structure functions.

The systematic error from the pion sea structure function is easier to quantify. We have calculated the systematic error in K and β^{π} by simply propagating the error matrix reported by NA3[27] for the parameters γ^{π} and $<g^{\pi}>$. A one sigma change in the parameter γ^{π} changed K and β^{π} by .104 and .068

respectively. A one sigma change in the parameter $<g^\pi>$ changed K and β^π by .160 and .135 respectively. When these errors are combined, including the correlation between them, the systematic errors for K and β^π are .177 and .142.

Finally, there is a systematic error that comes from the uncertainty in the parameter α^π. Our choice of α^π=.5 is based on historical and theoretical prejudice.[40] NA3 and NA10 both measure values of α^π closer to .4. To test the sensitivity of our results to the assumed value of α^π we have fit our data with the assumption α^π=.4, which is close to the values obtained by NA3 and NA10. As noted previously, this strongly affected the fitted values of K and β^π. When α^π and β^π are changed together as required by the fit, the shape of the structure function does not change significantly in the region of phase space covered by this experiment. It is in the extrapolation of the valence structure function outside the range of x_1 covered by the experiment that differences appear. Even NA3 and NA10, who quote measured values of α^π with quite small errors have a systematic error from extrapolating the pion valence structure function to low x_1 because the pion sea is poorly measured and their data (like ours) does not extend to low x_1. This is important for the measurement of the K-factor because the pion valence structure function can only be normalized with knowledge of the structure function over the whole range of x_1. We have assigned a systematic error of 20% to the K-factor from the normalization of the pion valence structure function. We have not assigned a systematic error per se to β^π from the uncertainty in α^π, but it must be kept in mind that the value of β^π that we measure corresponds to a specific value of α^π.

In conclusion, we measure the following values for K and β^π.

$$K = 2.70\ ^{+.82}_{-.77}$$

$$\beta^\pi = 1.21 \pm .26$$

The error for the K-factor includes statistical error (negligible), an apparatus systematic error of +.46 and -.37 an error of .18 from the pion sea, an error of .54 from the extrapolation over the full range of x_1 and an error of .36 from the nucleon structure functions. The error on β^π includes a statistical error of .13, an acceptance systematic error of .18 and a pion sea systematic error of .14. Both

errors are systematic dominated.

Many experiments have measured the pion structure function.[41] Table 9 contains a summary of their results for the shape of the pion structure function. Our results are consistent with these existing measurements. The experiments listed in Ref. 41 (except for the CIP experiment) have reported K-factors in the range 2.2-2.8 with typical systematic errors of 20% or larger, which is also consistent with our result.

High Mass Differential Cross Section

In the previous section, it was shown that this experiment is consistent with existing data in the mass continuum between the ψ and the Υ. The purpose of this section is to present our results for the mass continuum above the Υ and to compare them with the Drell-Yan model.

We have extracted the differential cross section $d\sigma/dM$ for masses greater than 4.5 GeV/c^2. The results are shown in Table 10. We parameterized the continuum as follows using data in the ranges 4.5 GeV/c^2 $< M <$ 8.5 GeV/c^2 and 11.5 GeV/c^2 $< M <$ 15.5 GeV/c^2.

$$\frac{d\sigma}{dM} = A\tau^{\gamma}(1-\sqrt{\tau})^{\delta} \qquad \text{(V.5)}$$

The results were A=.0441 $\pm$ .0282 nb/(GeV/c^2), γ=-0.96 $\pm$ .18 and δ=7.07 $\pm$ .59 with χ^2/d.o.f. = 12.6/13. This parameterization represents the data well both above and below the Υ (see Fig. 56).

We have also compared our high mass data with the predictions of the Drell-Yan model extrapolated to high mass. For the nucleon structure functions we have used the EHLQ parameterizations. For the pion structure function we have used our own result and a "world average" based on NA3 and NA10 results. The latter pion structure function is characterized by the parameters α^{π}=.41$\pm$.02 and β^{π}=.99$\pm$.03 at M^2=25GeV/c^2. In each case the K-factor has been allowed to float to reproduce the overall normalization of our data in the ψ to Υ mass range.

Figures 57-59 compare our data for $d\sigma/dM$ with the Drell-Yan model. Figure 57 used our pion structure function without QCD M^2-evolution in either the

pion or nucleon structure functions. Figure 58 used our result with QCD leading log M^2-evolution (using Λ=.2). Figure 59 used the world average pion structure function with M^2-evolution. In each case there is good agreement between the Drell-Yan model and our data in the ψ to Υ mass range, as expected. Figure 57 shows that the naive Drell-Yan model overestimates the data above the Υ. On the other hand, in Figures 58 and 59 the presence of QCD M^2-evolution in the structure functions reduces the prediction of the Drell-Yan model to the extent that there is reasonable agreement between the Drell-Yan model and our data even at high mass.

The above observations can be made more quantitative. In our data we have 83 events with masses greater that 11.5 GeV/c^2. The predictions of the Drell-Yan model with the assumptions of Figures 57-59 are 136, 101 and 106 events respectively. The statistical error associated with our number is 11%. Our detector systematic errors (beam energy and target position in particular) contribute about a 20% systematic uncertainty to the relative normalization between the high mass and ψ to Υ data. There is also a 5-10% error in the prediction of the Drell-Yan model due to uncertainties in the input structure functions and the value of Λ.

With these uncertainties, the number of observed high mass events is consistent with the prediction of the Drell-Yan model with M^2-evolution. We have also examined the x_F dependence of the high mass data. Table 11 contains our measurement of the cross section $d\sigma/dx_F$ for $M>11$ GeV/c^2. Figure 60 compares our data for $d\sigma/dx_F$ with the prediction of the Drell-Yan model (using the world average structure function with M^2-evolution) for $M>11$ GeV/c^2. For comparison Figure 61 shows the data of the NA10 experiment for $\sqrt{\tau}>.54$.[36] (The value $\sqrt{\tau}=.54$ corresponds to $M=11.1$ GeV/c^2 at our beam energy of 225 GeV and $M=10.3$ GeV/c^2 at NA10's beam energy of 194 GeV.) The NA10 data are in clear disagreement with the prediction of the Drell-Yan model. NA10 has called this disagreement an "anomalous scaling violation". Our data do not show an anomalous scaling violation.

Transverse Momentum Differential Cross Section

The purpose of this section is to present the transverse momentum dependence of the differential cross section. Table 12 summarizes our results for the differential cross section, $(1/p_T)(d\sigma/dp_T)$, in several mass ranges. These are the ψ to Υ continuum, four subranges within the ψ to Υ continuum and the continuum above the Υ.

We have parameterized the cross section in the ψ to Υ mass continuum as follows:

$$\frac{d\sigma}{p_T dp_T} = A \, \mathrm{sech}^n(\alpha p_T) \tag{V.6}$$

We chose to parameterize the p_T spectrum using a hyperbolic secant because that function behaves like a Gaussian for values of its argument near 0 and falls off exponentially for large values of its argument. The two shape parameters, α and n, allow you to independently tune the Gaussian width ($\sigma = 1/\alpha\sqrt{n}$) and the exponential fall-off length ($\lambda = 1/\alpha n$). The results of the fit were A=.226±.007 nb/(GeV/c)^2, α=.491±.036 (GeV/c)$^{-1}$ and n=6.04±.73, with χ^2/d.o.f. = 6.07/5. The results of the fit are shown in Figure 62. Figure 63 shows the differential cross sections in several mass ranges.

We have also calculated the mean values of p_T and p_T^2 in each of the above mentioned mass ranges. The results are shown in Table 13 and plotted in Figure 64. The statistical and systematic errors are shown separately in Table 13 and are combined in Figure 64. Our results in the ψ to Υ mass range are $<p_T> = 1.147\pm.023$ and $<p_T^2> = 1.712\pm.069$. For the purpose of this calculation, the transverse momentum spectra were cut off above 4 GeV/c.

Figures 63 and 64 show that the p_T spectrum is almost independent of mass at fixed beam energy. There is perhaps a slight stiffening of the p_T spectrum at higher mass.

Several other experiments have reported measurements of the mean transverse momenta of pion induced Drell-Yan pairs with pion energies close to our energy of 225 GeV. The CIP experiment[42] has reported $<p_T> = 1.21\pm.073$ and $<p_T^2> = 1.938\pm.085$ for pion induced muon pairs in the mass range 4.5 GeV/c^2<M<8.5 GeV/c^2 with a pion energy of 225 GeV. The NA3

experiment has measured $<p_T> = 1.123 \pm .013$[43] and $<p_T^2> = 1.74 \pm .04$[44] for muon pairs in the mass range 4.1 GeV/c^2<M<8.5 GeV/c^2 with a pion energy of 200 GeV. These results are generally consistent. The CIP result for $<p_T^2>$ disagrees with both our result and NA3's result by about 2σ.

Conclusions

This experiment has measured the differential cross section for the production of high mass muon pairs by 225 GeV/c negative pions in a heavy nuclear target. The cross section has been interpreted in terms of the the Drell-Yan quark-antiquark annihilation model. We have measured the pion structure function using muon pairs with invariant masses between the ψ and Υ masses. The results are consistent with the Drell-Yan model and with other experiments. We have used the Drell-Yan model to predict the differential cross section for muon pairs with masses greater than the Υ mass. Here too, the results are consistent with the Drell-Yan model when QCD leading log scaling violations are included in the structure functions. Finally, we have measured the p_T-dependence of the differential cross section as a function of mass. Our results for the mean values of p_T and p_T^2 are consistent with previous experiments.

APPENDIX A

TRACK-FITTING

The track-fitting problem can be stated as follows: given a set of track measurements, what set of track parameters best reproduces these measurements, and how well are the measurements reproduced? The first part of this appendix deals with the mathematical formulation of the track-fitting problem. The second part deals with the solution of the problem.

Coordinate Systems

A global Cartesian coordinate system was defined for the laboratory. The origin of coordinates was located in the vicinity of the experimental target (actually the origin was seven inches downstream of the target). The z-axis coincided with the beamline with positive z defined as downstream. The y-axis was defined as vertical with positive y being up. The x-axis was defined to complete a right-handed coordinate system.

The detector was divided azimuthally into eight identical octants. In addition to the laboratory coordinate system, a local coordinate system was defined for each octant. The origin and z-axis were the same as for the laboratory system. The local x-axis was defined as the centerline of the octant. The local y-axis was chosen to complete a right-handed coordinate system. Thus, the octant coordinate systems were related to the laboratory coordinate system by a rotation about the z-axis. An octant u-axis was defined 5.7° counter-clockwise (looking downstream) from the octant x-axis. Octant u coordinates are related to x and y coordinates by the equation $u = .995x - .0995y$.

One track measurement (as supplied by one plane of our drift chamber system) consisted of either an x or u coordinate at a specific z. One track could contain up to 14 such measurements.

Chisquare Definition

We make the following definitions:

$$a_i = \text{track parameter } i \tag{A.1}$$

$$\xi_r = \text{Measured track coordinate } (x \text{ or } u) \text{ at plane } r \tag{A.2}$$

$$\hat{\xi}_r(\mathbf{a}) = \text{Idealized track coordinate at plane } r \tag{A.3}$$

Lower case bold letters refer to vectors in parameter space. Upper case bold letters refer to matrices in parameter space. The subscripts i and j refer to parameter numbers. The subscripts r and s refer to drift chamber plane numbers.

We use the following definition of χ^2 as our goodness of fit criterion.

$$\chi^2 = \sum_{rs} w_{rs}(\hat{\xi}_r - \xi_r)(\hat{\xi}_s - \xi_s) \tag{A.4}$$

The weight matrix w_{rs} is the matrix inverse of the covariance matrix defined as follows.

$$w_{rs} = (\sigma^2)^{-1}_{rs} \tag{A.5}$$

where

$$\sigma^2_{rs} = <(\hat{\xi}_r - \xi_r)(\hat{\xi}_s - \xi_s)> \tag{A.6}$$

Mathematically, the track-fitting problem consisted of finding the values of the track parameters, $\mathbf{a}$, that minimize χ^2. Before tackling this problem, it was first necessary to determine how the $\hat{\xi}_r$ and σ^2_{rs} depended on $\mathbf{a}$.

Track Model

This section describes how we determined the idealized motion of muons through our apparatus. The differential equations (in Cartesian coordinates) for the motion of an ultra-relativistic charged particle subject to uniform (but not necessarily constant) energy loss are:

$$x'' = \frac{q}{E}\sqrt{1+x'^2+y'^2}[x'\,y'\,B_x - (1+x'^2)B_y] \tag{A.7}$$

$$y'' = \frac{q}{E}\sqrt{1+x'^2+y'^2}[(1+y'^2)B_x - x'\,y'\,B_y] \tag{A.8}$$

$$E' = -\sqrt{1+x'^2+y'^2}\,f(E) \tag{A.9}$$

The variables in these equations are as follows: $x=x(z)$ and $y=y(z)$ define the trajectory of the muon; E is the energy of the muon; q is the charge of the muon; B_x and B_y are components of the magnetic field ($B_z=0$ is assumed); $f(E)$ is the mean energy loss for a muon of energy E. Primes denote differentiation with respect to z.

The solution of these equations is straightforward. An exact analytic solution is impossible because B_x and B_y have a complicated dependence on x and y. We therefore solved the equations numerically using the fourth-order Runge-Kutta method with a step size equal to the length of one toroid. We checked the accuracy of the solution by reducing the step size. The error was quite negligible (typically less than .01" after seven toroids).

The five integration constants are the five track parameters. For the purpose of track-fitting, we chose the track parameters to be the initial value data at the z of the target (i.e. x_0, x_0', y_0, y_0' and E_0). During minimization the five track parameters were not allowed to vary independently. In constrained fitting mode the track was required to pass through the center of the target (i.e. $x_0=y_0=0$). In unconstrained mode, the track did not have to pass through the target, but was required to be coplanar with the beamline (i.e. $x_0y_0' = y_0x_0'$).

Covariance matrix

The covariance matrix was calculated by Monte Carlo simulation directly from the definition (Eq. A.6). The dependence of the covariance matrix on the track parameters was parameterized as follows.

$$\sigma_{rs}^2 = \frac{M_{rs}}{(E-\Delta E)^2} + T_{rs} + \lambda^2\delta_{rs} \tag{A.10}$$

That is, σ_{rs}^2 was assumed to depend only on the energy of the muon. The M_{rs} term is the contribution to the covariance matrix from the multiple scattering

and energy loss fluctuations of muons in iron. The T_{rs} term is the contribution from the finite size of the target. The diagonal term represents an intrinsic drift chamber resolution. ΔE and λ were empirically determined constants.

M_{rs} was calculated from the Monte Carlo by comparing tracks propagated with and without multiple scattering and energy loss fluctuations. Finite target size and intrinsic resolution effects were ignored in this calculation.

T_{rs} was calculated from first principles, making use of the Monte Carlo only to estimate the distribution of events in the target volume. This term was different in constrained and unconstrained mode, being much smaller in the latter case. This term would be zero in a totally unconstrained five parameter fit.

The diagonal term was included not only to take account of intrinsic drift chamber resolution but also to provide the χ^2 with a certain amount of leeway, so that small systematic errors in the drift chamber survey (say) would not cause uncontrollably large perturbations in the value of χ^2 determined for real tracks. The parameter λ was set at .07 inches. This value of λ was conservative in the sense that it was much larger than the intrinsic drift chamber resolution and somewhat larger than the expected survey errors.

The parameter ΔE was adjusted so that the mean value of the χ^2 was nearly independent of muon energy for Monte Carlo tracks. The value of ΔE was allowed to depend on the length of the track. The optimum value was 1.1 GeV/c^2 per toroid, or about half of the total energy loss over the length of the track. That is, E–ΔE was the average energy of the muon while it was in the spectrometer.

Minimization algorithm

The track-fitter used a hybrid of several gradient minimization methods. The prototype of such methods is Newton's method. Newton's method (and other gradient methods) start by assuming the validity of a second-order Taylor expansion of the χ^2 about some point $\mathbf{a}=\mathbf{a}_0$ in the neighborhood of a local minimum.

$$\chi^2(\mathbf{a}) = \chi^2(\mathbf{a}_0) + \mathbf{g}(\mathbf{a}_0)\cdot\Delta\mathbf{a} + \frac{1}{2}\Delta\mathbf{a}^{\dagger}\mathbf{H}(\mathbf{a}_0)\Delta\mathbf{a} \qquad \text{(A.11)}$$

where $\Delta\mathbf{a}=\mathbf{a}-\mathbf{a}_0$. In the above equation $\mathbf{g}$ is the gradient vector and $\mathbf{H}$ is the Hessian matrix calculated from χ^2.

$$g_i = \frac{\partial \chi^2}{\partial a_i} \tag{A.12}$$

$$H_{ij} = \frac{\partial^2 \chi^2}{\partial a_i \partial a_j} \tag{A.13}$$

Differentiating Eq. A.11 gives

$$\mathbf{g}(\mathbf{a}) = \mathbf{g}(\mathbf{a}_0) + \mathbf{H}(\mathbf{a}_0)\Delta\mathbf{a} \tag{A.14}$$

The condition that χ^2 be a minimum is that $\mathbf{g}=0$. This leads to a simultaneous system of linear equations that can be solved formally as follows.

$$\Delta\mathbf{a} = -\mathbf{H}(\mathbf{a}_0)^{-1}\mathbf{g}(\mathbf{a}_0) \tag{A.15}$$

Newton's method finds the minimum of a quadratic function in one step. In the case of a general function it is necessary to iterate Eq. A.15. Under favorable conditions, Newton's method converges quadratically. This high rate of convergence is hard to beat and it is a very desirable property for any minimization method to have.

Newton's method has two main drawbacks. The first drawback is that it is fairly costly in terms of function evaluations and computer time to evaluate the full Hessian matrix (assuming that analytic derivatives are not available, which is the case here). The second drawback is that the first guess used for $\mathbf{a}$ must be fairly close to the local minimum you are searching for. Newton's method method can converge slowly or even diverge if $\mathbf{a}$ is too far from the minimum.

With regard to the second objection, a technique that can be used to stabilize Newton's method and related methods is to perform a one-dimensional minimization in the direction of the step calculated by Eq. A.15. The advantage of this technique is that one is guaranteed to find a new minimum at each iteration (until a local minimum is reached) so that divergence is impossible. Because of this the requirement on the quality of the first guess is much reduced. The disadvantage of this technique is that it makes more function evaluations than necessary in the neighborhood of the minimum.

Various alternatives to Newton's method are based on ways of avoiding the use of second derivatives. The crudest of these are steepest descent methods. Here you simply replace $\mathbf{H}^{-1}$ in Eq. A.15 by some arbitrary positive-definite matrix (often the unit matrix). One-dimensional minimization of the step is required since the length of the step is not otherwise controlled. The speed of convergence depends on how fortuitous your choice of the matrix is, but in general the convergence is only linear.

There is an approximation that is often used when you are minimizing a χ^2 function. Differentiating the definition of χ^2 twice gives the following exact formula for the Hessian matrix

$$H_{ij} = 2\sum_{rs} w_{rs}\left[\frac{\partial\hat{\xi}_r}{\partial a_i}\frac{\partial\hat{\xi}_s}{\partial a_j} + \frac{\partial^2\hat{\xi}_r}{\partial a_i \partial a_j}(\hat{\xi}_s - \xi_s)\right] \tag{A.16}$$

The approximation consists of neglecting the second term in the sum. That is:

$$H_{ij} \simeq 2\sum_{rs} w_{rs}\frac{\partial\hat{\xi}_r}{\partial a_i}\frac{\partial\hat{\xi}_s}{\partial a_j} \tag{A.17}$$

This is a good approximation when the data are well represented by the model (i.e. when the $(\hat{\xi}_s - \xi_s)$ are small). This approximation allows you to calculate the Hessian matrix using only first derivatives. The approximation can break down when the data are not well represented by the model.

A more sophisticated approach is used in the Davidon-Fletcher-Powell method.[45] This method combines many of the advantages of the methods described so far. Specifically, it requires only first derivatives and it converges quadratically. The basic idea is to iteratively refine both an estimate of the minimum and the inverse of the Hessian matrix.

Suppose that you have an estimate of the minimum of the χ^2, $\mathbf{a}$, and that you know the gradient, $\mathbf{g}$, at $\mathbf{a}$. Instead of Newton's step (Eq. A.15) the DFP method calculates the step

$$\Delta\mathbf{a} = -\mathbf{V}\mathbf{g} \tag{A.18}$$

where $\mathbf{V}$ is an estimate of the inverse of the Hessian matrix. This step can be used directly, if $\mathbf{V}$ is a good enough estimate of $\mathbf{H}^{-1}$, or you can do a one-dimensional minimization along the direction of $\Delta\mathbf{a}$. In any case you obtain an

improved estimate of the minimum, $\mathbf{a}' = \mathbf{a} + \Delta\mathbf{a}$ and you calculate the gradient, $\mathbf{g}'$, at $\mathbf{a}'$. If you are in a quadratic region of parameter space, it is easy to show that $\Delta\mathbf{a}$ and $\Delta\mathbf{g} = \mathbf{g}' - \mathbf{g}$ are related by the equation.

$$\Delta\mathbf{a} = \mathbf{H}^{-1}\Delta\mathbf{g} \tag{A.19}$$

Thus $\Delta\mathbf{a}$ and $\Delta\mathbf{g}$ contain information about the Hessian matrix. This information can be used to improve your estimate of $\mathbf{H}^{-1}$. The DFP method updates $\mathbf{V}$ as follows.

$$\mathbf{V}' = \mathbf{V} + \frac{\Delta\mathbf{a}\Delta\mathbf{a}^{\dagger}}{\Delta\mathbf{a}\cdot\Delta\mathbf{g}} - \frac{\mathbf{V}\Delta\mathbf{g}\Delta\mathbf{g}^{\dagger}\mathbf{V}}{\Delta\mathbf{g}^{\dagger}\mathbf{V}\Delta\mathbf{g}} \tag{A.20}$$

The improved estimate $\mathbf{V}'$ is closer to $\mathbf{H}^{-1}$ than $\mathbf{V}$ in the sense that it satisfies the equation $\Delta\mathbf{a} = \mathbf{V}'\,\Delta\mathbf{g}$. In general, it takes n iterations (where n is the dimensionality of the parameter space) to zero out (to first order) the difference between $\mathbf{H}^{-1}$ and $\mathbf{V}$ in all directions.

The minimization used by the track-fitter used ideas from each of the methods described above. The basic algorithm was that of the DFP method. The first guess for the track parameters was supplied by a simple fit based on a quadratic polynomial, with empirically determined relations between the track parameters and the coefficients of the polynomial. The first guess for the Hessian matrix was calculated using Eq. A.17. One-dimensional minimization along the calculated step was used to enforce convergence only when the new estimate for the minimum resulted in a χ^2 that was larger than the previous best minimum. If the one-dimensional minimization failed to improve the χ^2 significantly, a second one-dimensional minimization was performed in a steepest descent direction (in case $\mathbf{V}$ was not positive definite). The track-fitter included code to force the propagation of the initial and subsequent estimates for the minimum. Basically, the first priority of the minimization algorithm was efficiency. We believe that the track-fitter was able to find the minimum value of χ^2 essentially 100% of the time.

APPENDIX B

LINEAR PRECUTS

The large number of possible hit combinations and the relative slowness of the track-fitter made it necessary to develop a fast method of identifying plausible tracks. The linear precuts described in this appendix met this need. The precuts were an adaptation of the method of H. Wind[46] for removing the redundant information contained in a set of track measurements.

Consider a sample of real or realistically simulated tracks where each track has been measured at n points on its trajectory. The set of all possible measurements makes up an n-dimensional hyperspace. Each point in the space is a possible track. All points do not correspond to plausible tracks, however. In fact, a sample of plausible tracks will be approximately confined to an m-dimensional hypersurface within this space, where m is the number of parameters needed to characterize a track (it is assumed that $n>m$). The basic idea of the precuts is to find linear combinations of the track coordinates that depend only weakly on the track parameters but depend strongly on the distance of the point from the m-dimensional hypersurface. This is accomplished by means of a rotation of the axes of the n-dimensional track space such that m of the axes are approximately parallel to and $n-m$ axes are approximately perpendicular to the m-dimensional surface populated by real tracks (assuming the hypersurface can be approximated by a hyperplane). The latter $n-m$ coordinates are only weakly correlated to the track parameters and can be used to make cuts. The rotated coordinates are called generalized coordinates.

Let ξ_r represent a measured track coordinate at drift chamber plane r and let η_r represent the rth generalized coordinate. The linear transformation from $\boldsymbol{\xi}$ to $\boldsymbol{\eta}$ is

$$\boldsymbol{\eta} = \mathbf{O}(\boldsymbol{\xi} - \langle \boldsymbol{\xi} \rangle) \tag{B.1}$$

where **O** is an $n \times n$ orthogonal matrix. The sample means of the track coordinates have been subtracted off so that the sample means of the generalized coordinates will be zero. The appropriate orthogonal matrix is determined by diagonalizing the sample covariance matrix:

$$C_{rs} = <\xi_r - <\xi_r>><\xi_s - <\xi_s>> = <\xi_r\xi_s> - <\xi_r><\xi_s> \tag{B.2}$$

Diagonalizing the covariance matrix extremizes the dispersion of the new coordinates. We diagonalize **C** by the equation

$$\mathbf{\Lambda} = \mathbf{OCO}^{\dagger} \tag{B.3}$$

where **Λ** is a diagonal matrix. The dispersion of the generalize coordinate η_r is

$$<\eta_r^2> = \Lambda_r \tag{B.4}$$

where Λ_r is an eigenvalue of **C**. The m largest eigenvalues correspond to eigenvectors (i.e. generalized coordinates axes) that are approximately parallel to the m-dimensional hypersurface populated by plausible tracks. the rest of the eigenvalues are typically quite small. These correspond to eigenvectors that are approximately orthogonal to the m-dimensional hypersurface. We placed cuts on the latter generalized coordinates.

In practice, the precuts were calculated from a sample of Monte Carlo tracks. Covariance matrices (Eq. B.2) were calculated for various possible track topologies (i.e. combinations of drift chamber planes) with values of n ranging from 4 to 14. Positive and negative tracks were handled separately. In the case of the constrained fit, tracks were characterized by three parameters, so that n–3 precuts were possible. In the track-finding process, precuts were applied to all hit combinations having at least 4 drift chamber planes. The actual form of the cut was

$$\eta_r^2 < a\,(\Lambda_r + \lambda^2) \tag{B.5}$$

For the constrained fit, a=25 and λ=.07. The λ^2 term corresponded nominally to an intrinsic drift chamber resolution. The motivation for this term was the same as for a similar term in the χ^2 definition used in the track fit and is described in appendix A. In the case of the unconstrained fit, the value of a was increased from 25 to 100 and precuts were only applied to the subset of

generalized coordinates that were almost invariant under translation toward or away from the beam axis so that they would not bias unconstrained track-finding against halo muons.

Since drift chamber planes were added to tracks one or (usually) two at a time in the process of track-finding, many precuts were applied to each track. Figures 65 and 66 are intended to show the efficiency of the precuts for positive and negative tracks respectively. These figures are histograms of the *largest* cut generalized coordinate encountered during track-finding for a sample of good tracks using only hits from the final track. The entries to these histograms were scaled so that the cut was applied at 1.0 (i.e. at the right edge of the histogram). They are based on our entire sample of good tracks from our data.

APPENDIX C

NUCLEON STRUCTURE FUNCTIONS

This appendix describes nucleon structure function parameterizations used in our analysis. We used three different nucleon structure functions. We used the EHLQ parameterizations[28] for our primary nucleon structure functions. For comparison we used the two parameterizations used by the NA10 dimuon experiment.[36] The EHLQ parameterizations and the first NA10 parameterizations were based on CDHS neutrino deep inelastic scattering data.[37] The second NA10 parameterizations used CCFRR neutrino data[38] for the valence structure functions only.

EHLQ expand structure functions as sums of Chebyshev polynomials.

$$f(x,Q^2) = \begin{cases} (1-x)^a \sum_{i,j=0}^{5} c_{ij} T_i(x') T_j(t') & x > .1 \\ (1-x)^a \sum_{i,j=0}^{5} d_{ij} T_i(y) T_j(t') & 10^{-4} < x < .1 \end{cases} \tag{C.1}$$

where

$$x' = \frac{2x-1.1}{.9} \tag{C.2}$$

$$y = \frac{2\ln x + 5\ln 10}{3\ln 10} \tag{C.3}$$

$$t' = \frac{2t - t_{max} - t_{min}}{t_{max} - t_{min}} \tag{C.4}$$

The variable t is given by

$$t = \ln(Q^2/\Lambda^2) \tag{C.5}$$

$$t_{max} = \ln(Q^2_{max}/\Lambda^2) \tag{C.6}$$

$$t_{\min} = \ln(Q^2_{\min}/\Lambda^2) \tag{C.7}$$

where $Q^2_{\max} = 10^8$ (GeV/c)^2, $Q^2_{\min} = 5$ (GeV/c)^2 and $\Lambda = .2$ GeV/c.

The values of the parameters a, c_{ij} and d_{ij} for various flavors of quarks are given in Tables 14-16 respectively.

NA10 used the following general forms for their parameterizations.

Up valence:

$$u_V(x) = A_u x^{\alpha_1}(1-x)^{\beta_V}(1+\gamma x^{\alpha_2}) \tag{C.8}$$

Down valence:

$$d_V(x) = A_d x^{\alpha_1}(1-x)^{\beta_V+1}(1+\gamma x^{\alpha_2}) \tag{C.9}$$

Up, down and strange sea:

$$\bar{u}(x) = \bar{d}(x) = 2\bar{s}(x) = C(1-x)^{\beta_s} \tag{C.10}$$

The normalization constants A_u and A_d are determined by quark counting.

$$\int_0^1 \frac{u_V(x)}{x}\,dx = 2 \tag{C.11}$$

$$\int_0^1 \frac{d_V(x)}{x}\,dx = 1 \tag{C.12}$$

Specifically,

$$A_u = \frac{2}{B(\alpha_1,\beta_V+1) + \gamma B(\alpha_1+\alpha_2,\beta_V+1)} \tag{C.13}$$

$$A_d = \frac{1}{B(\alpha_1,\beta_V+2) + \gamma B(\alpha_1+\alpha_2,\beta_V+2)} \tag{C.14}$$

B is Euler's beta function. The Q^2-dependence of the structure functions was parameterized by expanding the parameters in a power series in $\bar{s} = \ln[\ln(Q^2/\Lambda^2)/\ln(Q_0^2/\Lambda^2)]$ with $Q_0^2 = 5$ (GeV/c)^2 and $\Lambda = .3$ GeV/c. Table 17 gives the power series expansions of the parameters α_1, α_2, β_V, γ, C and β_s extracted from CDHS data. Table 18 gives the values of α_1, α_2, β_V and γ extracted from CCFRR data. Figures 67 and 68 show the three parameterizations for the composite structure functions $G(x)$ and $H(x)$ (see Eq. I.15) respectively at Q^2=44(GeV/c)^2.

REFERENCES

1. M. Gell-Mann, Phys. Lett. 8, 214 (1964);
   G. Zweig, CERN report 8419/TH 412.
2. J. D. Bjorken and E. A. Paschos, Phys. Rev. 185, 1975 (1969);
   R. P. Feynman, Phys. Rev. Lett. 23, 1415 (1969);
   R. P. Feynman, Photon-Hadron Interactions, Benjamin, Reading Mass., 1972.
3. For a review of SLAC deep inelastic scettering results, see J. I. Friedman and H. W. Kendall, Ann. Rev. Nucl. Science 22, 203 (1972).
4. J. D. Bjorken, Phys. Rev. 179, 1547 (1969).
5. C. G. Callan and D. J. Gross, Phys. Rev. Lett. 22, 156 (1969).
6. M. D. Mestayer et al., Phys. Rev. D27, 285 (1983).
7. For a general treatment of quark/parton phenomenology see F. E. Close, An Introduction to Quarks and Partons, Academic Press, New York, 1979.
8. S. D. Drell and T. M. Yan, Phys. Rev. Lett. 25, 316 (1970).
9. J. C. Collins and D. E. Soper, Phys. Rev. D16, 2219 (1977);
   C. S. Lam and W. K. Tung, Phys. Rev. D18, 2447 (1978).
10. For a recent review of the Drell-Yan process see I. R. Kenyon, Rept. Math. Phys. 45, 1261, (1982).
11. G. T. Bodwin, S. J. Brodsky and G. P. Lepage, Phys. Rev. Lett. 47, 1799 (1981).
12. J. C. Collins, D. E. Soper and G. Sterman, Phys. Lett. 134B, 263 (1984).

13. H. D. Politzer, Nucl. Phys. B129, 301 (1977);
C. T. Sachrajda, Phys. Lett. 73B, 185 (1978);
D. Amati, R. Petronzio and G. Veneziano, Nucl. Phys. B140, 54 (1978);
R. K. Ellis, H. Georgi, M. Machacek, H. D. Politzer and G. G. Ross, Nucl. Phys. B152, 285 (1979).
14. G Altarelli and G. Parisi, Nucl. Phys. B126, 298 (1977).
15. G. Altarelli, R. K. Ellis and G. Martinelli, Nucl. Phys. B157, 461 (1979);
J. Kubar, M. Le Bellac, J. L. Meunier and G. Plaut, Nucl. Phys. B175, 251 (1980).
16. G. Curci and M. Greco, Phys. Lett. 92B, 175 (1980).
17. G. Altarelli, G. Parisi and R. Petronzio, Phys. Lett. 76B, 351 and 356 (1978);
K. Kajantie and R. Raitio, Nucl. Phys. B139, 72 (1978).
18. F. Halzen and D. M. Scott, Phys. Rev. D24, 2433 (1981).
19. R. K. Ellis, G. Martinelli and R. Petronzio, Phys. Lett. 104B, 45 (1981).
20. Yu. L. Dokshitzer, D. I. Dyakonov and S. I. Troyan, Phys. Rep. 58, 271 (1980);
G. Parisi and R. Petronzio, Nucl. Phys. B154, 427 (1979);
F. Halzen and D. M. Scott, Phys. Rev. D21, 131 (1980);
G. Curci, M. Greco and Y. Srivastava, Phys. Rev. Lett. 43, 834 (1979);
J. C. Collins, D. E. Soper and G. Sterman, CERN TH.3923 (1984).
21. P. Chiapetta and M. Greco, Nucl. Phys. B221, 269 (1983).
22. N. Giokaris, Ph. D. Thesis, University of Chicago, 1981.
23. J. Hawkins, private communication.
24. W. F. Baker et al., Fermilab PUB-74/13 EXP, 1974;
H. W. Atherton et al., CERN 80-07, SPS Division, 1980.
25. A. Halling, M. Isaila and R. Sumner, IEEE Transactions on Nucl. Sci., NS-29, 437 (1982).

26. H. J. Frisch et al., IEEE Transactions on Nucl. Sci., NS-27, 150 (1980).

27. J. Badier et al., Zeit. Phys. C18, 281 (1983).

28. E. Eichten, I. Hinchliffe, K. Lane and C. Quigg, Rev. Mod. Phys. 56, 579 (1984).

29. A. S. Caroll et al., Phys. Lett. 80B, 319 (1979).

30. M. Swartz, Ph. D. Thesis, University of Chicago, 1984.

31. E. J. Moniz et al., Phys. Rev. Lett. 26, 445 (1971).

32. J. J. Aubert et al., Phys. Lett. 123B, 275 (1983);

A. Bodek et al., Phys. Rev. Lett. 50, 1431 (1983);

R. G. Arnold et al., Phys. Rev. Lett. 52, 727 (1984).

33. M. Mugge, private communication.

34. This error was based on the difference between the mean energy loss of Ref. 33 and the mean energy loss of muons in iron reported in the following document: C. Richard-Serre, CERN 71-18, 1971.

35. C. Adolphsen, private communication.

36. B. Betev et al., CERN-EP/85-04, 1985.

37. H. Abramowicz et al., Zeit. Phys. C17, 283 (1983).

38. D. B. MacFarlane et al., Zeit. Phys. C26, 1 (1984).

39. A. J. Buras and K. J. F. Gaemers, Nucl. Phys. B132, 249 (1977).

40. G. R. Farrar, Nucl. Phys. B77, 429 (1974).

41. The following experiments have measured the pion structure function:

NA10: see Ref. 36;

NA3: see Ref. 27;

CIP: C. B. Newman et al., Phys. Rev. Lett. 42, 951 (1979);

OMEGA: M. Corden et al., Phys. Lett. 96B, 417 (1980);

GOLIATH: R. Barate et al., Phys. Rev. Lett. 43, 1541 (1979).

42. K. J. Anderson et al., Phys. Rev. Lett. 42, 944 (1979).

43. O. Callot, Thesis, Orsay, Report LAL 81/05, 1981.

44. J. Badier et al., Phys. Lett. 117B, 372 (1982).

45. W. C. Davidon, Computer Journal 10, 406 (1968);
R. Fletcher and M. J. D. Powell, Computer Journal 6, 163 (1963);
W. C. Davidon, ANL-5990, 1959.

46. H. Wind, CERN/NP Internal Report, 72-08, 1972.

TABLE 1

QUARK FLAVORS

Name	Symbol	Electric Charge	Baryon Number	Approximate Mass
down	d	$-\frac{1}{3}$	$\frac{1}{3}$	8 MeV/c^2
up	u	$+\frac{2}{3}$	$\frac{1}{3}$	4 MeV/c^2
strange	s	$-\frac{1}{3}$	$\frac{1}{3}$	150 MeV/c^2
charm	c	$+\frac{2}{3}$	$\frac{1}{3}$	1.5 GeV/c^2
bottom	b	$-\frac{1}{3}$	$\frac{1}{3}$	4.7 GeV/c^2
top	t	$+\frac{2}{3}$	$\frac{1}{3}$	>22 GeV/c^2

TABLE 2

TOROID MAGNETS

Magnet	Mean inner radius (inches)	Outer radius (inches)	Length (inches)
TM1	2.67	24	55.88
TM2	4.51	35	55.75
A	6.69	47*	56.25
B	8.75	47*	56.25
C	10.81	47*	56.25
D	12.84	47*	56.25
E	14.91	47*	56.25

* Minor radius of octagon

TABLE 3

TRIGGER HODOSCOPES

Gap	Inner radius* (inches)	Outer radius* (inches)	Number of counters	Width of counters (inches)
1	5.125	23.625	5	4†
2	7.25	34.5	7	4‡
3	9.25	46.625	5	7.375
4	11.125	46.625	5	7
5	13.25	46.625	4	8.25
6	15.25	46.625	4	7.75
7	17.25	46.625	4	7.25

* Minor radius of octagon

† The width of the innermost counter was 2"

‡ The width of the innermost counter was 2.5"

TABLE 4

DRIFT CHAMBERS

Plane	Gap	Projection	Number of sense wires	Radius of inner wire* (inches)	Wire spacing* (inches)
1	1	X	18	6	1
2	1	U	18	6	1
3	2	X	27	8	1
4	2	U	27	8	1
5	3	X	37	10	1
6	3	U	37	10	1
7	4	X	35	12	1
8	4	U	35	12	1
9	5	X	33	14	1
10	5	U	33	14	1
11	6	X	31	16	1
12	6	U	31	16	1
13	7	X	29	18	1
14	7	U	29	18	1
15	1	X	32	4.625	.25

* Along the direction of the octant bisector

TABLE 5

OCTANT INEFFICIENCY SCHEMES

Scheme	Octant efficiency								Special
	1	2	3	4	5	6	7	8	efficiency*
1	.91	.77	.90	.93	1	.84	1	.81	1
2	1	.86	.93	.93	.92	.77	.95	.81	cut†
3	1	.86	.93	.93	.92	.77	.95	.81	.72

* Special inefficiency is associated with five octant pairs: (+,-)= (6,1), (7,2), (8,3), (1,4), (2,5)

† In this scheme the five special octant pairs are cut from the data

TABLE 6

MASS AND x_F DEPENDENCE OF CROSS SECTION FOR 4.5 GeV/c^2<M<8.5 GeV/c^2

M (GeV/c^2)	x_F	number of events	accidental background	acceptance (%)	$\frac{d\sigma}{dMdx_F}$ (nb/nucleon-GeV/c^2)
4.75	-.175	32	13.0 ± 3.9	0.20	.150 ± .057
	-.125	45	19.8 ± 4.9	0.28	.143 ± .049
	-.075	30	18.3 ± 4.8	0.33	.056 ± .035
	-.025	39	10.3 ± 3.6	0.47	.097 ± .025
	.025	75	10.3 ± 3.7	0.71	.145 ± .023
	.075	76	11.9 ± 4.1	0.72	.143 ± .023
	.125	51	10.8 ± 3.6	0.66	.098 ± .020
	.175	35	5.2 ± 2.4	0.34	.139 ± .032
5.25	-.175	33	8.3 ± 3.3	0.52	.077 ± .022
	-.125	48	12.5 ± 3.9	0.81	.071 ± .017
	-.075	35	12.1 ± 3.9	0.81	.045 ± .014
	-.025	71	7.3 ± 3.0	1.18	.087 ± .013
	.025	95	6.5 ± 2.9	1.39	.102 ± .013
	.075	106	5.1 ± 2.5	1.46	.111 ± .013
	.125	83	4.7 ± 2.4	1.12	.112 ± .015
	.175	43	3.0 ± 1.9	0.75	.086 ± .016
	.225	18	2.0 ± 1.6	0.40	.064 ± .019
5.75	-.175	44	4.7 ± 2.4	1.06	.060 ± .012
	-.125	44	5.8 ± 2.6	1.65	.037 ± .007
	-.075	71	7.4 ± 3.4	1.82	.056 ± .009
	-.025	77	4.9 ± 2.4	2.15	.054 ± .007
	.025	91	2.6 ± 1.8	2.27	.063 ± .008
	.075	93	2.7 ± 1.7	2.15	.068 ± .008
	.125	67	2.5 ± 1.9	2.08	.050 ± .007
	.175	66	1.0 ± 1.1	1.51	.069 ± .010
	.225	34	0.8 ± 1.0	0.85	.063 ± .012
	.275	6	0.4 ± 0.7	0.23	.038 ± .018

TABLE 6 (continued)

M (GeV/c²)	x_F	number of events	accidental background	acceptance (%)	$\frac{d\sigma}{dMdx_F}$ (nb/nucleon-GeV/c²)
6.25	-.175	36	2.4 ± 1.6	1.60	.034 ± .007
	-.125	63	2.6 ± 1.8	2.68	.036 ± .005
	-.075	61	2.6 ± 1.8	3.27	.029 ± .004
	-.025	103	2.1 ± 1.7	3.84	.042 ± .005
	.025	87	2.0 ± 1.7	4.05	.034 ± .004
	.075	77	1.3 ± 1.2	3.77	.032 ± .004
	.125	82	0.7 ± 0.8	2.91	.045 ± .006
	.175	58	0.6 ± 0.8	2.25	.041 ± .006
	.225	55	0.3 ± 0.6	1.62	.054 ± .008
	.275	8	0.2 ± 0.4	0.93	.014 ± .005
6.75	-.175	20	1.5 ± 1.3	2.49	.0119 ± .0031
	-.125	54	1.7 ± 1.4	3.57	.0236 ± .0037
	-.075	58	0.7 ± 0.9	4.19	.0220 ± .0033
	-.025	72	1.1 ± 1.2	5.38	.0212 ± .0029
	.025	91	0.9 ± 1.0	5.25	.0276 ± .0034
	.075	84	0.4 ± 0.7	4.99	.0270 ± .0034
	.125	81	0.4 ± 0.7	4.48	.0290 ± .0037
	.175	56	0.3 ± 0.6	3.32	.0271 ± .0041
	.225	44	0.6 ± 0.8	2.33	.0300 ± .0051
	.275	19	0.06 ± 0.3	1.66	.0184 ± .0045
	.325	8	0.10 ± 0.4	0.66	.0194 ± .0073
7.25	-.175	15	0.6 ± 0.8	3.41	.0068 ± .0019
	-.125	30	0.5 ± 0.8	4.83	.0098 ± .0020
	-.075	52	0.2 ± 0.5	6.13	.0136 ± .0021
	-.025	61	0.7 ± 0.9	6.40	.0152 ± .0022
	.025	79	0.5 ± 0.9	7.72	.0164 ± .0022
	.075	51	0.2 ± 0.5	5.31	.0154 ± .0024
	.125	59	0.3 ± 0.6	5.25	.0180 ± .0027
	.175	45	0.08 ± 0.3	4.38	.0165 ± .0027
	.225	33	0.08 ± 0.3	3.23	.0164 ± .0031
	.275	26	0.13 ± 0.4	2.59	.0161 ± .0034
	.325	16	0.05 ± 0.2	1.31	.0197 ± .0052

TABLE 6 (continued)

M (GeV/c^2)	x_F	number of events	accidental background	acceptance (%)	$\frac{d\sigma}{dMdx_F}$ (nb/nucleon-GeV/c^2)
7.75	-.175	28	0.31 ± 0.5	4.28	.0104 ± .0022
	-.125	19	0.19 ± 0.4	5.45	.0056 ± .0014
	-.075	42	0.16 ± 0.4	6.34	.0106 ± .0018
	-.025	49	0.08 ± 0.3	6.35	.0124 ± .0020
	.025	57	0.16 ± 0.4	7.82	.0117 ± .0018
	.075	45	0.11 ± 0.3	6.78	.0107 ± .0018
	.125	46	0.03 ± 0.2	6.64	.0112 ± .0018
	.175	45	0.02 ± 0.1	5.56	.0131 ± .0022
	.225	40	0.02 ± 0.1	4.13	.0156 ± .0027
	.275	29	0.08 ± 0.3	3.18	.0147 ± .0030
	.325	19	0.03 ± 0.2	1.89	.0162 ± .0040
	.375	8	0	0.93	.0138 ± .0051
8.25	-.175	12	0.11 ± 0.3	4.29	.0045 ± .0014
	-.125	23	0.23 ± 0.6	5.06	.0072 ± .0016
	-.075	41	0.12 ± 0.4	7.31	.0090 ± .0016
	-.025	41	0.13 ± 0.4	7.77	.0085 ± .0015
	.025	39	0.02 ± 0.1	8.75	.0072 ± .0013
	.075	55	0.04 ± 0.2	9.21	.0096 ± .0015
	.125	38	0	7.17	.0086 ± .0015
	.175	39	0.11 ± 0.4	6.89	.0091 ± .0017
	.225	36	0.05 ± 0.2	5.26	.0110 ± .0021
	.275	23	0	3.60	.0103 ± .0023
	.325	21	0	2.79	.0122 ± .0029
	.375	6	0	2.20	.0044 ± .0019

TABLE 7

PION STRUCTURE FUNCTION, FIT RESULTS

Nucleon Str. Func.	Evolving Pion?	Evolving Nucleon?	χ^2/d.o.f.	K	α_0^π	α_1^π	β_0^π	β_1^π	β^N	$\rho(\beta_1^\pi-\beta^N)$
EHLQ	No	Yes	73.1/67	2.70±.08	.5	0	1.21±.13	0	0	–
EHLQ	Yes	Yes	73.6/67	2.70±.08	.5	−.10	1.20±.12	.73	0	–
EHLQ	No	No	72.1/67	2.72±.08	.5	0	1.27±.13	0	0	–
CDHS*	No	Yes	74.6/67	2.94±.09	.5	0	1.21±.13	0	0	–
CCFRR*	No	Yes	74.6/67	2.58±.08	.5	0	1.19±.13	0	0	–
EHLQ$\cdot(1-x_2)^{\beta^N}$	No	Yes	72.4/66	2.56±.18	.5	0	1.20±.13	0	−.16±.19	.065
EHLQ	No	Yes	72.4/67	3.08±.10	.4	0	0.99±.12	0	0	–

* As parameterized by NA10[36]

TABLE 8

APPARATUS SYSTEMATIC ERRORS

Parameter (Error)	ΔK	$\Delta\beta$
Magnetic Field ($\pm 1\%$)	$\pm .02$	$\pm .08$
Mean Energy Loss of Muons in Iron ($\pm 5\%$)	$\pm .14$	$\pm .02$
Detector Geometry (Target z $\pm 1.5''$)	$\pm .03$	$\pm .05$
Drift Chamber Inefficiency	$\pm .09$	$\pm .01$
Trigger Inefficiency	$\pm .07$	$\pm .11$
Beam Energy ($\pm 7\%$)	$\pm .11$	$\pm .10$
Overall Normalization ($^{+15\%}_{-11\%}$)	$^{+.41}_{-.30}$	0
Total	$^{+.46}_{-.37}$	$\pm .18$

TABLE 9

PION STRUCTURE FUNCTION, OTHER EXPERIMENTS[41]

Experiment	α^{π}	β^{π}
GOLIATH	.5	1.57±.18
CIP	.5	1.27±.06
OMEGA	.44±.12	0.98±.15
NA3	.41±.04	0.95±.05
NA10*	.41±.03	1.02±.04

* This result included QCD leading log scaling violations.

TABLE 10

MASS DEPENDENCE OF CROSS SECTION

M (GeV/c^2)	Number of events	Accidental background	Acceptance (%)	$\frac{d\sigma}{dM}$ (nb/nucleon-GeV/c^2)
4.75	393	112 ± 12	0.22	$1.05 \pm .09 \times 10^{-1}$
5.25	544	72 ± 10	0.47	$8.08 \pm .46 \times 10^{-2}$
5.75	608	42 ± 7	0.88	$5.19 \pm .25 \times 10^{-2}$
6.25	648	20 ± 5	1.47	$3.43 \pm .15 \times 10^{-2}$
6.75	606	11.4 ± 3.6	2.17	$2.21 \pm .10 \times 10^{-2}$
7.25	490	5.7 ± 2.9	2.80	$1.39 \pm .07 \times 10^{-2}$
7.75	437	2.4 ± 1.6	3.44	$1.02 \pm .05 \times 10^{-2}$
8.25	386	1.1 ± 1.1	4.05	$7.65 \pm .42 \times 10^{-3}$
8.75	282	0.9 ± 1.0	4.33	$5.23 \pm .33 \times 10^{-3}$
9.25	239	0.5 ± 0.7	4.69	$4.09 \pm .28 \times 10^{-3}$
9.75	228	0.3 ± 0.5	5.02	$3.65 \pm .26 \times 10^{-3}$
10.25	132	0.2 ± 0.4	5.76	$1.84 \pm .17 \times 10^{-3}$
10.75	102	0.2 ± 0.5	6.19	$1.32 \pm .14 \times 10^{-3}$
11.25	62	0.08 ± 0.3	6.61	$7.53 \pm .98 \times 10^{-4}$
11.75	26	0.08 ± 0.3	7.29	$2.86 \pm .57 \times 10^{-4}$
12.25	17	0.03 ± 0.2	8.07	$1.69 \pm .41 \times 10^{-4}$
12.75	13	0.03 ± 0.2	9.29	$1.12 \pm .31 \times 10^{-4}$
13.25	9	0.02 ± 0.2	9.72	$7.40 \pm 2.49 \times 10^{-5}$
13.75	7	0	11.65	$4.81 \pm 1.83 \times 10^{-5}$
14.25	5	0	13.23	$3.02 \pm 1.36 \times 10^{-5}$
14.75	2	0	14.73	$1.08 \pm .77 \times 10^{-5}$
15.25	2	0.03 ± 0.2	17.64	$8.90 \pm 6.44 \times 10^{-6}$

TABLE 11

x_F DEPENDENCE OF CROSS SECTION FOR $M>11$ GeV/c^2

x_F	Number of events	Accidental background	Acceptance (%)	$\frac{d\sigma}{dx_F}$ (pb/nucleon)
-.25	3	.02 ± .15	9.81	0.12 ± .07
-.15	4	.06 ± .30	9.83	0.16 ± .08
-.05	21	0	10.48	0.81 ± .18
.05	41	0	11.47	1.45 ± .23
.15	21	0	9.83	0.87 ± .19
.25	19	0	8.83	0.88 ± .20
.35	16	0	5.37	1.22 ± .31
.45	14	0	3.86	1.48 ± .40
.55	3	0	2.59	0.47 ± .27
.65	1	0	2.36	0.15 ± .15

TABLE 12

p_T DEPENDENCE OF CROSS SECTION IN SEVERAL MASS RANGES

Mass range (GeV/c^2)	p_T (GeV/c)	Number of events	Accidental background	Acceptance (%)	$\frac{d\sigma}{p_T dp_T}$ (pb/nucleon-$(GeV/c)^2$)
4.5-5.5	.25	21	0.6 ± 0.8	.08	$9.03 \pm 2.13 \times 10^{-2}$
	.75	133	3.8 ± 2.4	.14	$1.03 \pm .10 \times 10^{-1}$
	1.25	215	13.1 ± 4.1	.29	$4.63 \pm .38 \times 10^{-2}$
	1.75	230	25.6 ± 5.6	.56	$1.68 \pm .14 \times 10^{-2}$
	2.25	157	31.3 ± 6.2	.79	$5.55 \pm .65 \times 10^{-3}$
	2.75	97	31.1 ± 6.2	1.07	$1.73 \pm .32 \times 10^{-3}$
	3.25	45	25.0 ± 5.6	1.33	$3.51 \pm 1.55 \times 10^{-4}$
5.5-6.5	.25	113	0.5 ± 0.8	.69	$5.56 \pm .55 \times 10^{-2}$
	.75	316	1.7 ± 1.4	.83	$4.24 \pm .26 \times 10^{-2}$
	1.25	315	4.5 ± 2.3	1.12	$1.82 \pm .11 \times 10^{-2}$
	1.75	247	7.4 ± 3.2	1.49	$7.35 \pm .53 \times 10^{-3}$
	2.25	134	8.3 ± 3.2	1.87	$2.35 \pm .24 \times 10^{-3}$
	2.75	64	8.2 ± 3.1	2.14	$7.37 \pm 1.19 \times 10^{-4}$
	3.25	30	7.9 ± 3.2	2.77	$1.90 \pm .56 \times 10^{-4}$
	3.75	19	7.3 ± 3.1	2.92	$8.22 \pm 3.85 \times 10^{-5}$
6.5-7.5	.25	126	0.4 ± 0.6	2.28	$1.85 \pm .17 \times 10^{-2}$
	.75	301	0.6 ± 0.9	2.28	$1.46 \pm .09 \times 10^{-2}$
	1.25	312	1.0 ± 1.1	2.35	$8.70 \pm .54 \times 10^{-3}$
	1.75	189	1.3 ± 1.2	2.47	$3.49 \pm .28 \times 10^{-3}$
	2.25	103	1.8 ± 1.4	2.98	$1.19 \pm .13 \times 10^{-3}$
	2.75	30	2.1 ± 1.6	3.31	$2.35 \pm .50 \times 10^{-4}$
	3.25	18	2.0 ± 1.6	4.02	$9.13 \pm 2.70 \times 10^{-5}$
	3.75	11	2.5 ± 2.1	3.95	$4.17 \pm 2.00 \times 10^{-5}$

TABLE 12 (continued)

Mass range (GeV/c^2)	p_T (GeV/c)	Number of events	Accidental background	Acceptance (%)	$\frac{d\sigma}{p_T dp_T}$ (pb/nucleon-$(GeV/c)^2$)
7.5-8.5	.25	111	0.0 ± 0.2	3.52	$1.07 \pm .11 \times 10^{-2}$
	.75	246	0.0 ± 0.1	3.37	$8.14 \pm .55 \times 10^{-3}$
	1.25	215	0.2 ± 0.6	3.62	$3.88 \pm .29 \times 10^{-3}$
	1.75	132	0.2 ± 0.5	3.92	$1.54 \pm .15 \times 10^{-3}$
	2.25	67	0.1 ± 0.3	4.32	$5.43 \pm .71 \times 10^{-4}$
	2.75	24	0.6 ± 0.9	5.00	$1.33 \pm .30 \times 10^{-4}$
	3.25	16	0.2 ± 0.5	6.47	$5.82 \pm 1.59 \times 10^{-5}$
	3.75	9	0.5 ± 0.7	6.68	$2.62 \pm 1.02 \times 10^{-5}$
	4.25	2	0.3 ± 0.6	8.28	$3.81 \pm 3.40 \times 10^{-6}$
4.5-8.5	.25	371	1.5 ± 1.3	.63	$1.98 \pm .11 \times 10^{-1}$
	.75	996	6.2 ± 2.9	.69	$1.60 \pm .05 \times 10^{-1}$
	1.25	1057	18.8 ± 4.9	.87	$7.78 \pm .27 \times 10^{-2}$
	1.75	798	34.6 ± 6.6	1.16	$3.01 \pm .12 \times 10^{-2}$
	2.25	461	41.5 ± 7.2	1.46	$1.00 \pm .06 \times 10^{-2}$
	2.75	215	42.0 ± 7.2	1.76	$2.77 \pm .27 \times 10^{-3}$
	3.25	109	35.2 ± 6.7	2.20	$7.93 \pm 1.36 \times 10^{-4}$
	3.75	60	30.4 ± 6.3	2.43	$2.47 \pm .84 \times 10^{-4}$
>11	.25	16	0	5.59	$9.71 \pm 2.45 \times 10^{-4}$
	.75	27	0	6.09	$4.94 \pm .96 \times 10^{-4}$
	1.25	29	0	7.36	$2.58 \pm .49 \times 10^{-4}$
	1.75	35	0	9.49	$1.69 \pm .29 \times 10^{-4}$
	2.25	13	0	13.33	$3.44 \pm .97 \times 10^{-5}$
	2.75	11	0	21.62	$1.45 \pm .45 \times 10^{-5}$
	3.25	8	0	29.63	$6.50 \pm 2.38 \times 10^{-6}$
	3.75	4	0	55.97	$1.49 \pm .77 \times 10^{-6}$

TABLE 13

MEAN p_T AND p_T^2 FOR SEVERAL MASS RANGES

Mass range (GeV/c^2)	$<p_T>$ (GeV/c)	$<p_T^2>$ $(GeV/c)^2$
4.5-5.5	1.142 ± .029 ± .049	1.659 ± .073 ± .125
5.5-6.5	1.120 ± .019 ± .027	1.663 ± .054 ± .083
6.5-7.5	1.197 ± .020 ± .022	1.837 ± .060 ± .064
7.5-8.5	1.156 ± .022 ± .026	1.769 ± .067 ± .092
4.5-8.5	1.147 ± .011 ± .020	1.712 ± .031 ± .062
>11	1.205 ± .055 ± .024	1.936 ± .145 ± .074

The first error is statistical and the second error is systematic.

TABLE 14

EHLQ EXPONENTS, a

flavor	a
up valence	3
down valence	4
up & down sea	7
strange sea	7

TABLE 15

EHLQ COEFFICIENTS, c_{ij}

		i					
flavor	j	0	1	2	3	4	5
up valence	0	+0.77211	−0.20889	−0.33113	−0.02638	−0.01652	−0.00024
	1	−0.52894	−0.26450	+0.32259	+0.12139	+0.02579	+0.00893
	2	+0.21304	+0.18412	−0.08628	−0.06727	−0.01859	−0.00597
	3	−0.08961	−0.09573	+0.01589	+0.02644	+0.00951	+0.00308
	4	+0.03531	+0.04188	−0.00029	−0.00869	−0.00380	−0.00129
	5	−0.01502	−0.01943	−0.00245	+0.00264	+0.00146	+0.00054
down valence	0	+0.38389	−0.08068	−0.16369	−0.02245	−0.00886	−0.00067
	1	−0.29290	−0.14268	+0.16783	+0.06758	+0.01553	+0.00480
	2	+0.12336	+0.10193	−0.04866	−0.03797	−0.01104	−0.00339
	3	−0.05324	−0.05447	+0.01019	+0.01565	+0.00578	+0.00183
	4	+0.02131	+0.02428	−0.00081	−0.00541	−0.00239	−0.00080
	5	−0.00921	−0.01148	−0.00111	+0.00177	+0.00096	+0.00035
up & down sea	0	+0.07343	−0.06526	+0.03509	−0.00291	+0.00584	+0.00011
	1	−0.01744	−0.00187	+0.00716	−0.00913	+0.00138	−0.00178
	2	−0.00636	−0.00021	−0 00788	−0.00057	−0.00182	−0.00055
	3	+0.00761	+0.00432	+0.00432	+0.00221	+0.00134	+0.00071
	4	−0.00446	−0.00345	−0.00190	−0.00131	−0.00068	−0.00038
	5	+0.00262	+0.00239	+0.00086	+0.00061	+0.00029	+0.00016
strange sea	0	+0.05414	−0.03819	+0.02615	−0.00082	+0.00525	+0.00035
	1	−0.00571	−0.01484	+0.00725	−0.00749	+0.00103	−0.00157
	2	−0.01022	+0.00330	−0.00680	−0.00132	−0.00173	−0.00060
	3	+0.00897	+0.00328	+0.00370	+0.00245	+0.00133	+0.00072
	4	−0.00493	−0.00314	−0.00163	−0.00139	−0.00068	−0.00038
	5	+0.00279	+0.00229	+0.00074	+0.00063	+0.00030	+0.00016

TABLE 16

EHLQ COEFFICIENTS, d_{ij}

		i					
flavor	j	0	1	2	3	4	5
up valence	0	+0.24048	+0.29194	+0.09841	+0.02174	+0.00353	+0.00054
	1	+0.01848	−0.00472	−0.02624	−0.01883	−0.00783	−0.00263
	2	−0.00587	−0.00525	+0.00094	+0.00238	+0.00147	+0.00070
	3	+0.00175	+0.00199	+0.00033	−0.00031	−0.00028	−0.00016
	4	−0.00053	−0.00065	−0.00017	+0.00004	+0.00006	+0.00004
	5	+0.00017	+0.00023	+0.00008	+0.00001	−0.00001	−0.00001
down valence	0	+0.12672	+0.13615	+0.03988	+0.00835	+0.00170	+0.00046
	1	+0.00444	−0.01088	−0.01594	−0.00945	−0.00364	−0.00120
	2	−0.00199	−0.00069	+0.00152	+0.00153	+0.00080	+0.00036
	3	+0.00065	+0.00051	−0.00013	−0.00028	−0.00017	−0.00009
	4	−0.00020	−0.00019	−0.00000	+0.00006	+0.00004	+0.00002
	5	+0.00007	+0.00008	+0.00002	−0.00001	−0.00001	−0.00001
up & down sea	0	+1.03742	−1.12935	+0.34131	−0.07490	+0.00884	−0.00089
	1	+0.94925	−1.31366	+0.45441	−0.09849	+0.01413	−0.00114
	2	+0.04985	−0.12988	+0.08680	−0.02614	+0.00474	−0.00060
	3	−0.02798	+0.05052	−0.01819	+0.00174	+0.00024	−0.00005
	4	+0.00729	−0.01145	+0.00165	+0.00069	−0.00021	−0.00000
	5	−0.00174	+0.00230	+0.00042	−0.00036	+0.00004	+0.00001
strange sea	0	+0.94651	−1.10836	+0.35214	−0.07257	+0.00913	−0.00092
	1	+0.95694	−1.30198	+0.45809	−0.09837	+0.01375	−0.00133
	2	+0.04845	−0.13237	+0.08558	−0.02647	+0.00471	−0.00057
	3	−0.02763	+0.05118	−0.01783	+0.00187	+0.00027	−0.00005
	4	+0.00719	−0.01163	+0.00154	+0.00064	−0.00022	−0.00000
	5	−0.00171	+0.00235	+0.00045	−0.00035	+0.00005	+0.00001

TABLE 17

NA10 PATAMETERIZATION OF CDHS STRUCTURE FUNCTIONS

$$\alpha_1 = 0.3543 + 0.4122\bar{s}$$

$$\alpha_2 = 1.5760 + 2.0170\bar{s}$$

$$\beta_V = 3.8330 + 2.8680\bar{s}$$

$$\gamma = 11.57$$

$$C = (0.50758 + 0.23006\bar{s} + 0.06734\bar{s}^2)/2.8$$

$$\beta_s = 7.417 - 1.138\bar{s} + 13.22\bar{s}^2 - 4.966\bar{s}^3 - 1.86\bar{s}^4$$

TABLE 18

NA10 PARAMETERIZATION OF CCFRR STRUCTURE FUNCTIONS

$\alpha_1 = 0.6190 + 0.1678\overline{s}$
α_2 undefined
$\beta_V = 2.8670 + 0.6687\overline{s}$
$\gamma = 0$

Figure 1.— The lowest order Feynman diagram for Drell-Yan production.

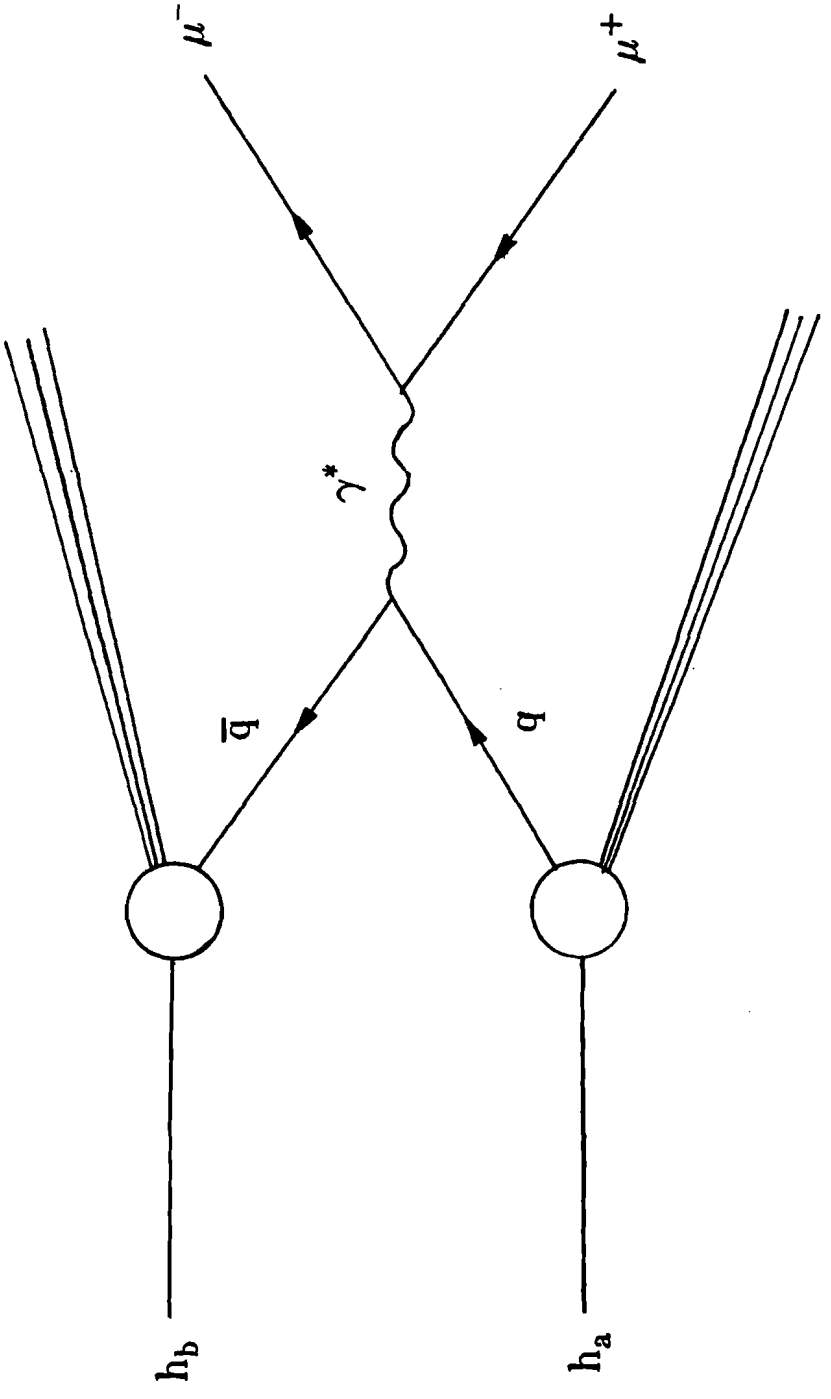
μ^-
μ^+
γ^*
$\bar{q}$
q
h_b
h_a

Figure 2.— The basic subprocess and higher order QCD subprocesses contributing to the Drell-Yan process.

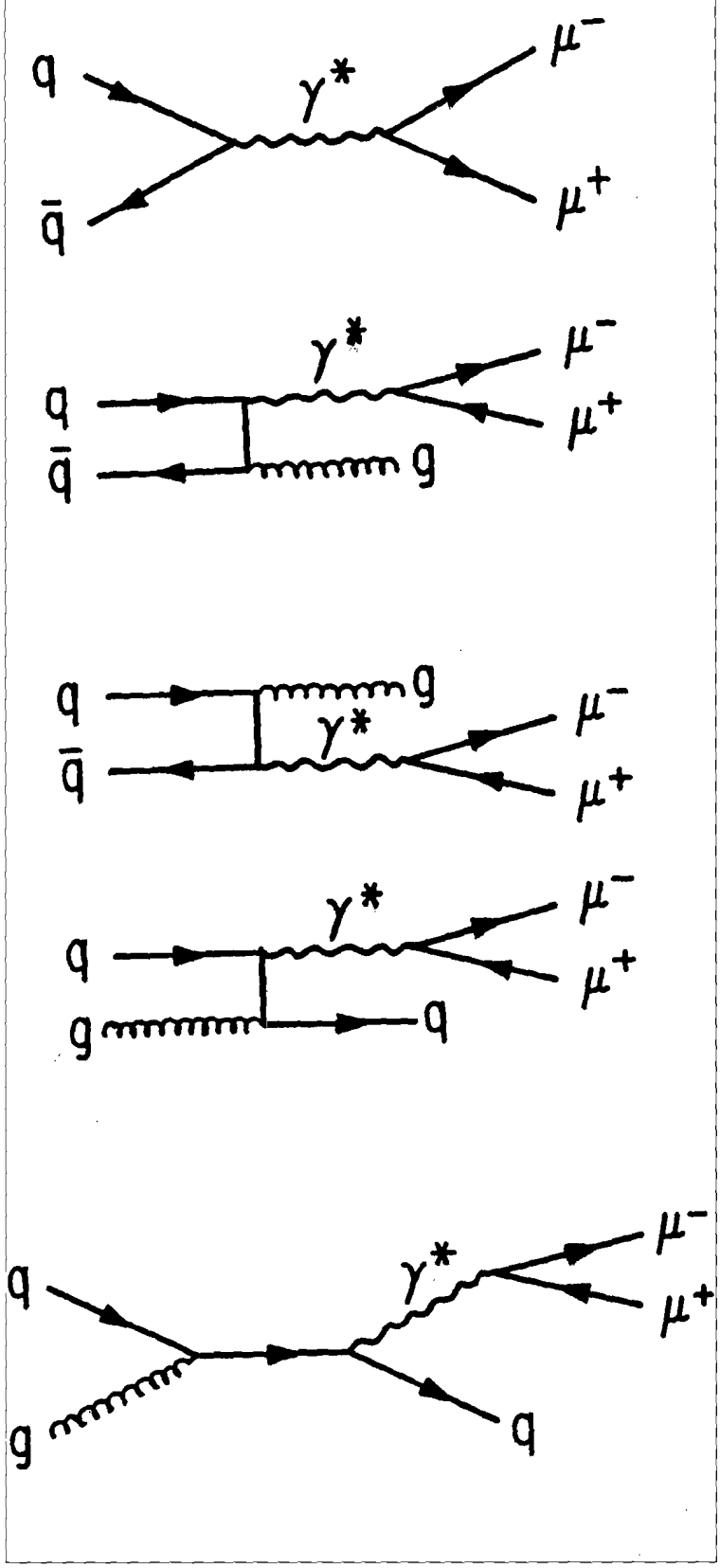
q
$\bar{q}$
γ^*
μ^-
μ^+
q
$\bar{q}$
g
γ^*
μ^-
μ^+
q
$\bar{q}$
g
γ^*
μ^-
μ^+
g
q
γ^*
μ^-
μ^+
q
g
γ^*
μ^-
μ^+
q

Figure 3.— Plan view of the E-326 detector. An end view is shown in section A-A'.

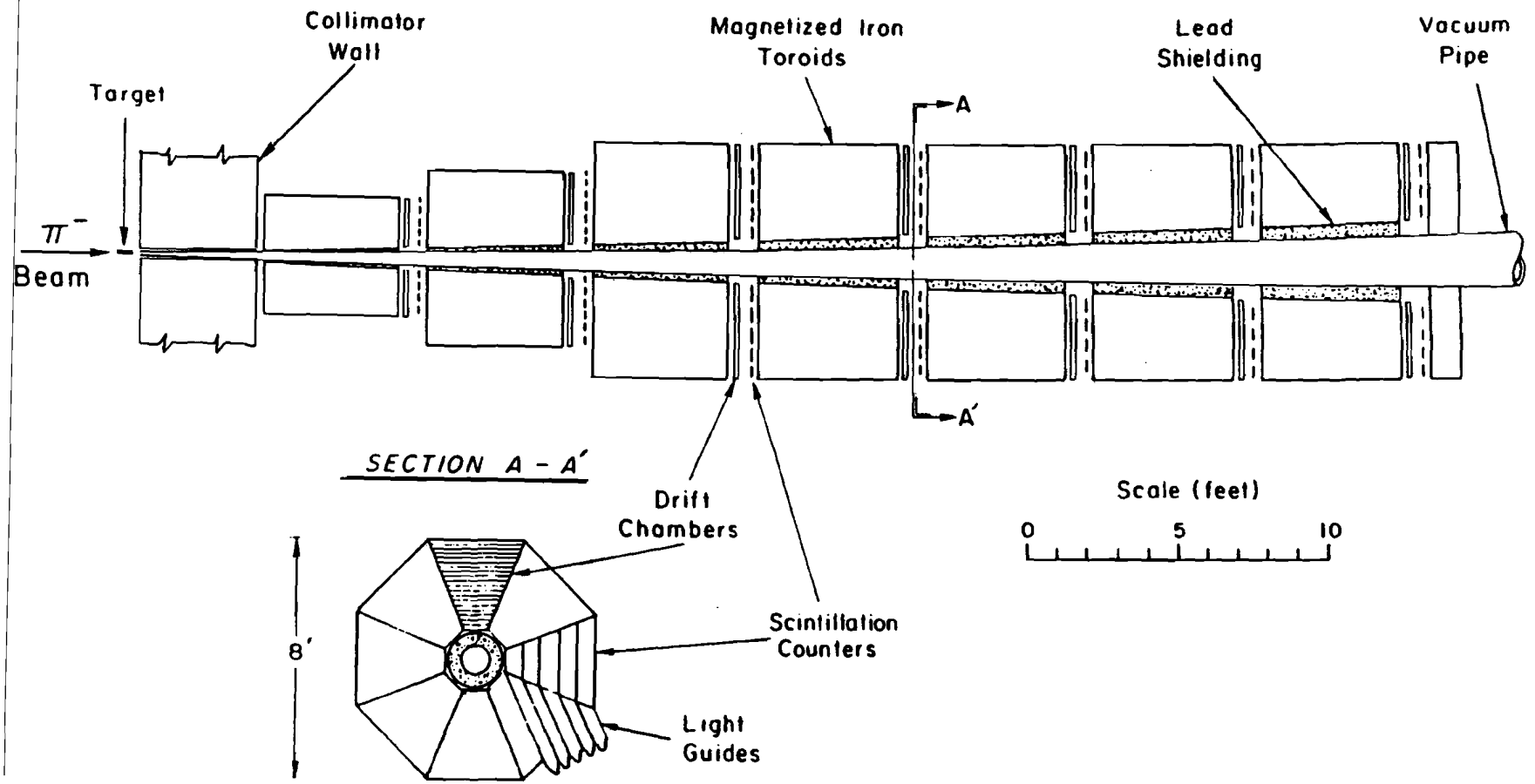
Collimator Wall
Target
Magnetized Iron Toroids
Lead Shielding
Vacuum Pipe
A
A'
π⁻ Beam
SECTION A - A'
Drift Chambers
Scintillation Counters
Light Guides
8'
Scale (feet)
0
5
10

Figure 4.— Plan view of the P-West secondary beamline.

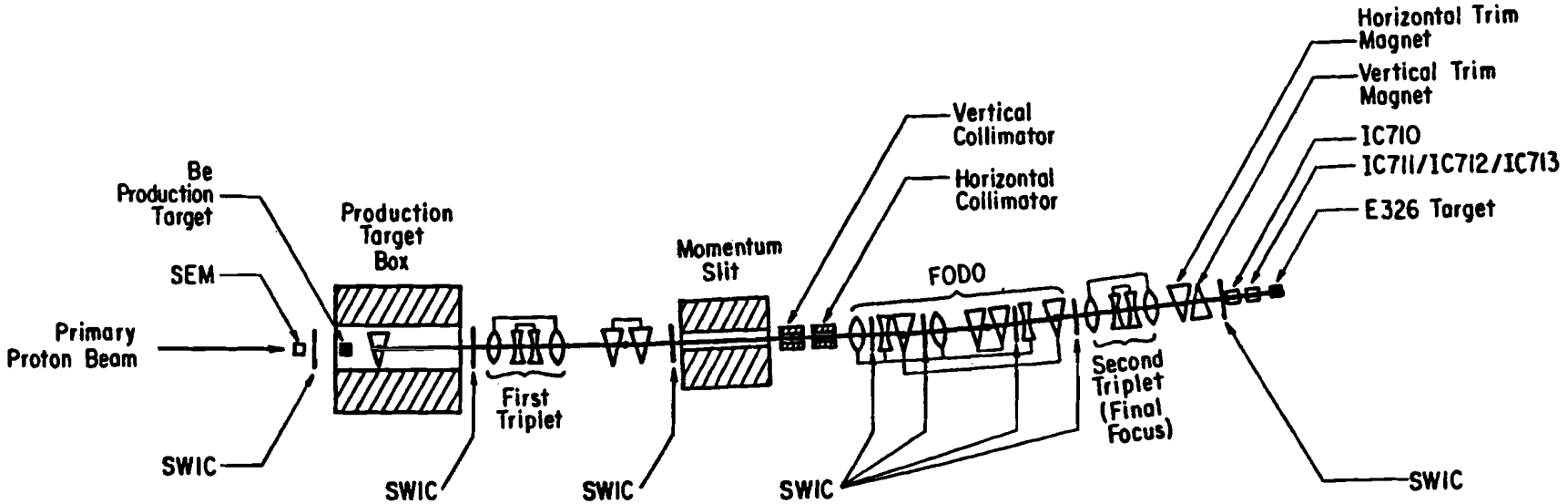
Be
Production
Target
SEM
Primary
Proton Beam
SWIC
Production
Target
Box
SWIC
First
Triplet
SWIC
Momentum
Slit
Vertical
Collimator
Horizontal
Collimator
SWIC
FODO
Second
Triplet
(Final
Focus)
Horizontal Trim
Magnet
Vertical Trim
Magnet
IC710
IC711/IC712/IC713
E326 Target
SWIC
0 10 20
Scale (m)
Quadrupole Focussing in the Horizontal Plane
Quadrupole Focussing in the Vertical Plane
Dipole
Steel Collimator

Figure 5.— Gap 3 trigger hodoscope (see section A-A' in Figure 3).

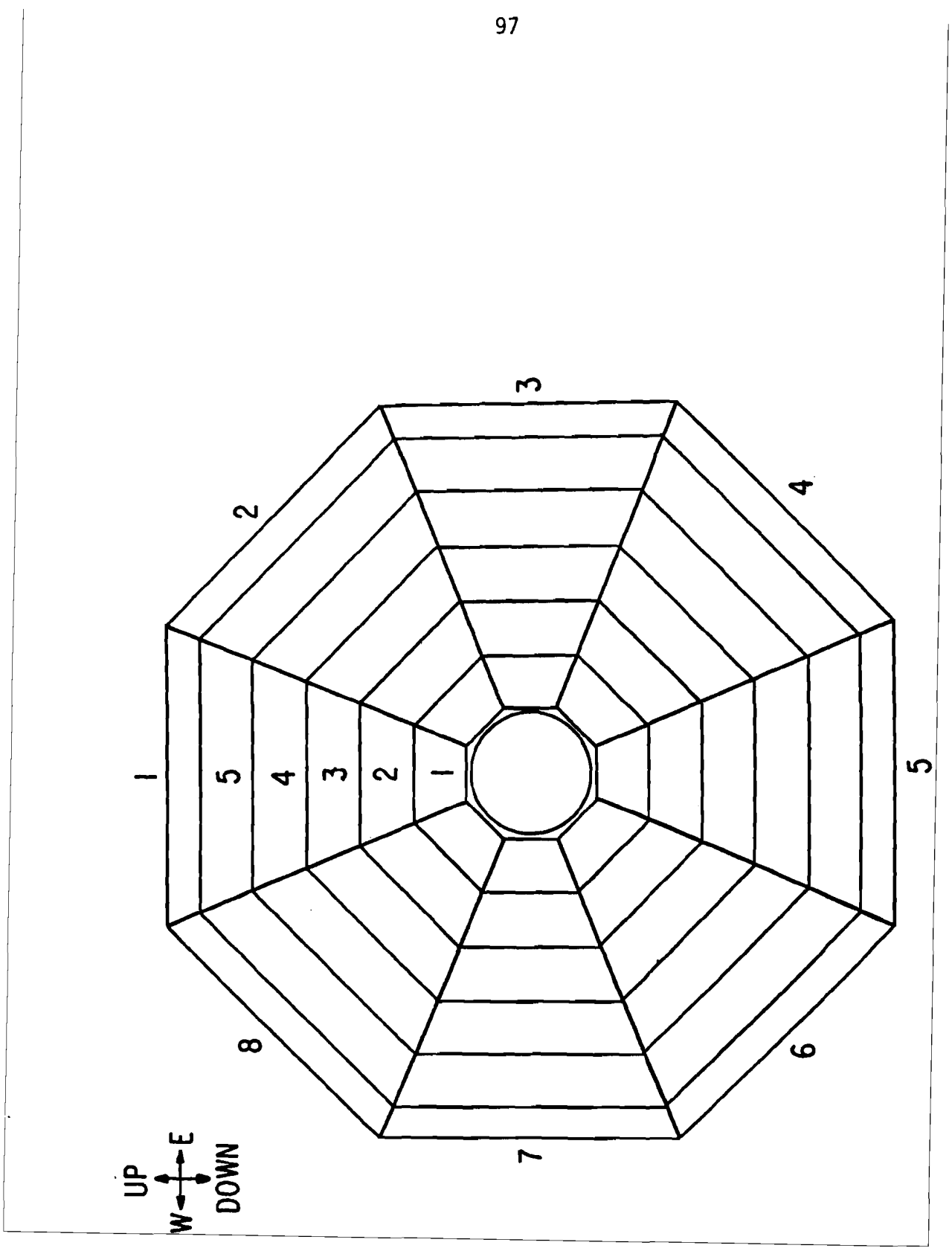
1
2
3
4
5
6
7
8
1
2
3
4
5
UP
DOWN
W
E

Figure 6.— Block diagram of the E-326 trigger.

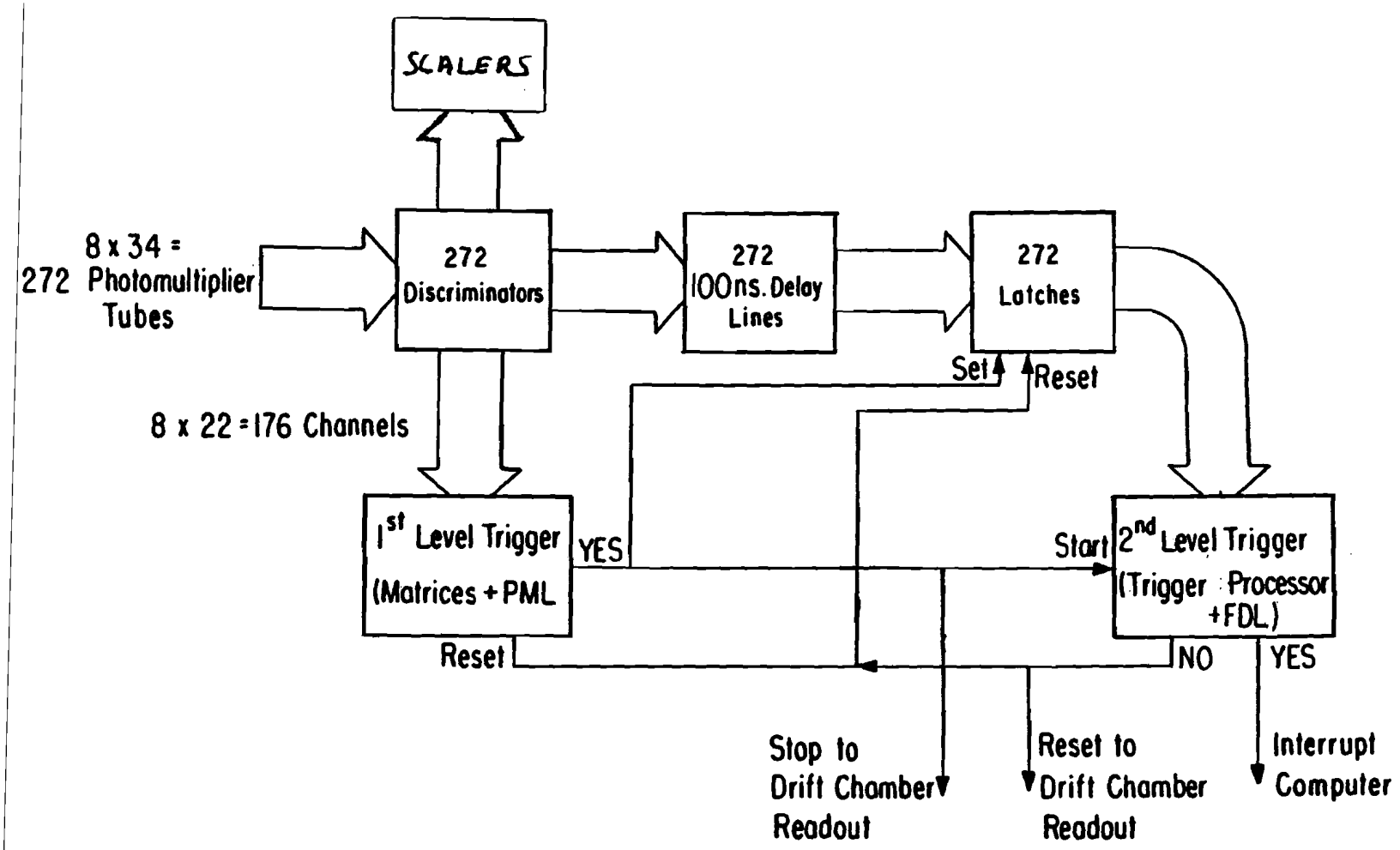
SCALERS
8 x 34 = 272 Photomultiplier Tubes
272 Discriminators
272 100ns. Delay Lines
272 Latches
Set
Reset
8 x 22 = 176 Channels
1st Level Trigger (Matrices + PML
YES
Start
2nd Level Trigger (Trigger Processor +FDL)
Reset
NO
YES
Stop to Drift Chamber Readout
Reset to Drift Chamber Readout
Interrupt Computer

Figure 7.— Trigger coincidence matrices in one octant. The labels Gn Pm refer to the mth trigger counter in the nth gap.

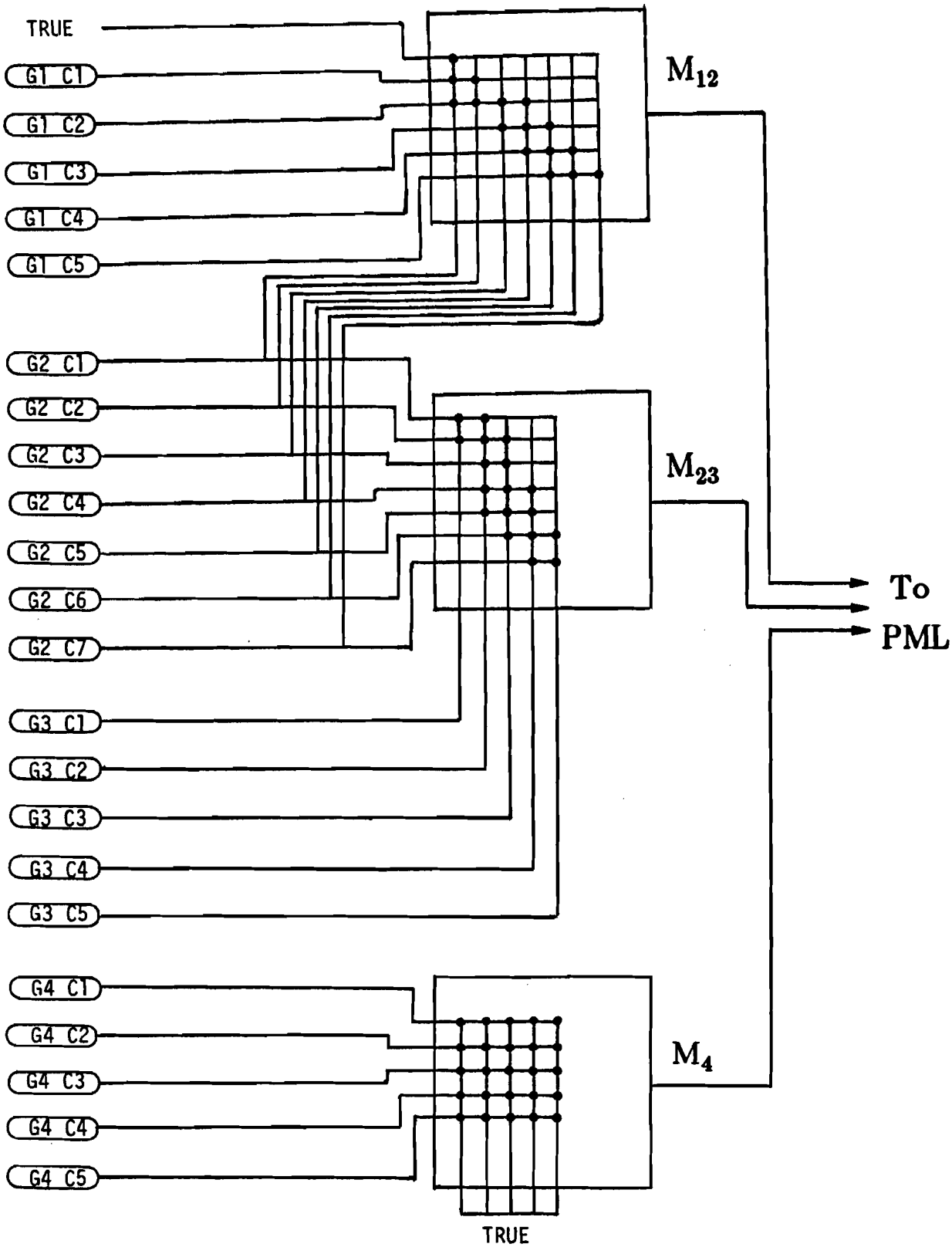
TRUE
G1 C1
G1 C2
G1 C3
G1 C4
G1 C5
G2 C1
G2 C2
G2 C3
G2 C4
G2 C5
G2 C6
G2 C7
G3 C1
G3 C2
G3 C3
G3 C4
G3 C5
G4 C1
G4 C2
G4 C3
G4 C4
G4 C5
TRUE
M_{12}
M_{23}
M_4
To
PML

Figure 8.— Schematic diagram of the post matrix logic (PML).

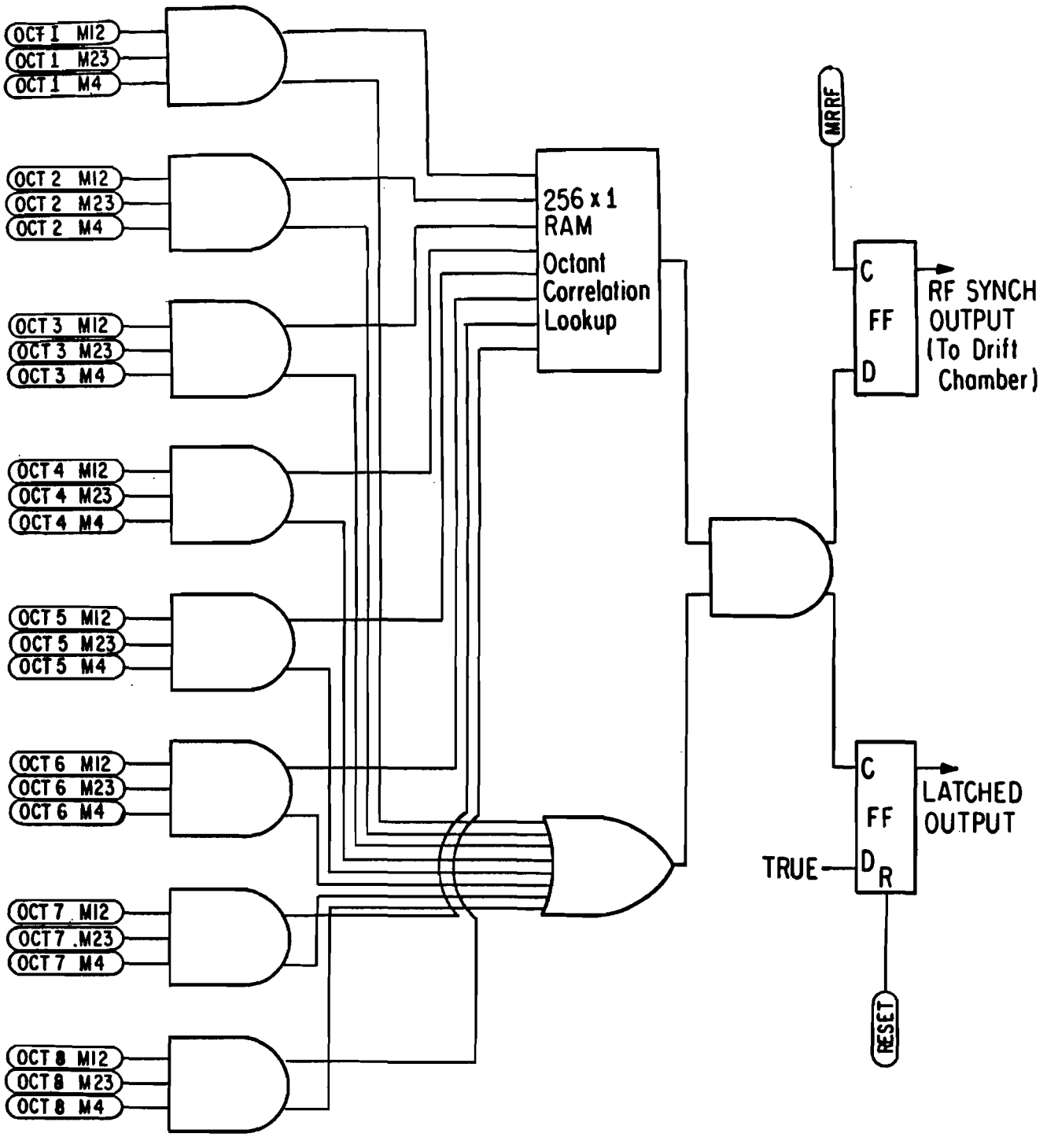
OCT 1 M12
OCT 1 M23
OCT 1 M4
OCT 2 M12
OCT 2 M23
OCT 2 M4
OCT 3 M12
OCT 3 M23
OCT 3 M4
OCT 4 M12
OCT 4 M23
OCT 4 M4
OCT 5 M12
OCT 5 M23
OCT 5 M4
OCT 6 M12
OCT 6 M23
OCT 6 M4
OCT 7 M12
OCT 7 M23
OCT 7 M4
OCT 8 M12
OCT 8 M23
OCT 8 M4
256 x 1
RAM
Octant
Correlation
Lookup
MRRF
C
FF
D
RF SYNCH
OUTPUT
(To Drift
Chamber)
C
FF
D
R
LATCHED
OUTPUT
TRUE
RESET

Figure 9.— Schematic diagram of the second level trigger.

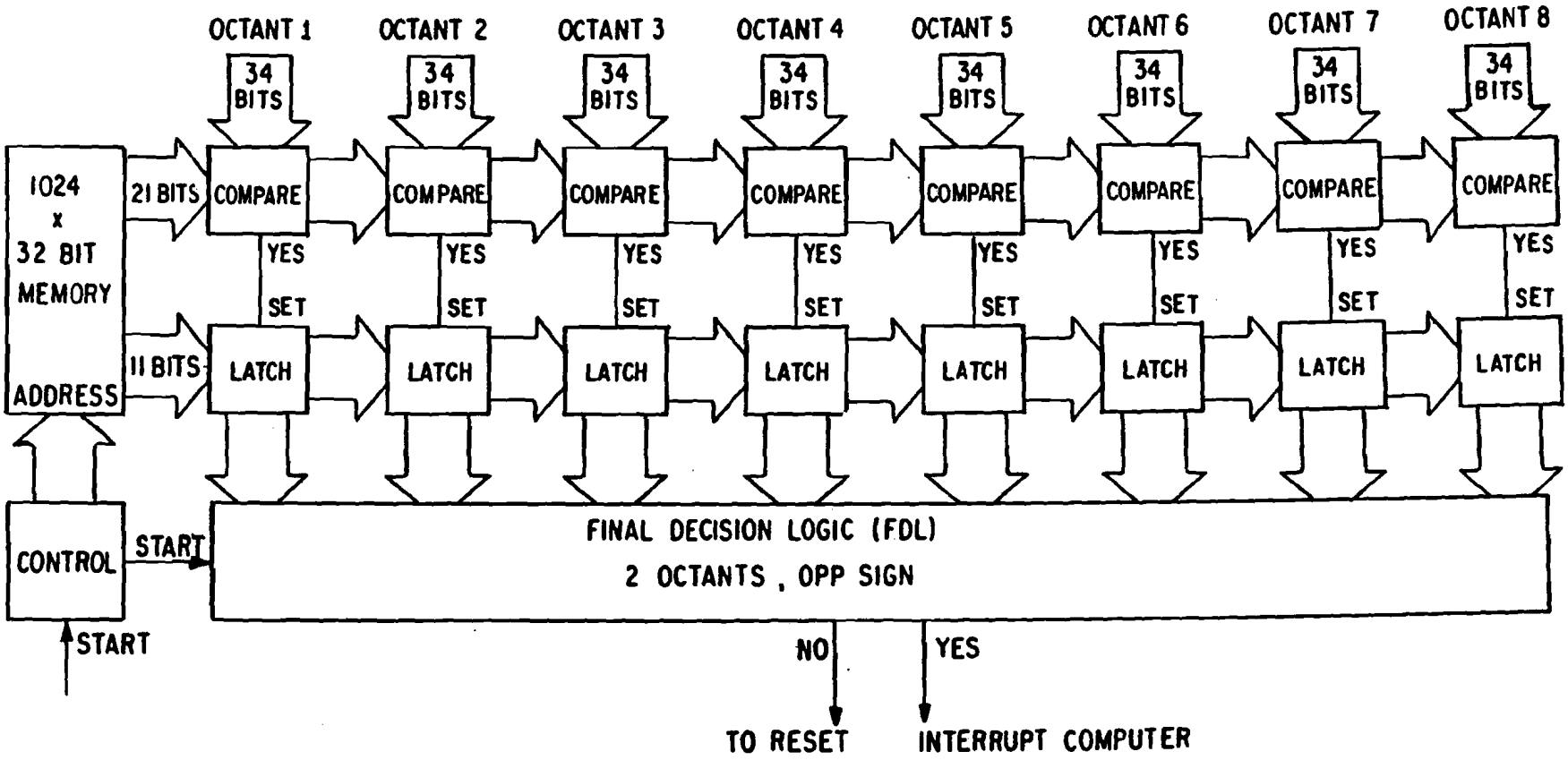
OCTANT 1
OCTANT 2
OCTANT 3
OCTANT 4
OCTANT 5
OCTANT 6
OCTANT 7
OCTANT 8
34 BITS
1024 x 32 BIT MEMORY
ADDRESS
21 BITS
11 BITS
COMPARE
YES
SET
LATCH
CONTROL
START
FINAL DECISION LOGIC (FDL)
2 OCTANTS , OPP SIGN
NO
YES
TO RESET
INTERRUPT COMPUTER

Figure 10.— Side view of drift cells of original drift chambers.

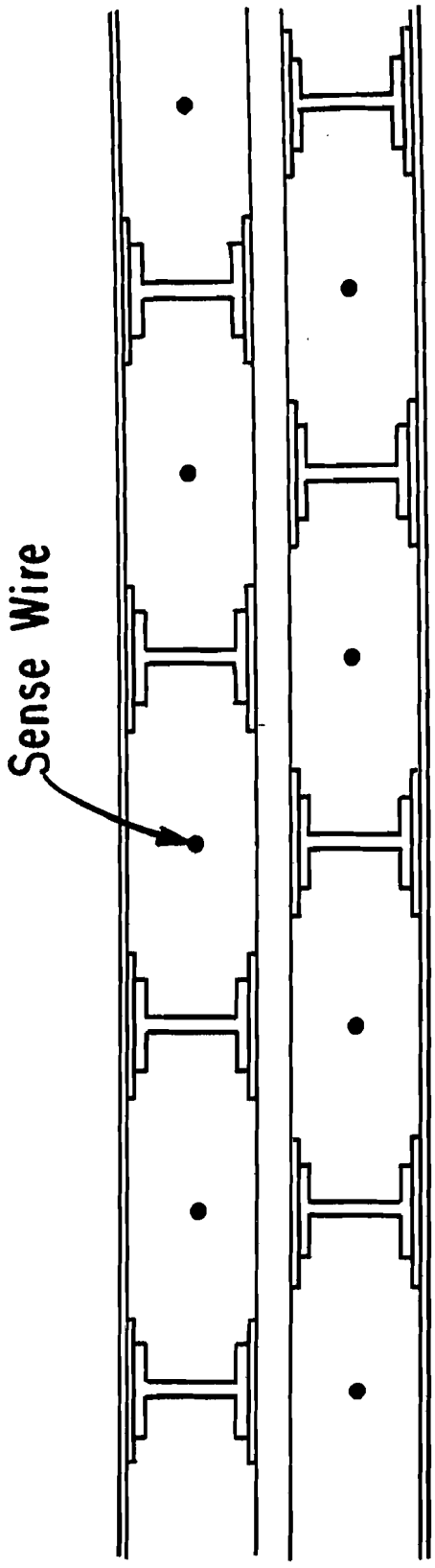
Sense Wire

Figure 11.— Side view of drift cells of new drift chambers in gap 1.

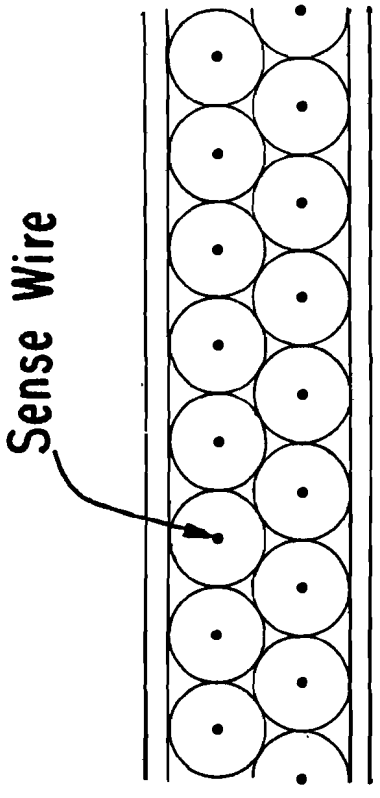
Sense Wire

Figure 12.— The efficiency of the original drift chambers in gap 1 as a function of distance from the beam.

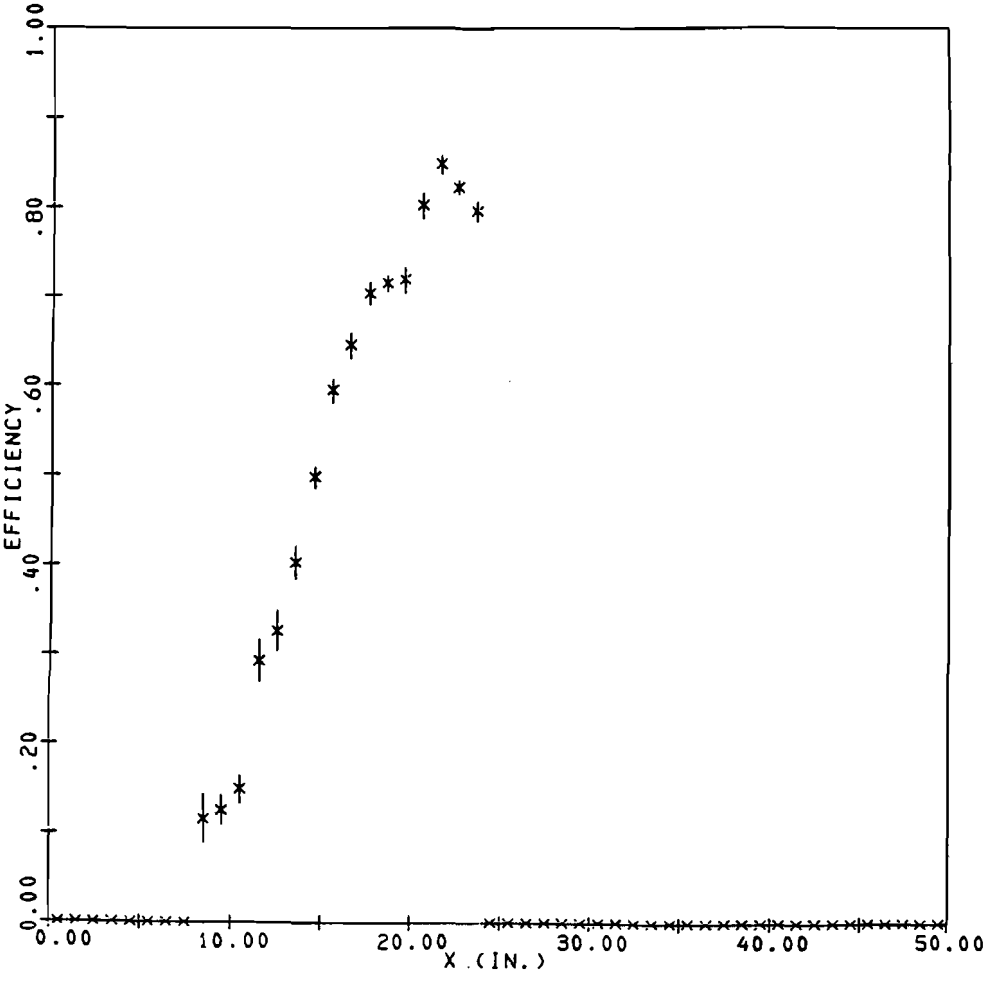
EFFICIENCY
1.00
.80
.60
.40
.20
0.00
0.00
10.00
20.00
30.00
40.00
50.00
X (IN.)

Figure 13.— The efficiency of the gap 2 drift chambers as a function of distance from the beam.

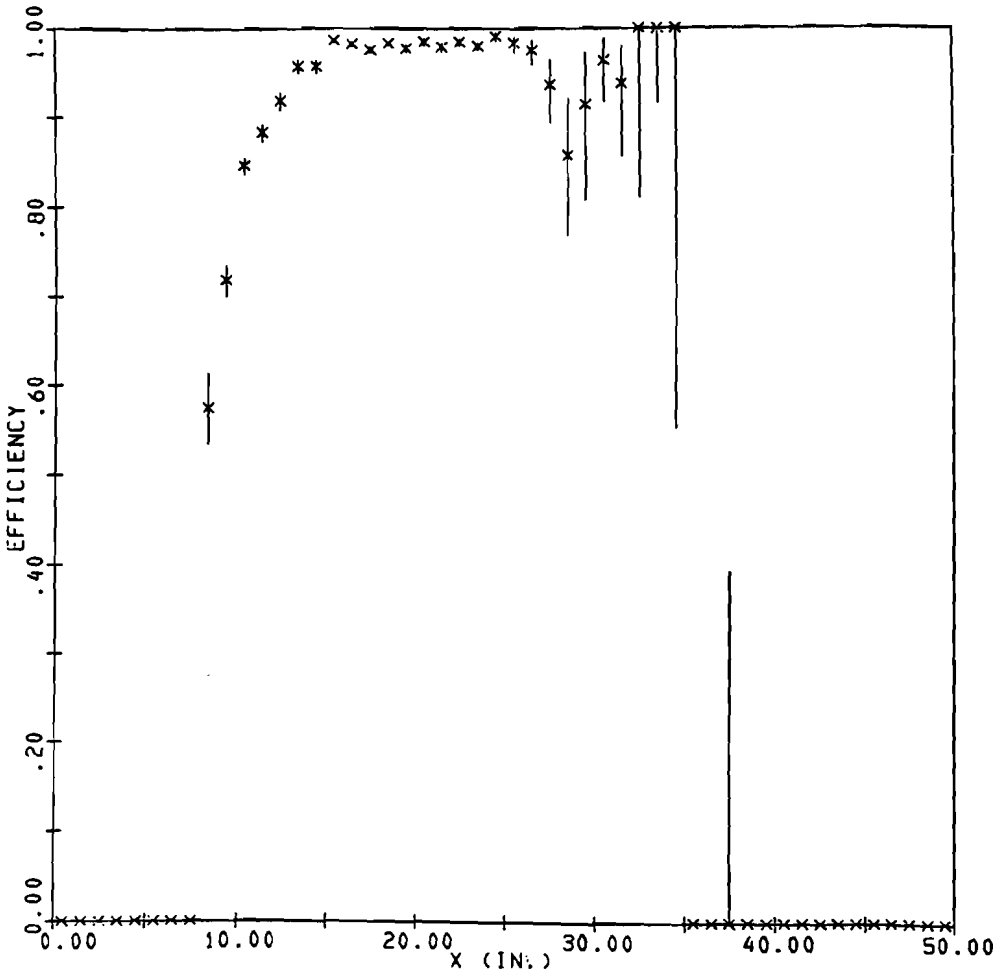
EFFICIENCY
1.00
.80
.60
.40
.20
0.00
0.00
10.00
20.00
30.00
40.00
50.00
X (IN.)

Figure 14.— The efficiency of the gap 3 drift chambers as a function of distance from the beam.

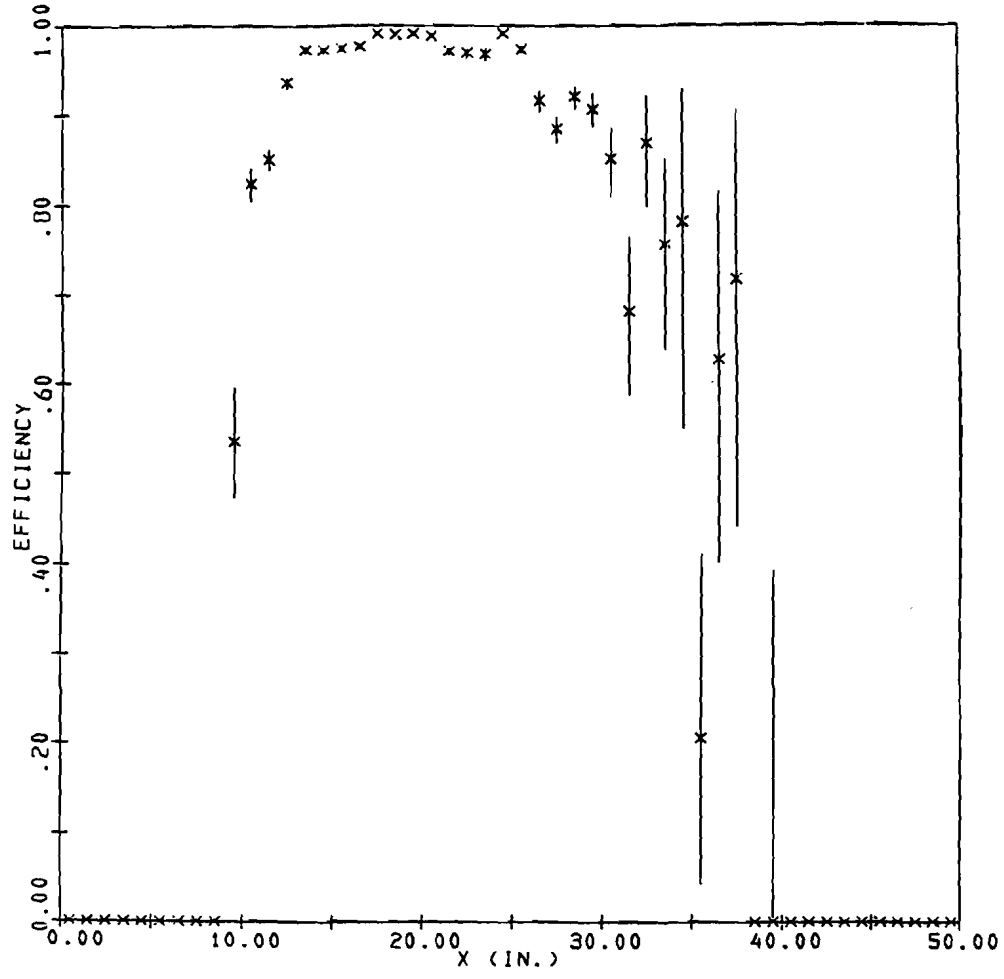
EFFICIENCY
1.00
.80
.60
.40
.20
0.00
0.00
10.00
20.00
30.00
40.00
50.00
X (IN.)

Figure 15.— A comparison of the octant distribution of tracks in the data and the Monte Carlo (before applying any correction).

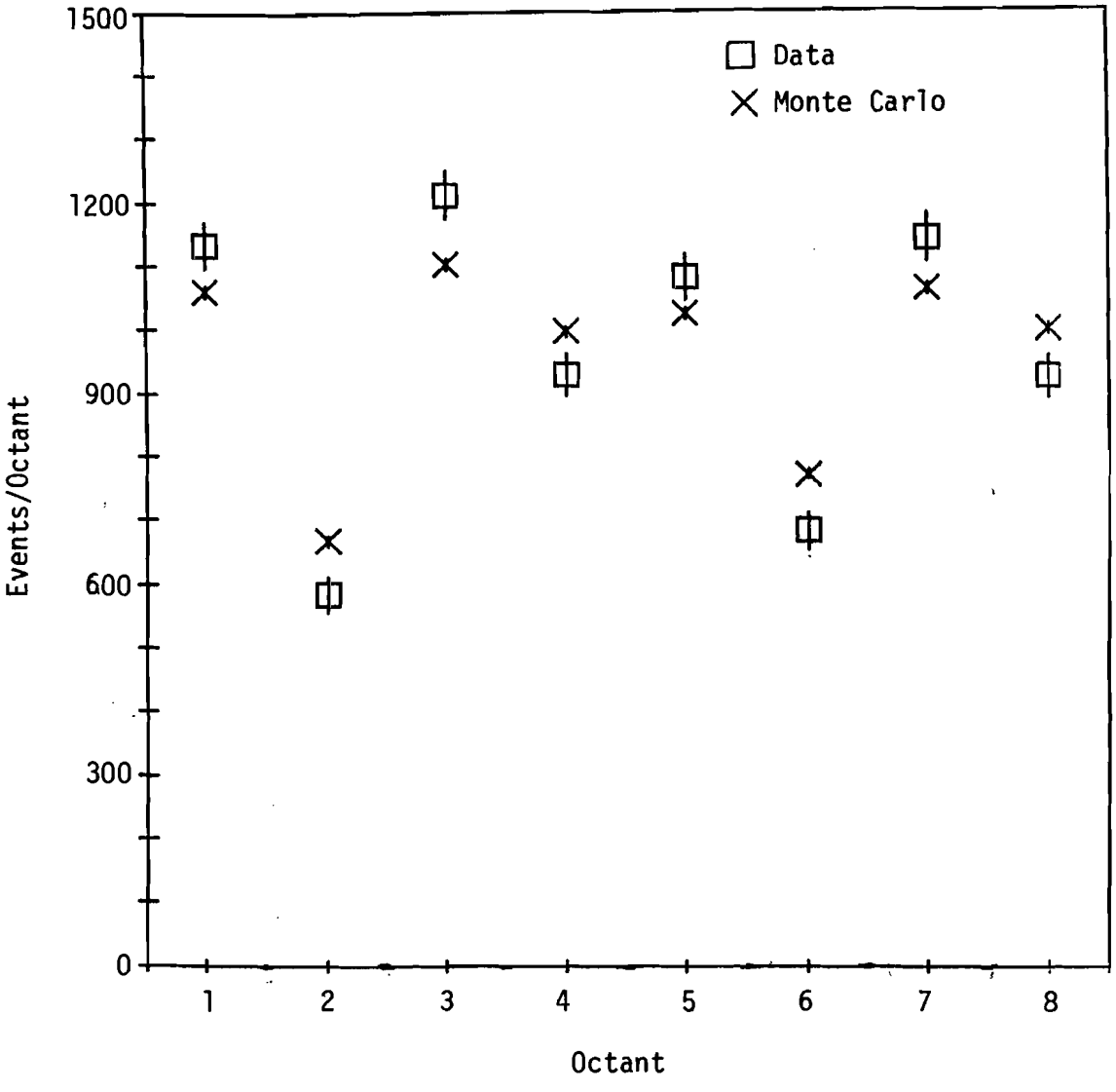
1500
1200
900
600
300
0
Events/Octant
Data
Monte Carlo
1
2
3
4
5
6
7
8
Octant

Figure 16.— The distribution of the number of drift chamber of hits per octant for positive tracks. Data and background.

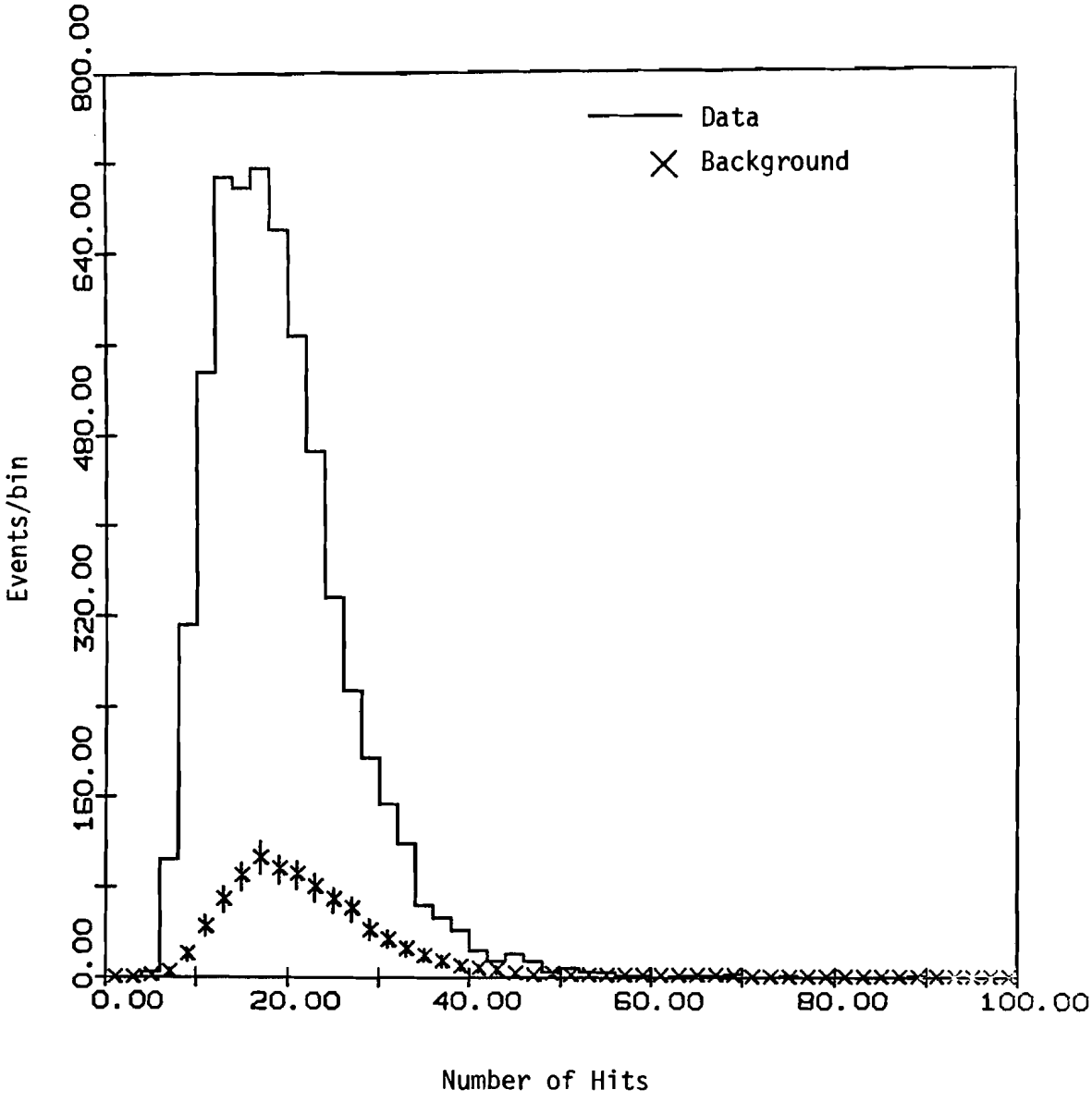
Data
Background
Events/bin
0.00
160.00
320.00
480.00
640.00
800.00
0.00
20.00
40.00
60.00
80.00
100.00
Number of Hits

Figure 17.— The distribution of the number of drift chamber of hits per octant for negative tracks. Data and background.

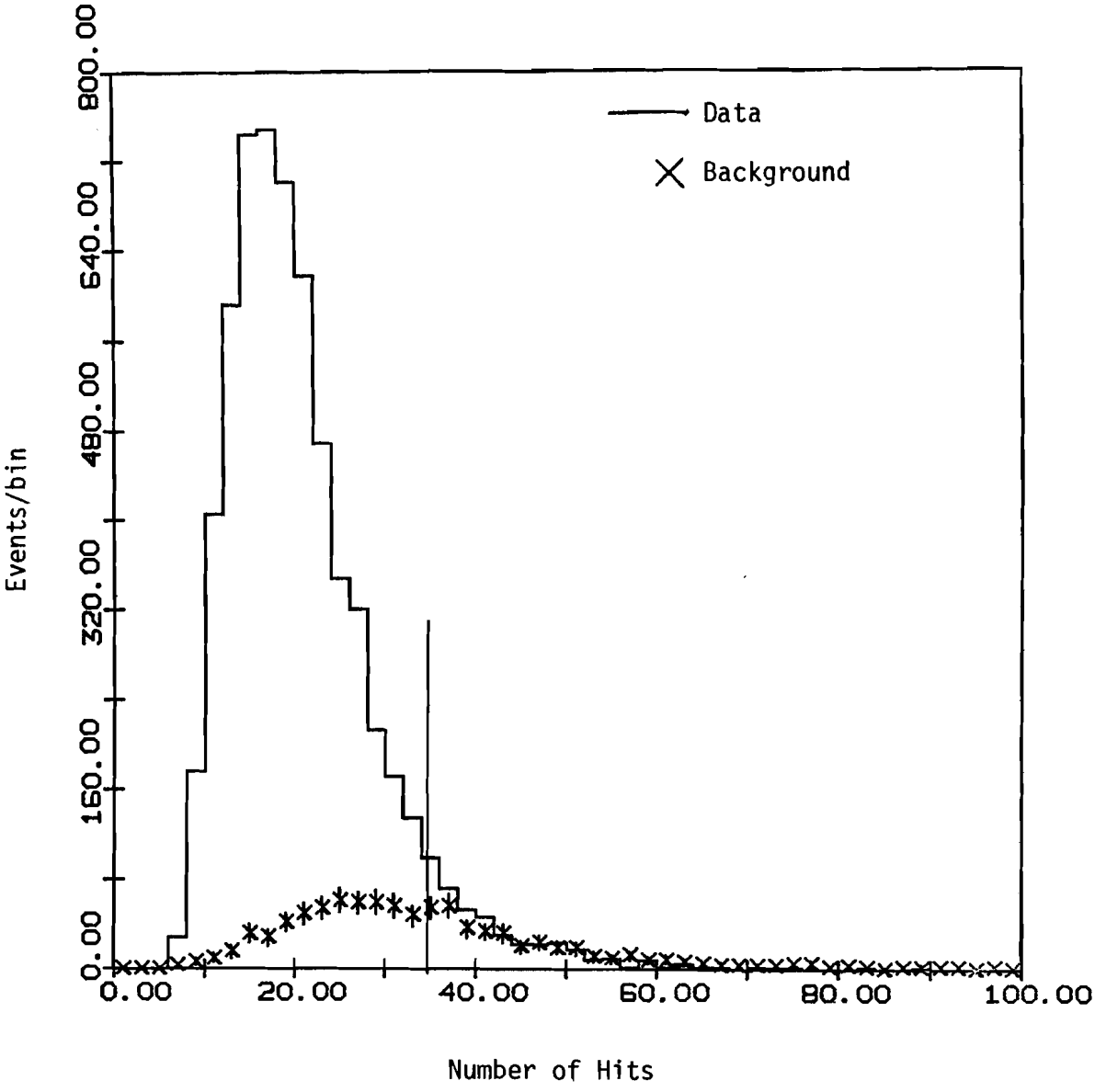
Data
Background
Events/bin
0.00
160.00
320.00
480.00
640.00
800.00
0.00
20.00
40.00
60.00
80.00
100.00
Number of Hits

Figure 18.— The distribution of $P \cdot \Delta\theta$ for positive tracks. Data and background.

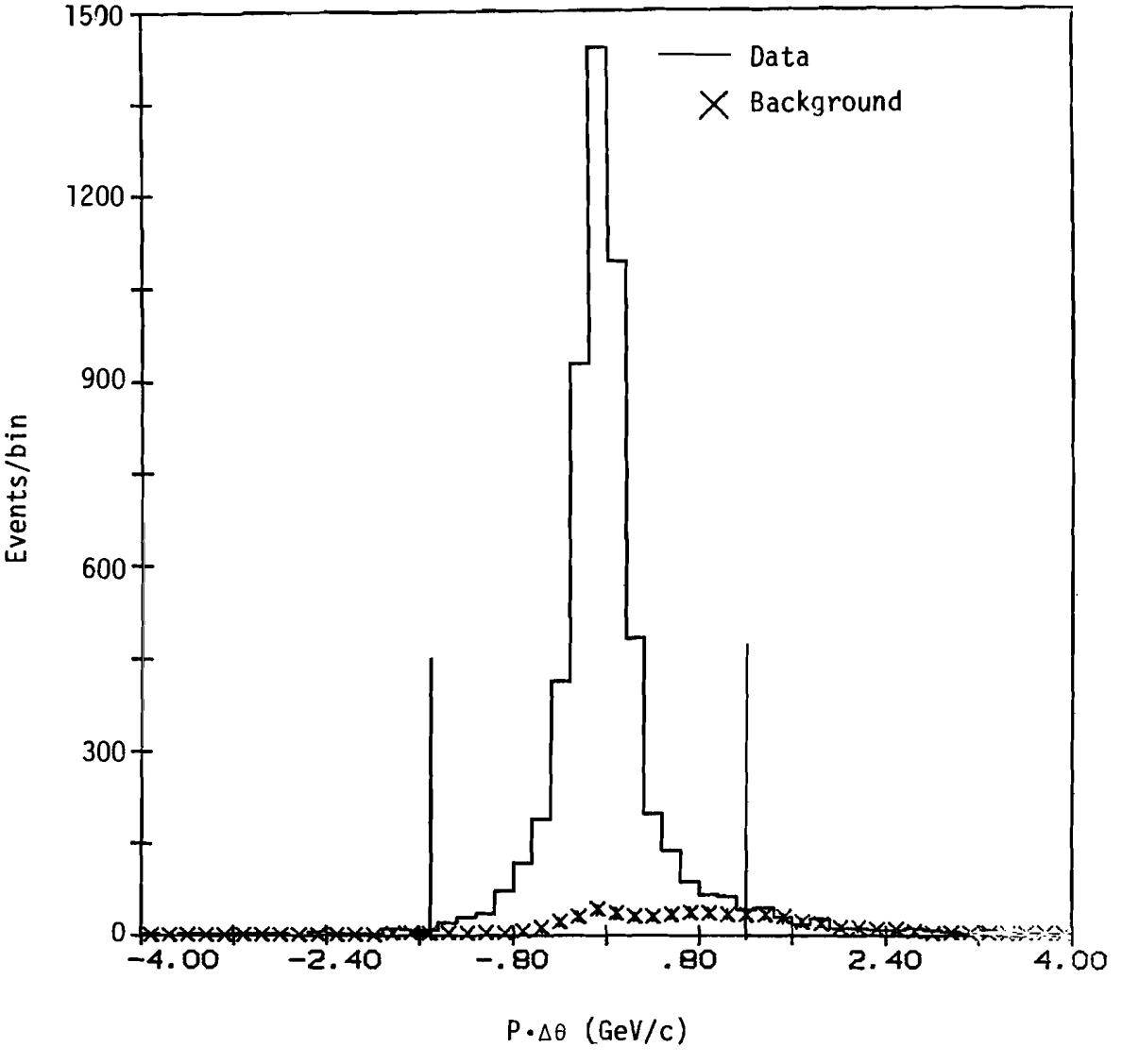
1500
1200
900
600
300
0
Events/bin
Data
Background
-4.00
-2.40
-.80
.80
2.40
4.00
P·Δθ (GeV/c)

Figure 19.— The distribution of $P \cdot \Delta\theta$ for negative tracks. Data and background.

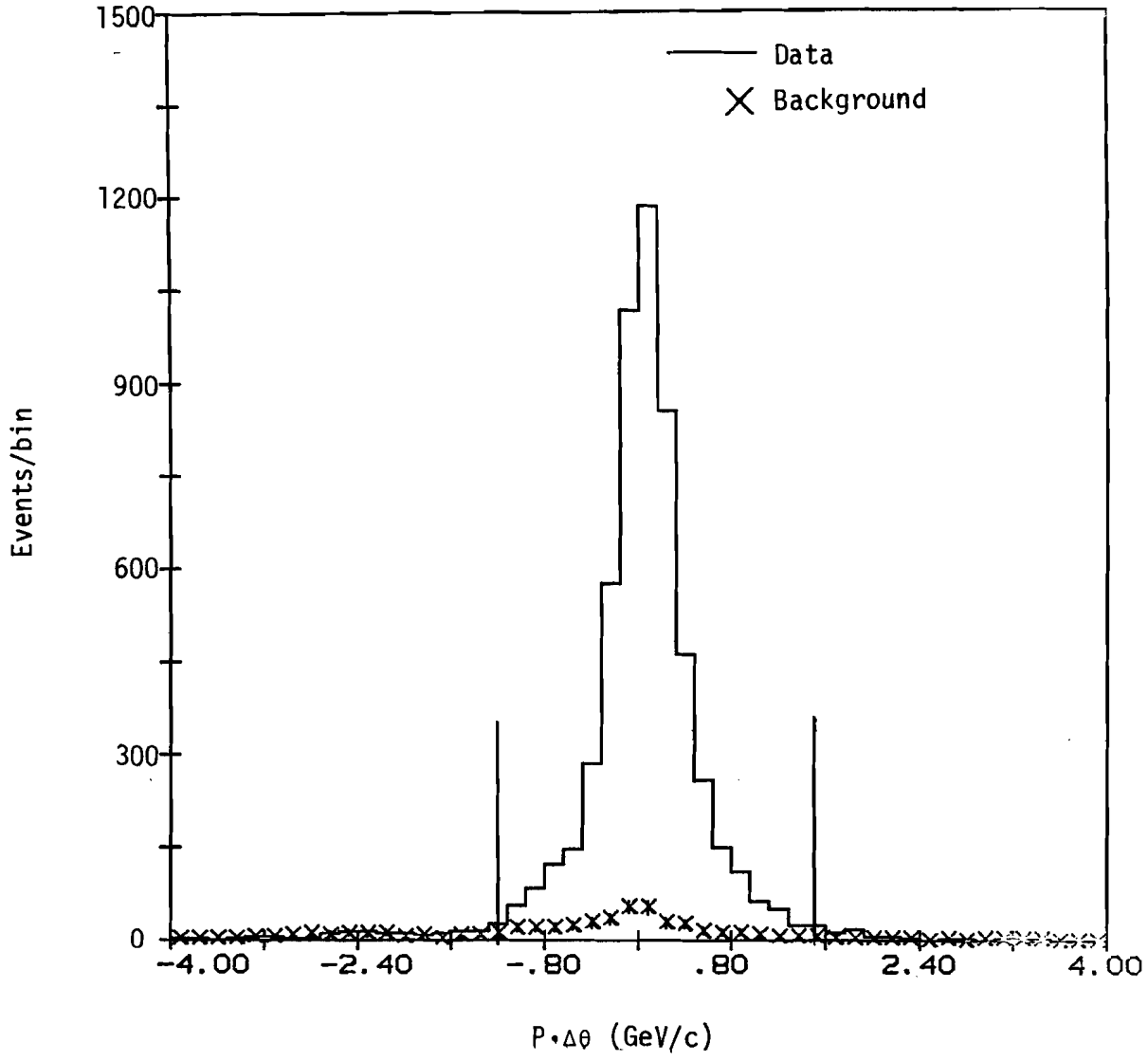
1500
1200
900
600
300
0
Events/bin
Data
Background
-4.00
-2.40
-.80
.80
2.40
4.00
P•Δθ (GeV/c)

Figure 20.— The distribution of $\Delta P/P$ for positive tracks. Data and background.

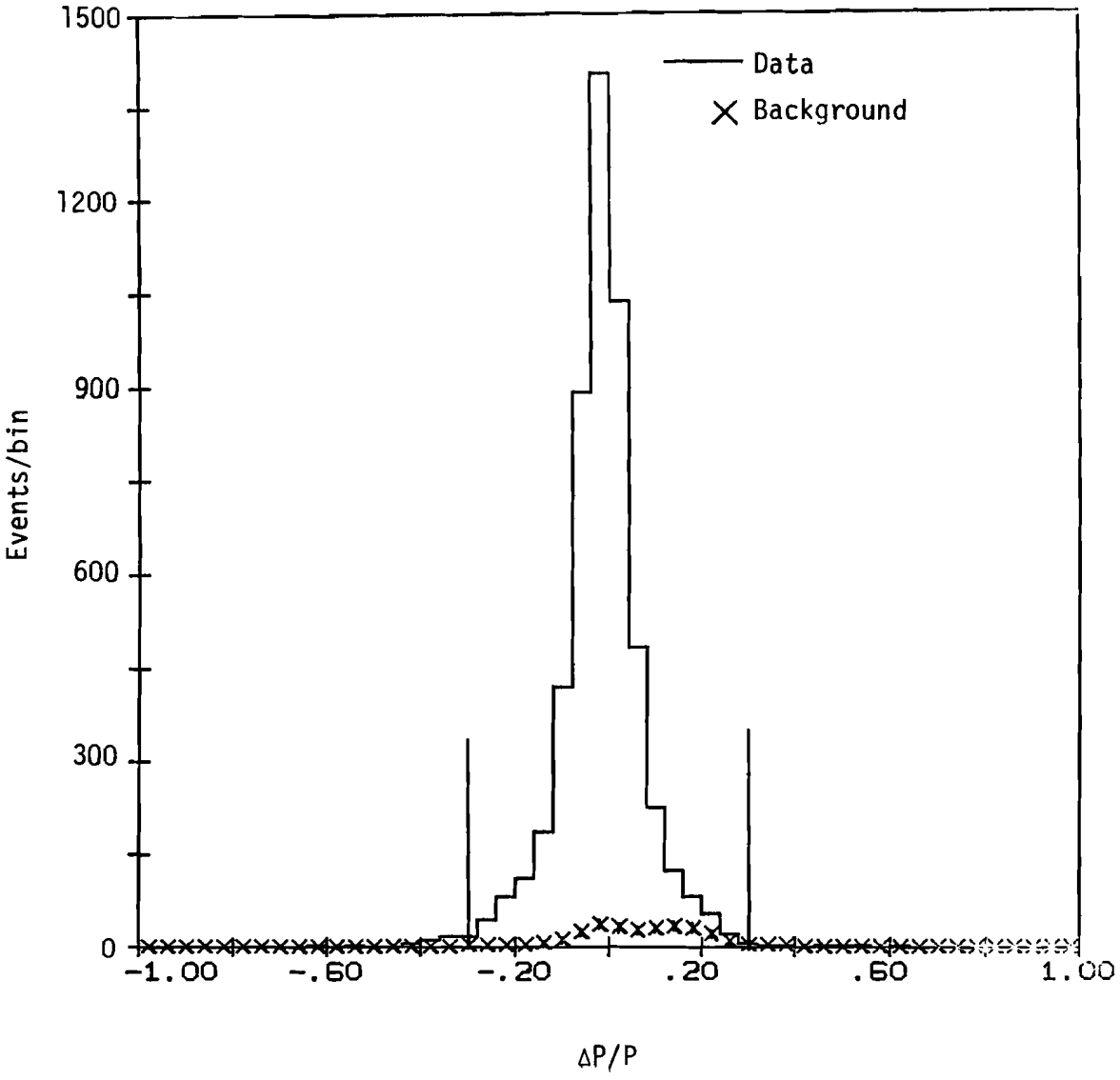
1500
1200
900
600
300
0
Events/bin
Data
Background
-1.00
-.60
-.20
.20
.60
1.00
ΔP/P

Figure 21.— The distribution of $\Delta P/P$ for negative tracks. Data and background.

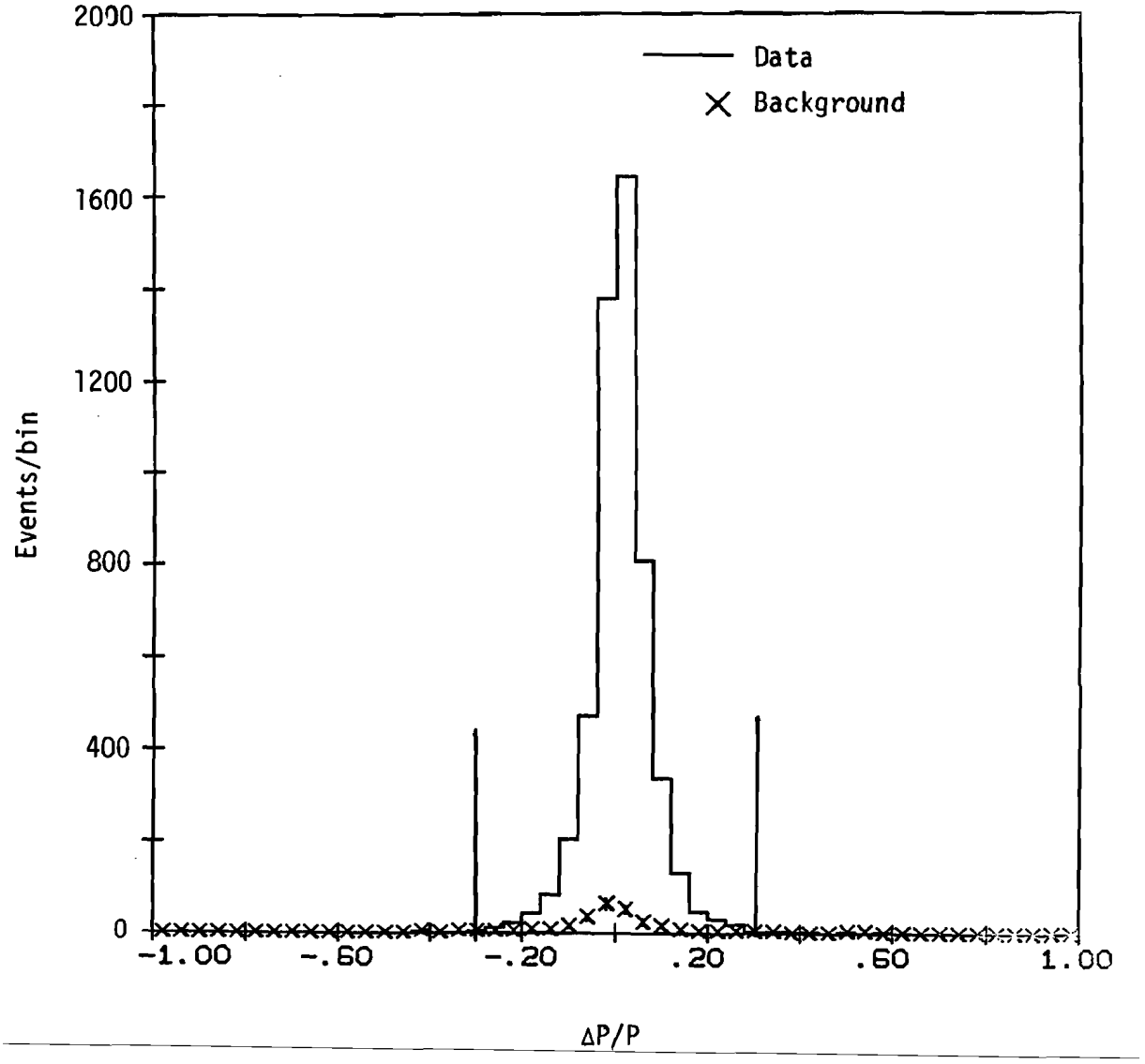
2000
1600
1200
800
400
0
Events/bin
Data
Background
-1.00
-.60
-.20
.20
.60
1.00
ΔP/P

Figure 22.— The χ^2 distribution for four gap positive tracks. Data and background.

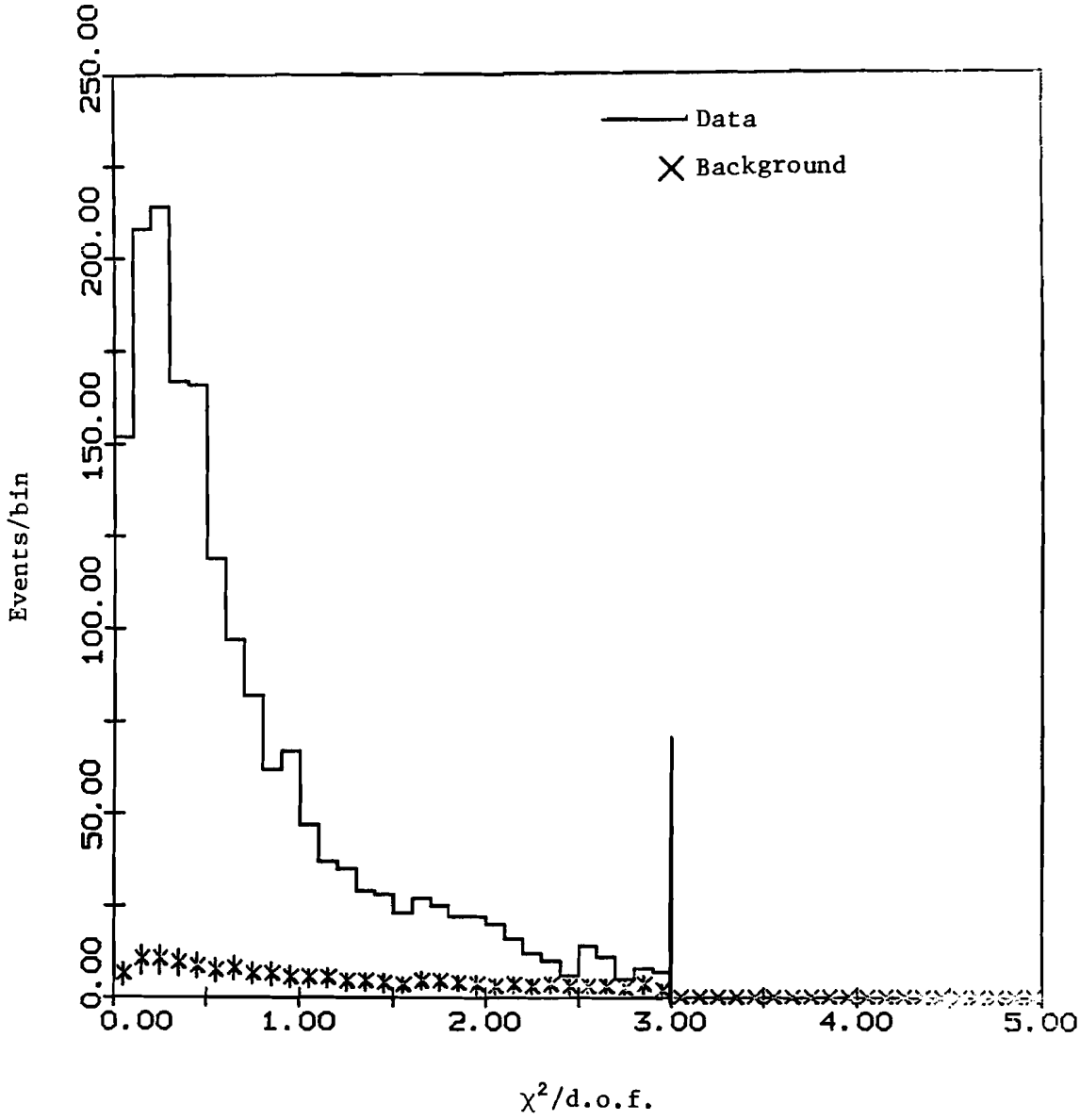
Data
Background
Events/bin
0.00
50.00
100.00
150.00
200.00
250.00
0.00
1.00
2.00
3.00
4.00
5.00
χ^2/d.o.f.

Figure 23.— The χ^2 distribution for positive tracks longer than four gaps. Data and background.

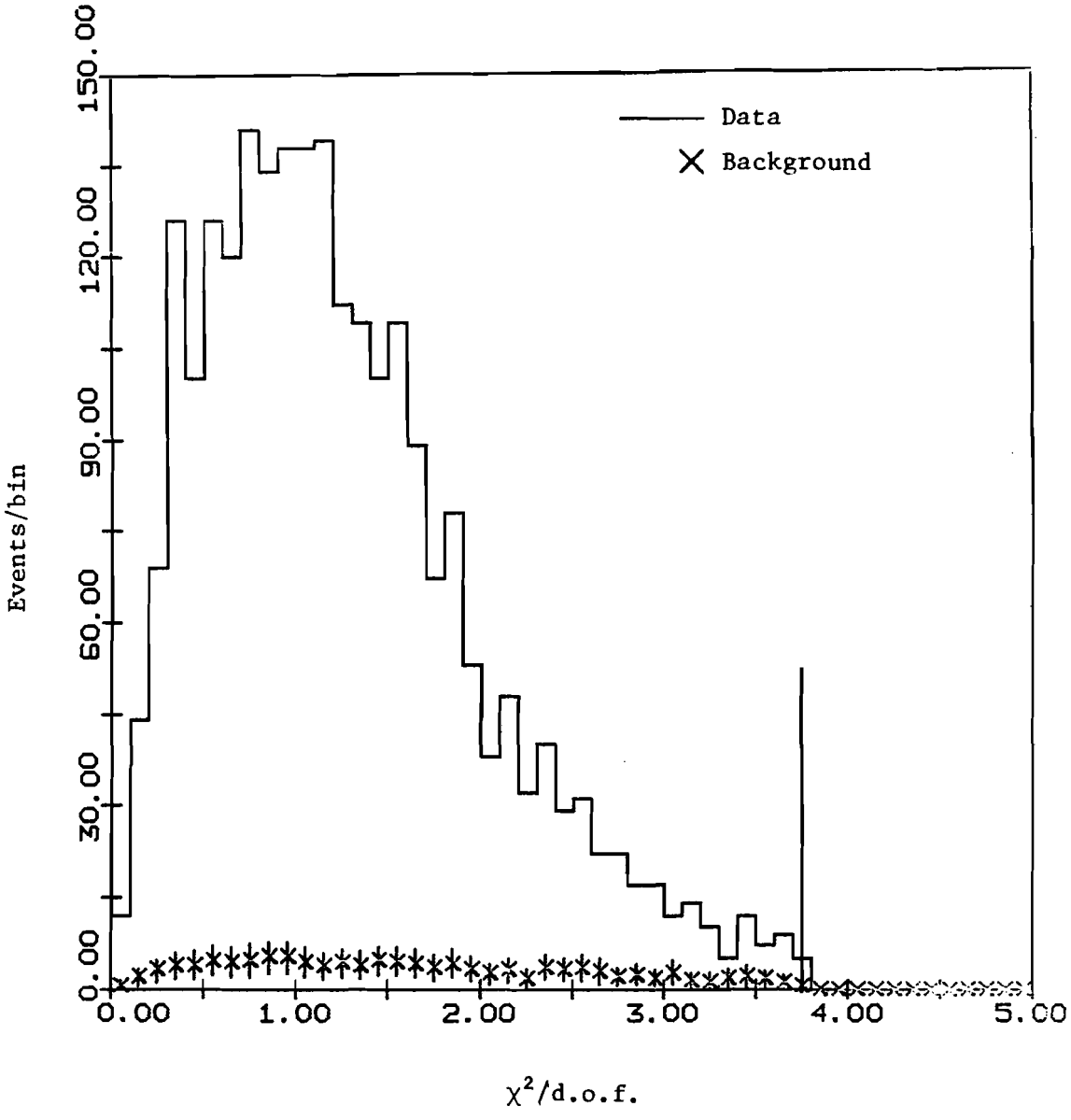
Data
Background
Events/bin
0.00
30.00
60.00
90.00
120.00
150.00
0.00
1.00
2.00
3.00
4.00
5.00
χ^2/d.o.f.

Figure 24.— The χ^2 distribution for four gap negative tracks. Data and background.

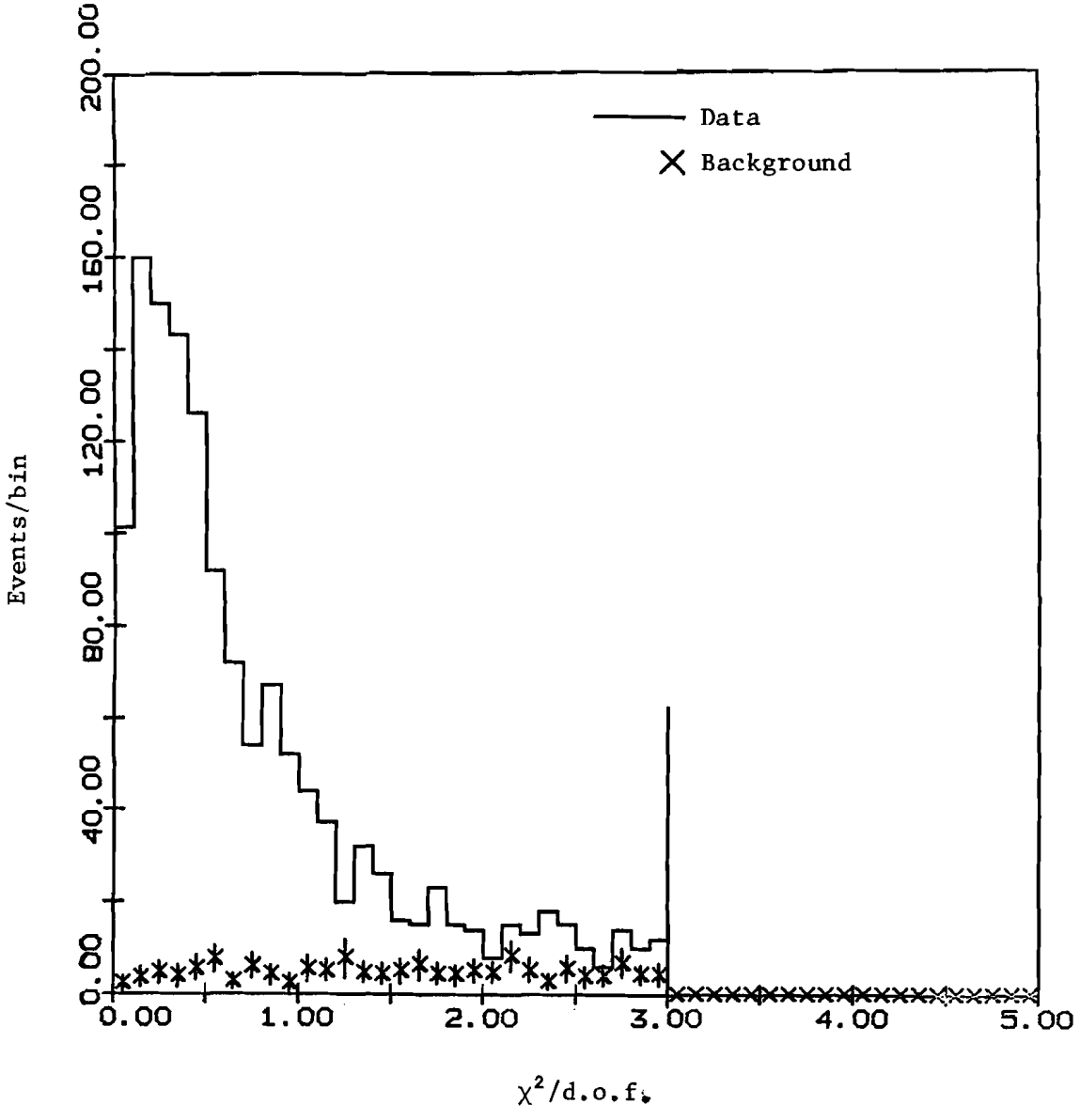
Data
Background
Events/bin
0.00
40.00
80.00
120.00
150.00
200.00
0.00
1.00
2.00
3.00
4.00
5.00
χ^2/d.o.f.

Figure 25.— The χ^2 distribution for negative tracks longer than four gaps. Data and background.

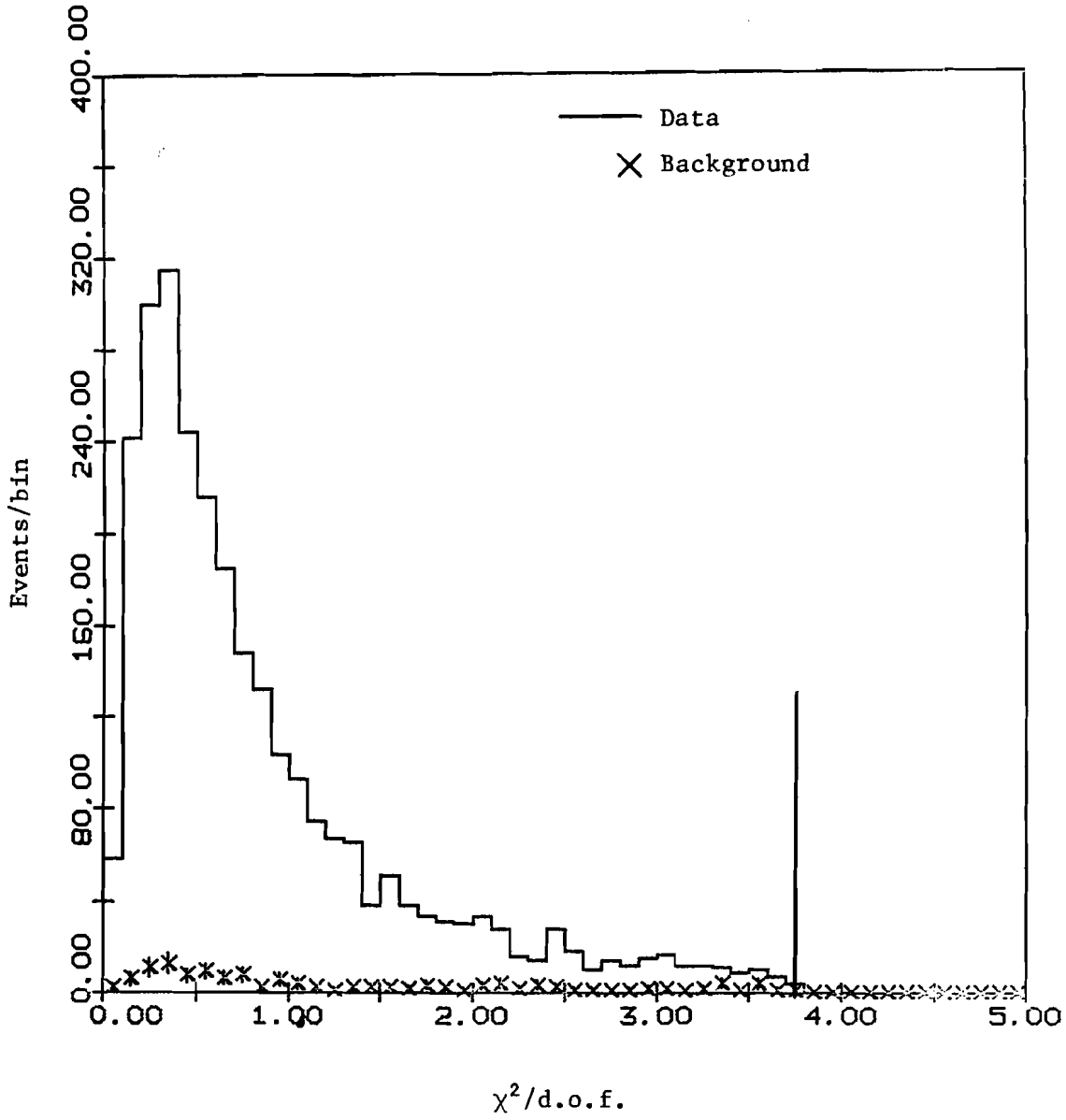
Data
Background
Events/bin
0.00
80.00
160.00
240.00
320.00
400.00
0.00
1.00
2.00
3.00
4.00
5.00
χ^2/d.o.f.

Figure 26.— A comparison of the data and background mass distributions for same sign positive events.

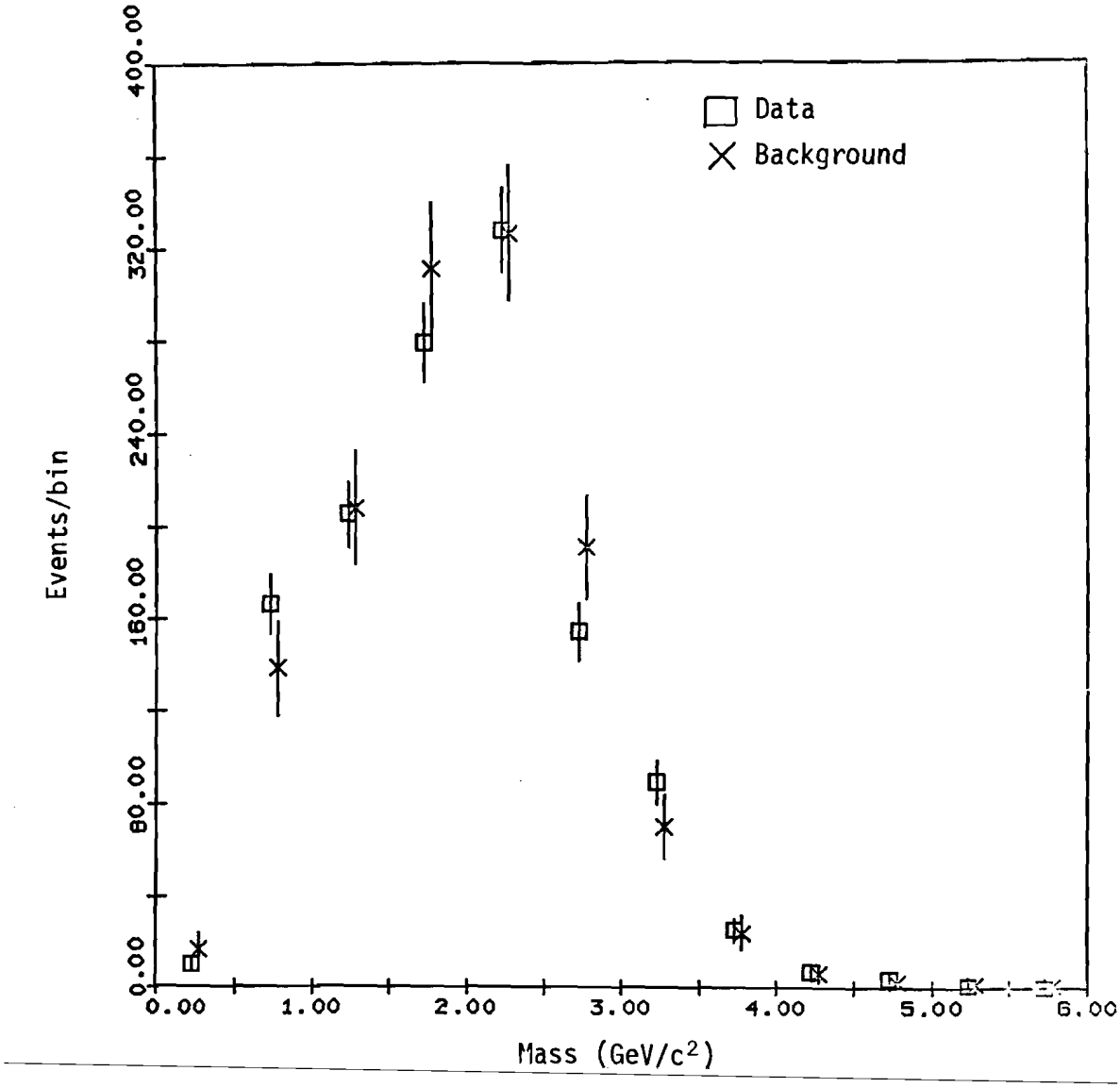
Data
Background
Events/bin
0.00
80.00
160.00
240.00
320.00
400.00
0.00
1.00
2.00
3.00
4.00
5.00
6.00
Mass (GeV/c²)

Figure 27.— A comparison of the data and background p_T distributions for same sign positive events.

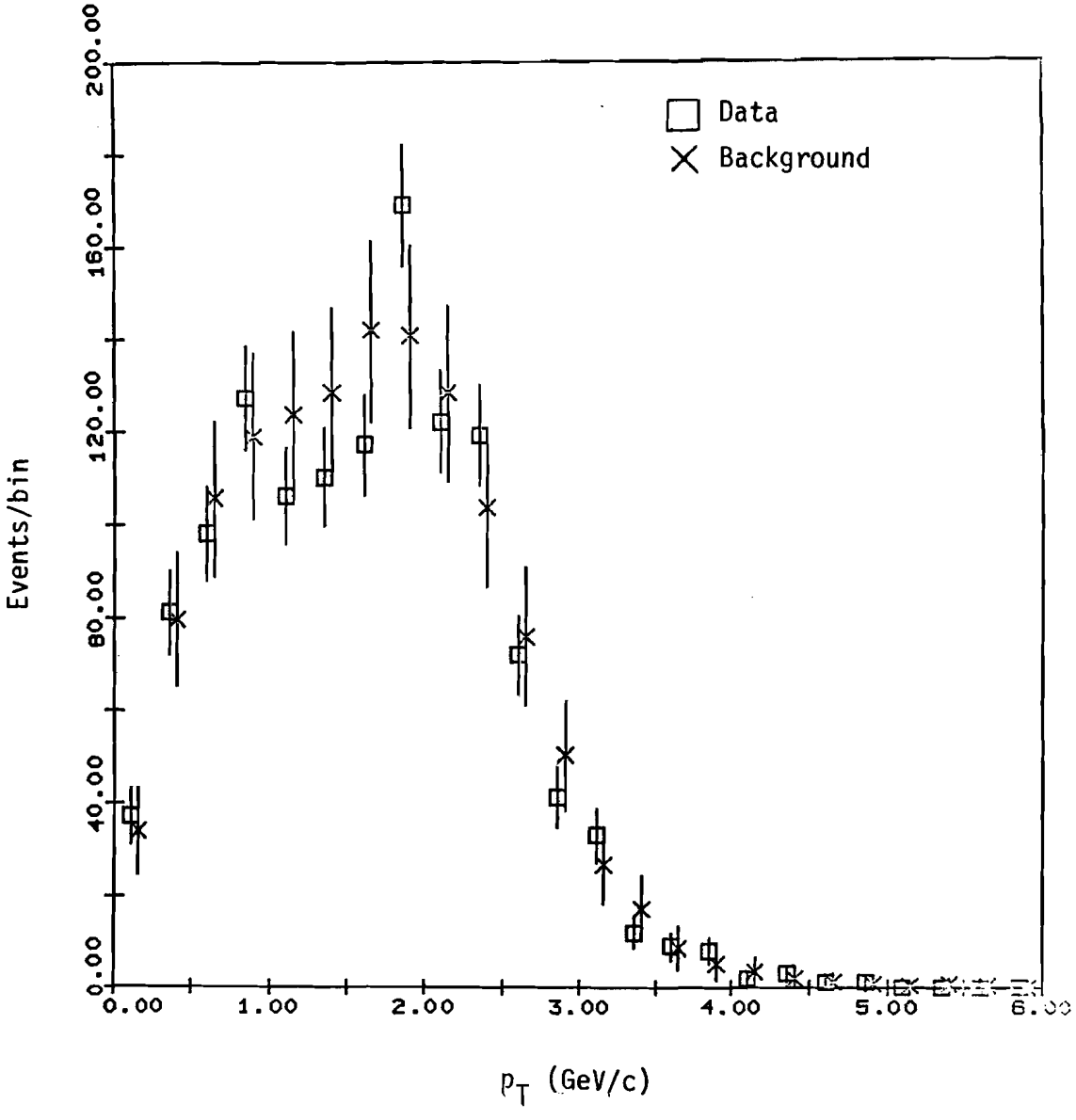
Data
Background
Events/bin
0.00
40.00
80.00
120.00
160.00
200.00
0.00
1.00
2.00
3.00
4.00
5.00
p_T (GeV/c)

Figure 28.— A comparison of the data and background x_F distributions for same sign positive events.

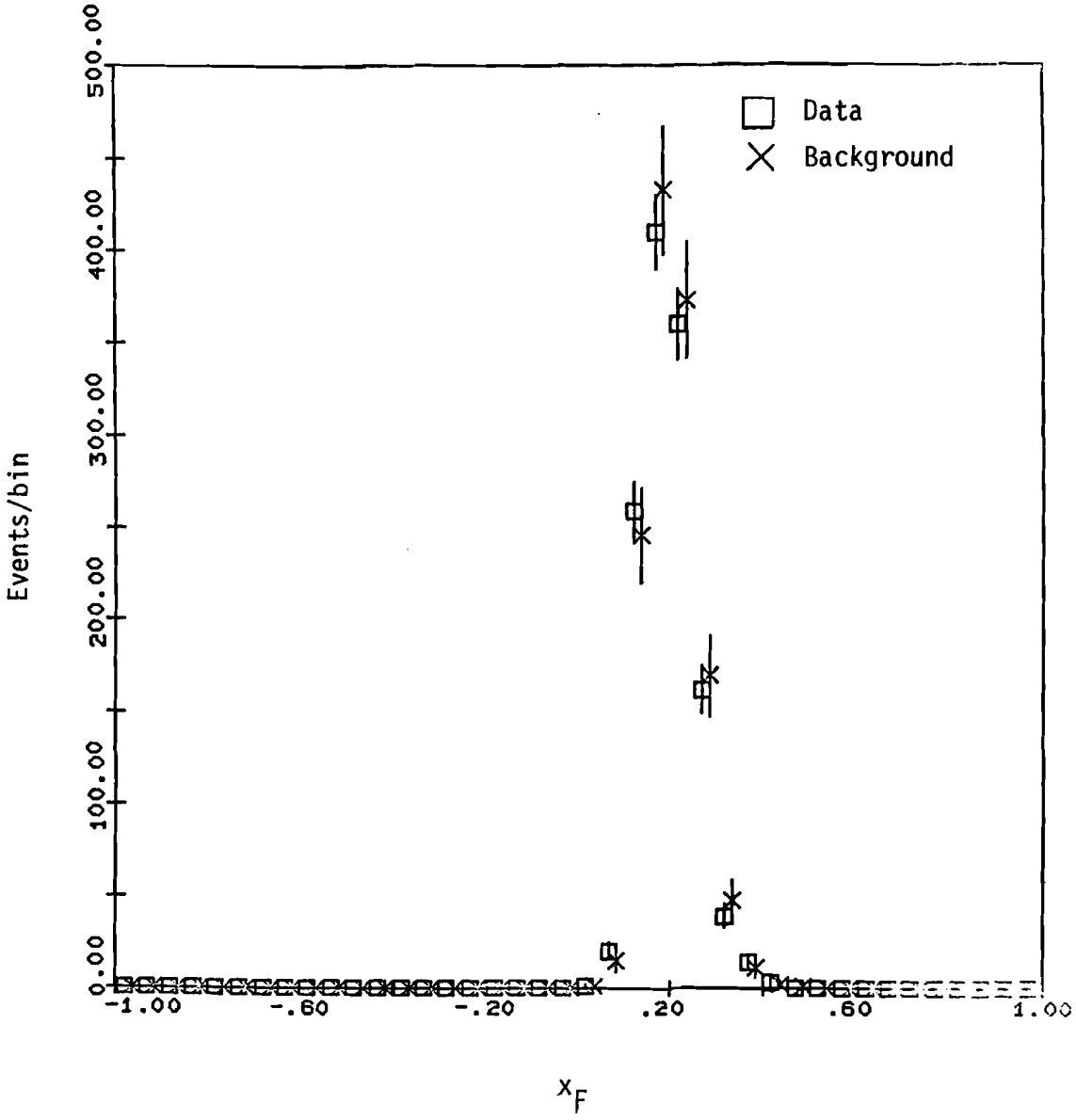
Data
Background
Events/bin
0.00
100.00
200.00
300.00
400.00
500.00
-1.00
-.60
-.20
.20
.60
1.00
x_F

Figure 29.— A comparison of the data and background $\cos\theta^*$ distributions for same sign positive events.

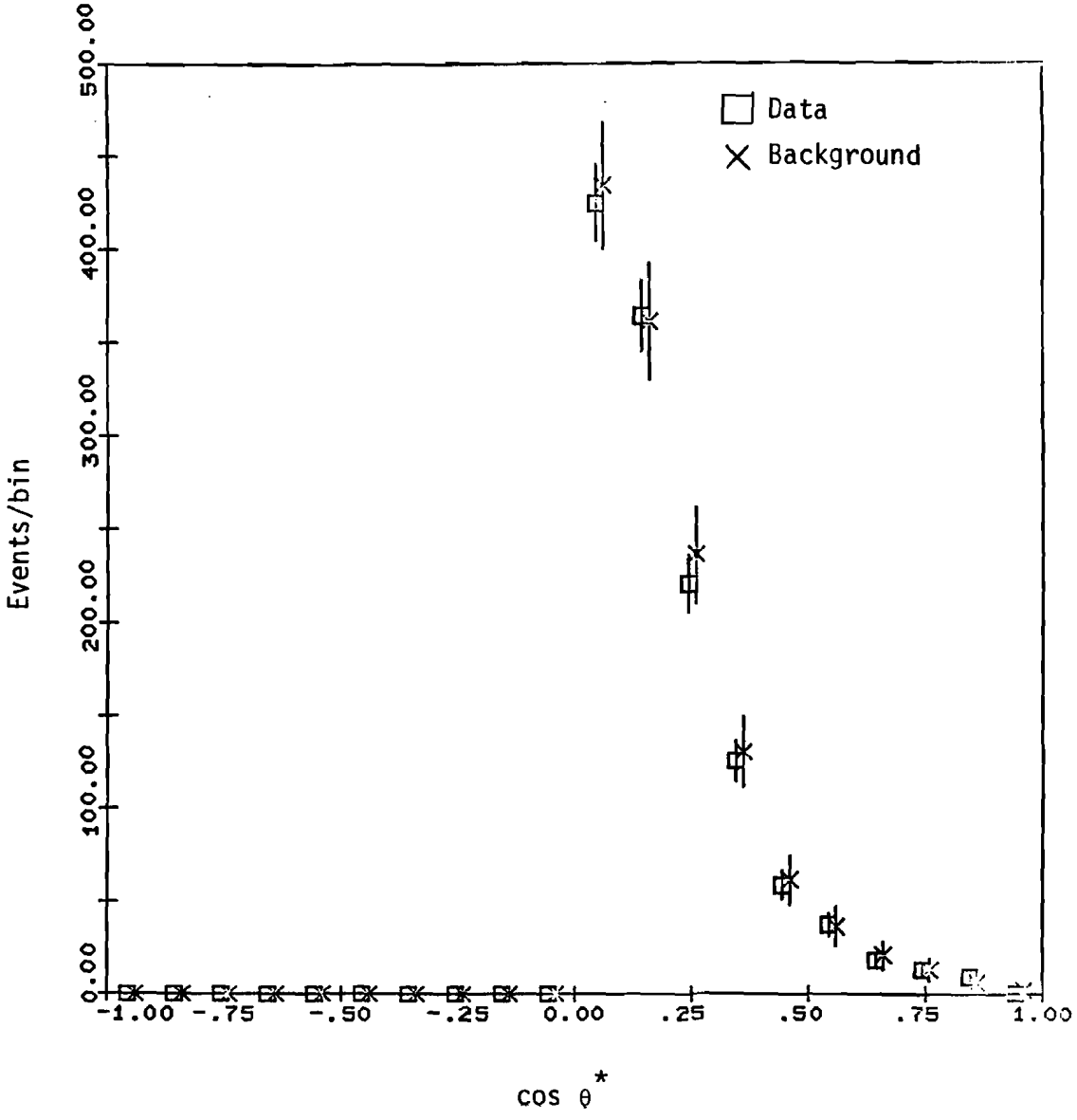
Data
Background
Events/bin
0.00
100.00
200.00
300.00
400.00
500.00
-1.00
-.75
-.50
-.25
0.00
.25
.50
.75
1.00
cos θ*

Figure 30.— A comparison of the data and Monte Carlo distributions of the gap 1 octant x coordinate for positive tracks.

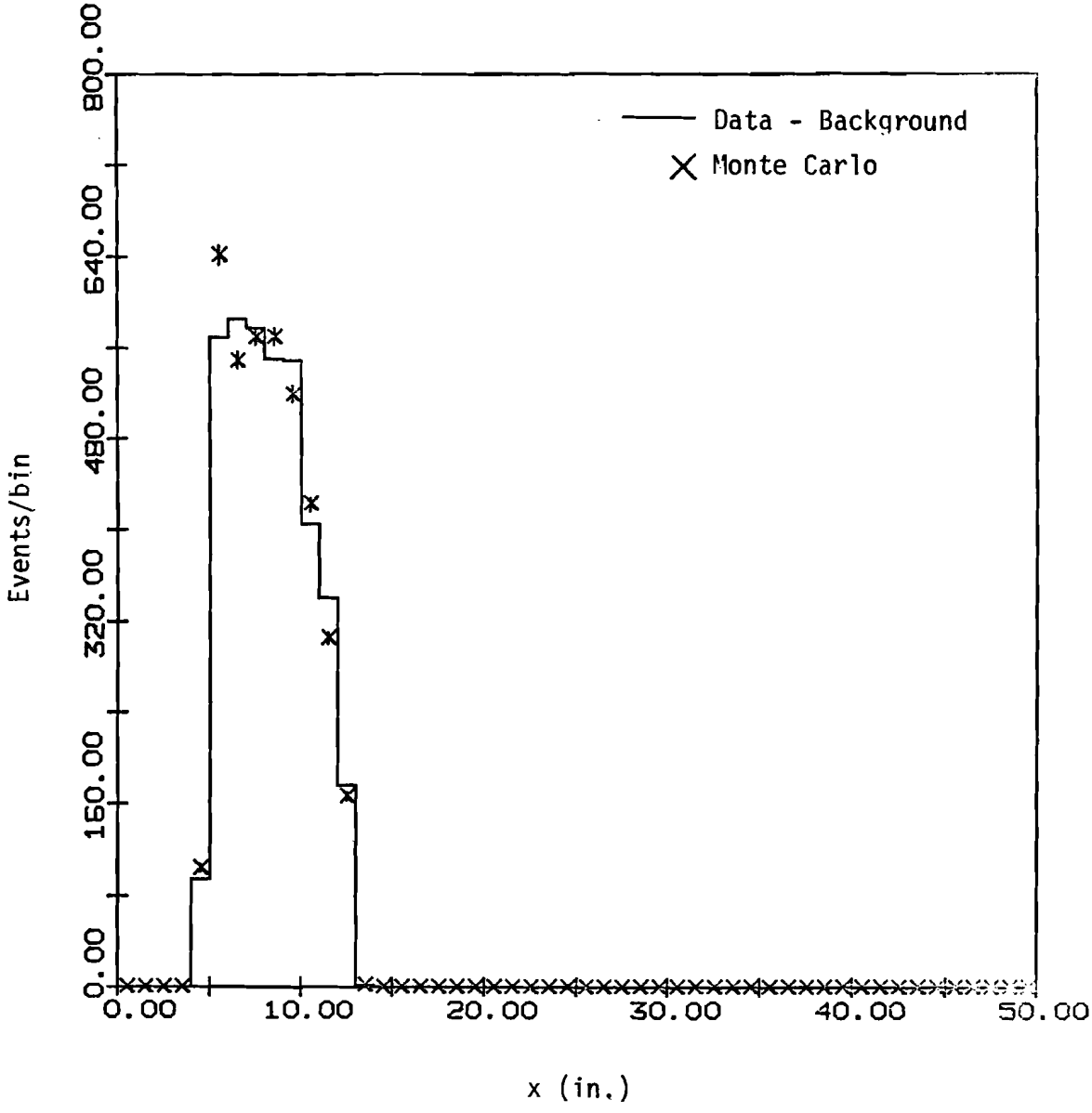
Data - Background
Monte Carlo
Events/bin
0.00
160.00
320.00
480.00
640.00
800.00
0.00
10.00
20.00
30.00
40.00
50.00
x (in.)

Figure 31.— A comparison of the data and Monte Carlo distributions of the gap 2 octant x coordinate for positive tracks.

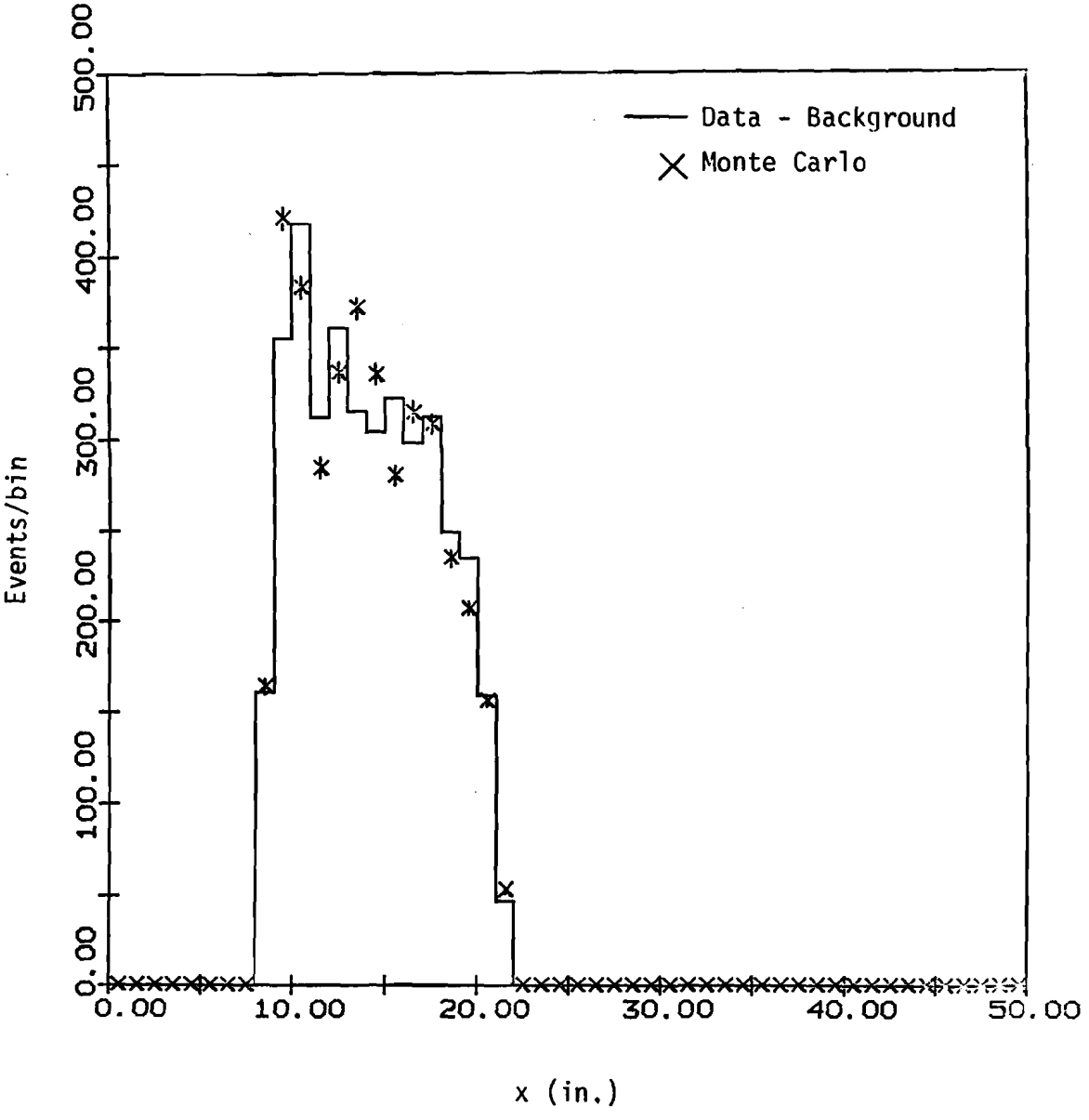
Data - Background
Monte Carlo
Events/bin
0.00
100.00
200.00
300.00
400.00
500.00
0.00
10.00
20.00
30.00
40.00
50.00
x (in.)

Figure 32.— A comparison of the data and Monte Carlo distributions of the gap 3 octant x coordinate for positive tracks.

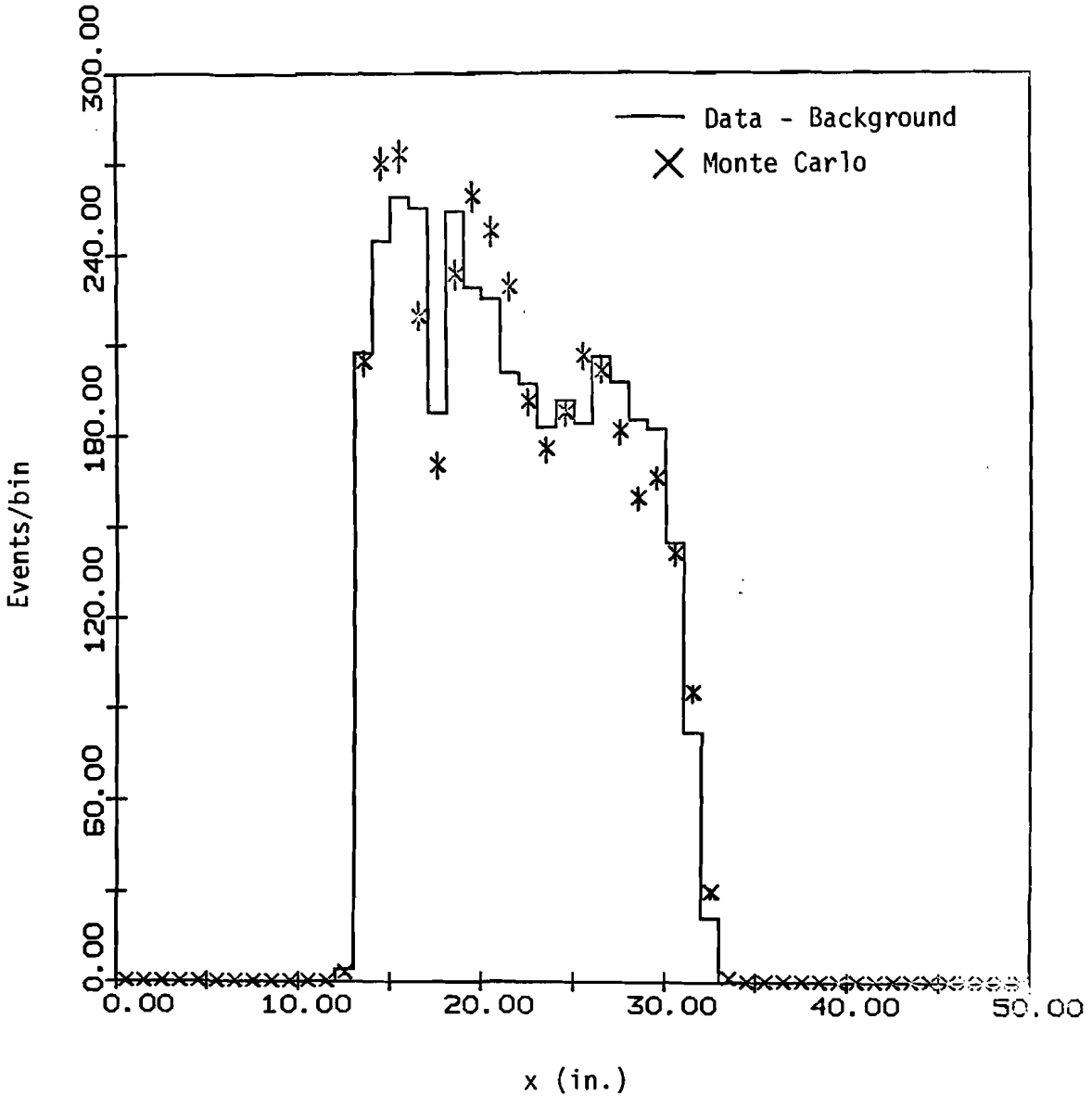
Data - Background
Monte Carlo
Events/bin
0.00
60.00
120.00
180.00
240.00
300.00
0.00
10.00
20.00
30.00
40.00
50.00
x (in.)

Figure 33.— A comparison of the data and Monte Carlo distributions of the gap 4 octant x coordinate for positive tracks.

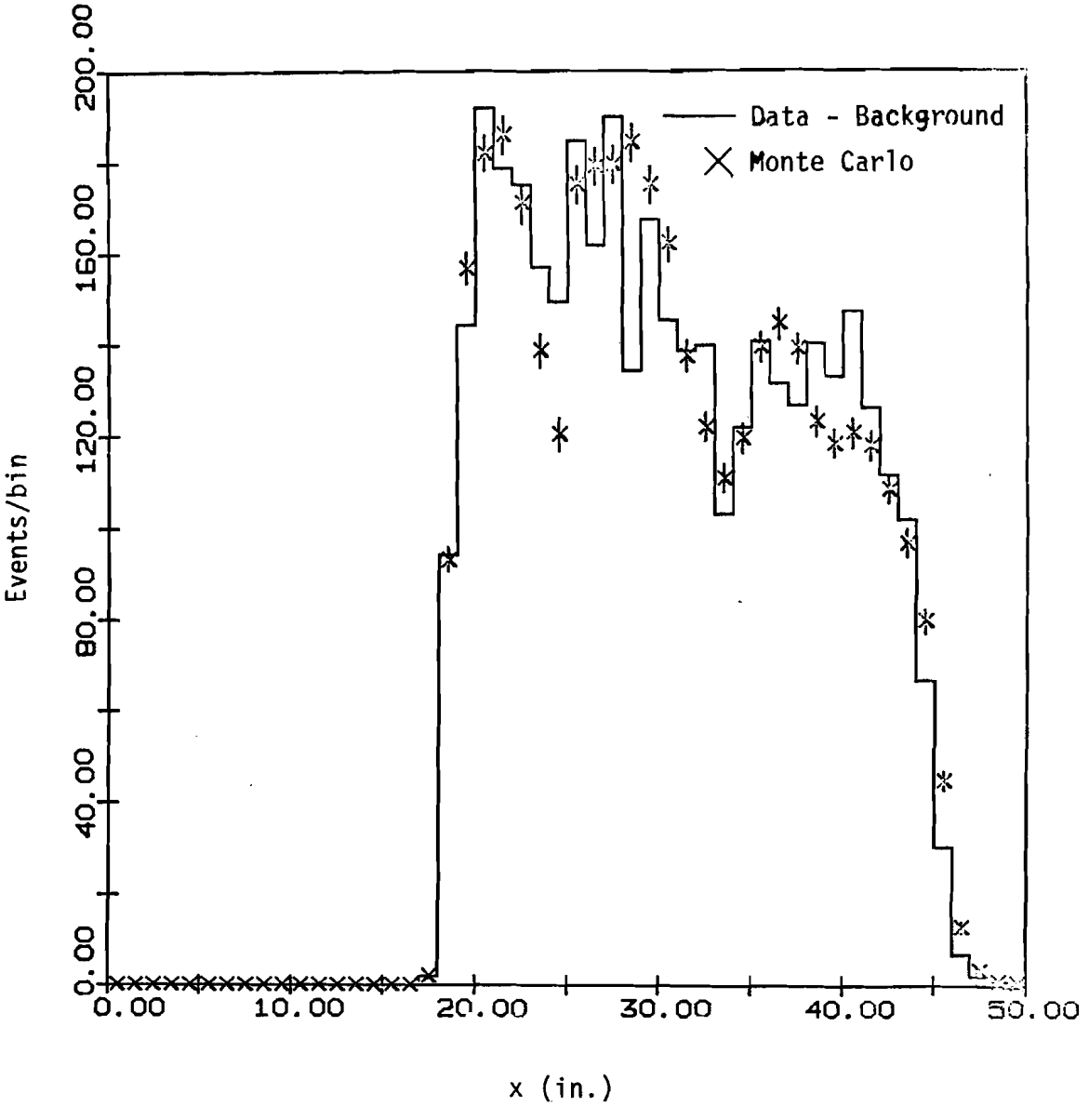
Data - Background
Monte Carlo
Events/bin
0.00
40.00
80.00
120.00
160.00
200.00
0.00
10.00
20.00
30.00
40.00
50.00
x (in.)

Figure 34.— A comparison of the data and Monte Carlo distributions of the gap 1 octant x coordinate for negative tracks.

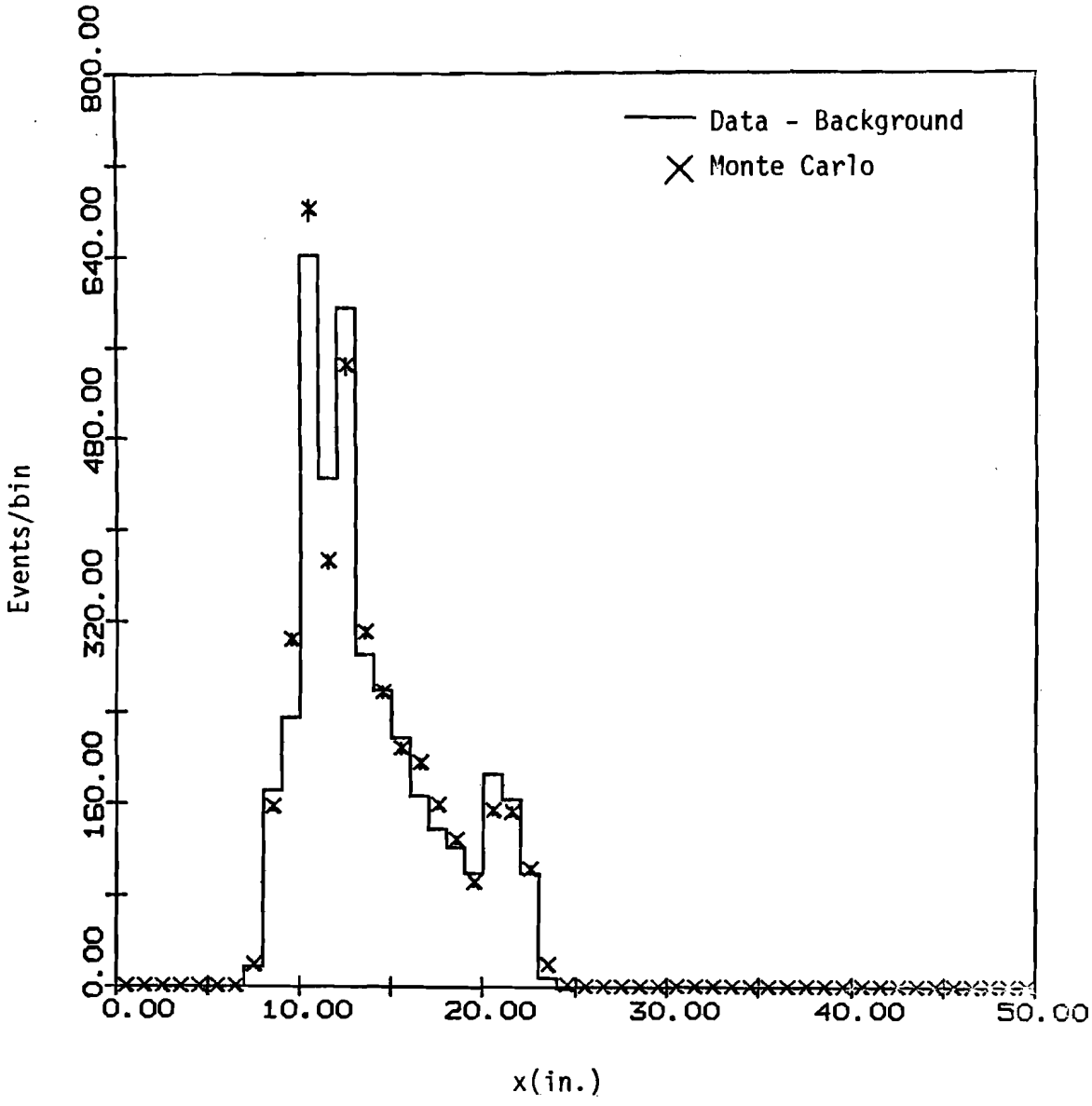
Data - Background
Monte Carlo
Events/bin
0.00
160.00
320.00
480.00
640.00
800.00
0.00
10.00
20.00
30.00
40.00
50.00
x(in.)

Figure 35.— A comparison of the data and Monte Carlo distributions of the gap 2 octant x coordinate for negative tracks.

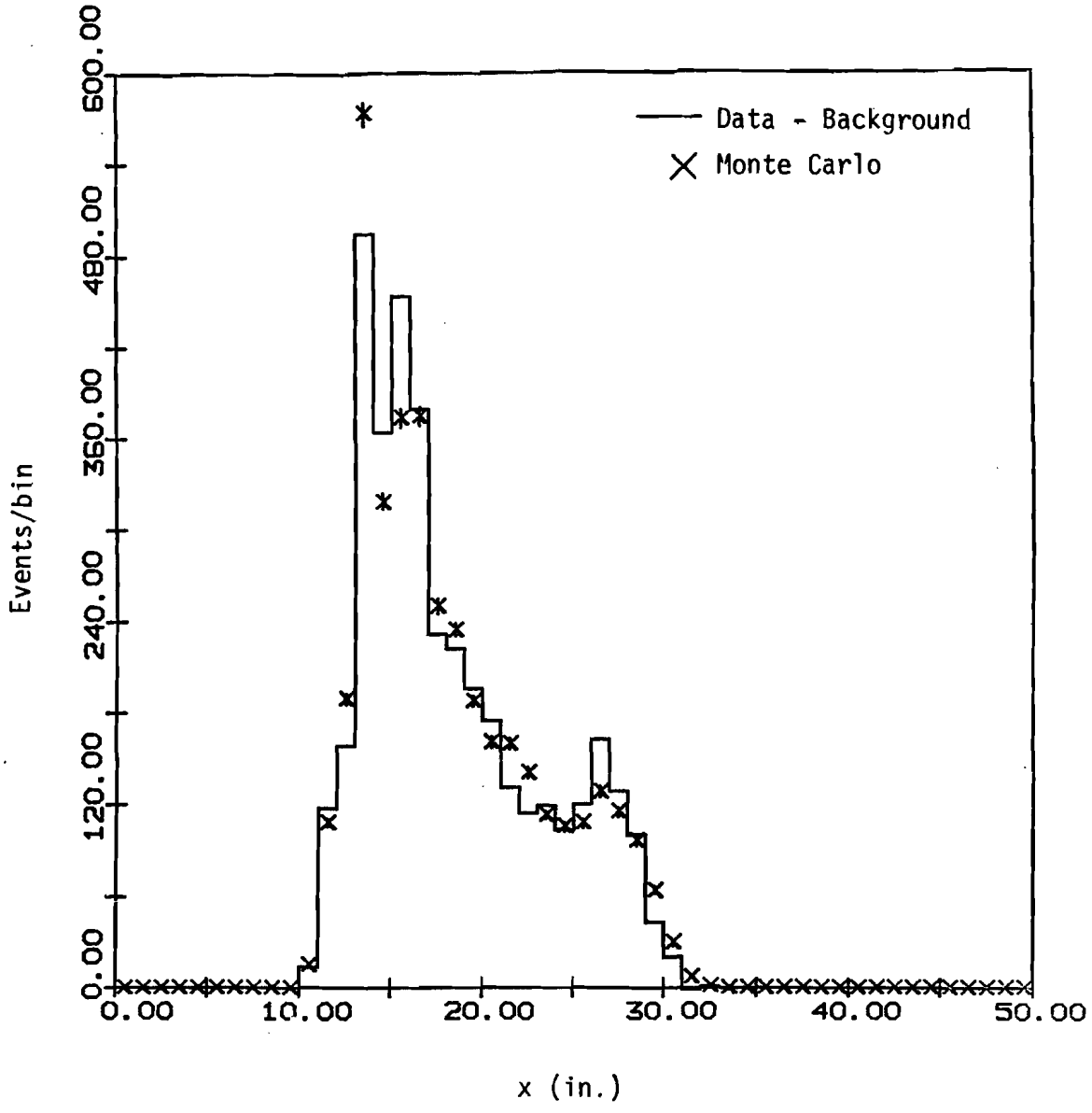
Data - Background
Monte Carlo
Events/bin
600.00
480.00
360.00
240.00
120.00
0.00
0.00
10.00
20.00
30.00
40.00
50.00
x (in.)

Figure 36.— A comparison of the data and Monte Carlo distributions of the gap 3 octant x coordinate for negative tracks.

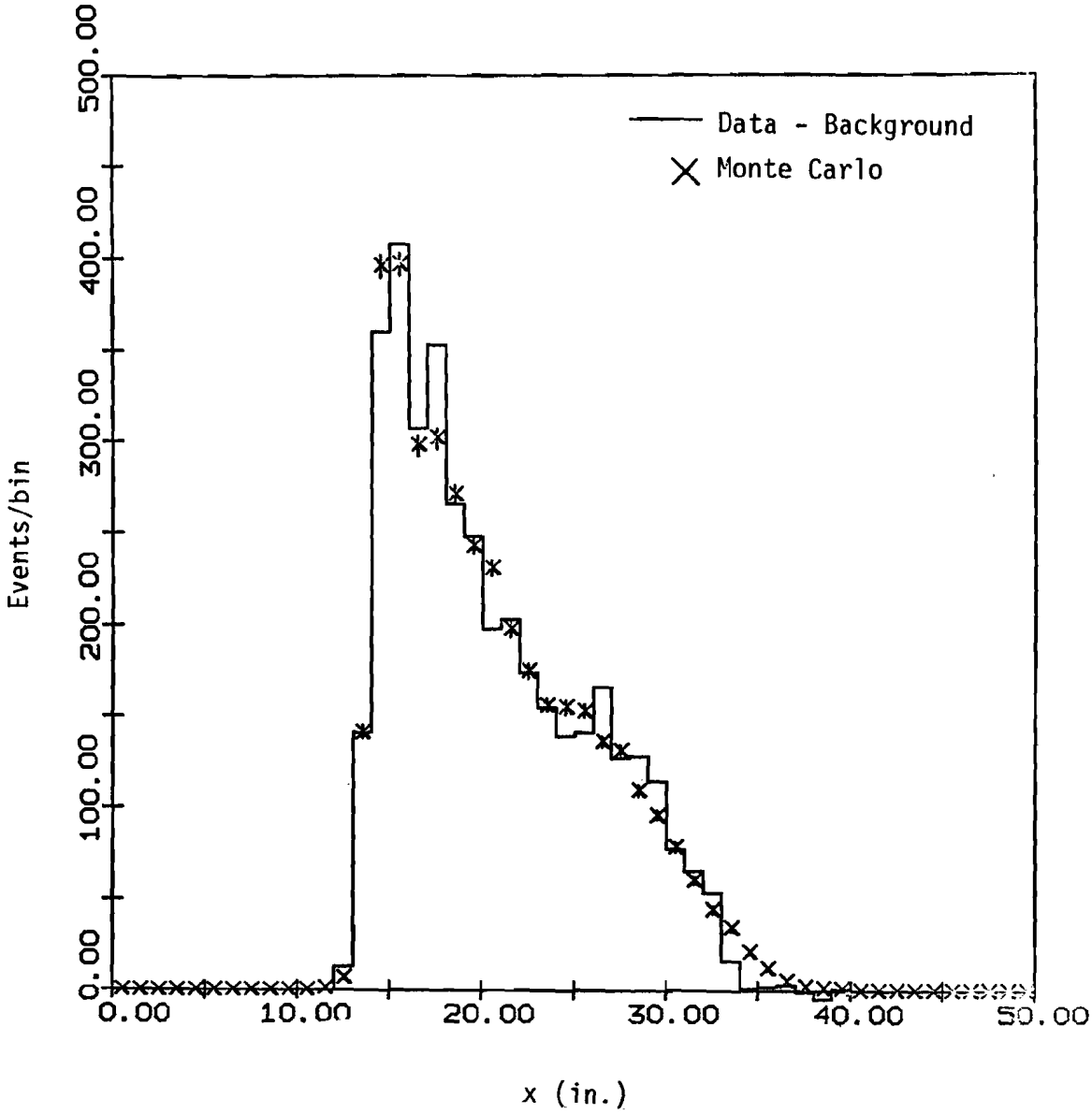
Data - Background
Monte Carlo
Events/bin
0.00
100.00
200.00
300.00
400.00
500.00
0.00
10.00
20.00
30.00
40.00
50.00
x (in.)

Figure 37.— A comparison of the data and Monte Carlo distributions of the gap 4 octant x coordinate for negative tracks.

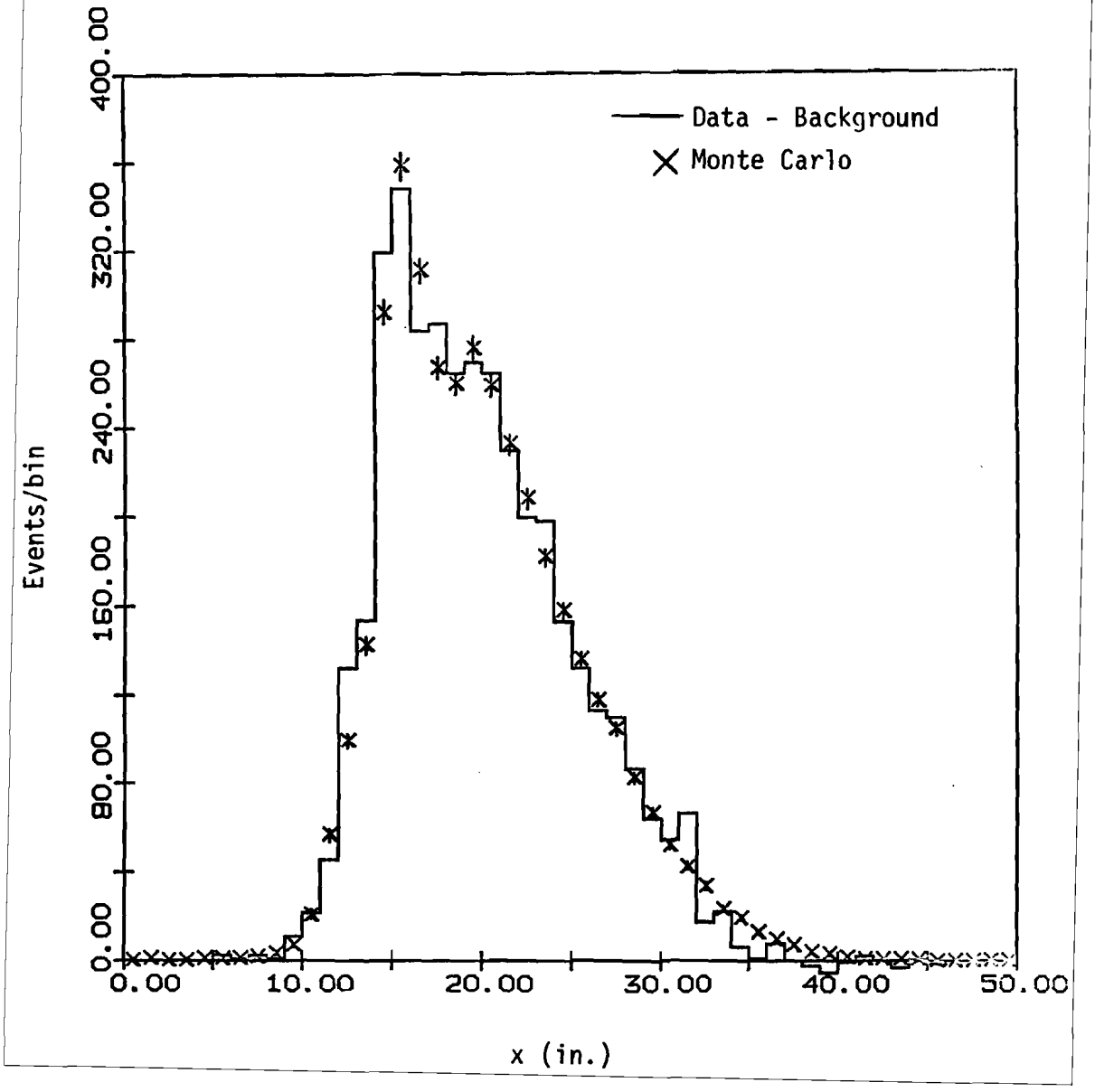
Data - Background
Monte Carlo
Events/bin
0.00
80.00
160.00
240.00
320.00
400.00
0.00
10.00
20.00
30.00
40.00
50.00
x (in.)

Figure 38.— A comparison of the data and Monte Carlo constrained χ^2 distributions for positive tracks.

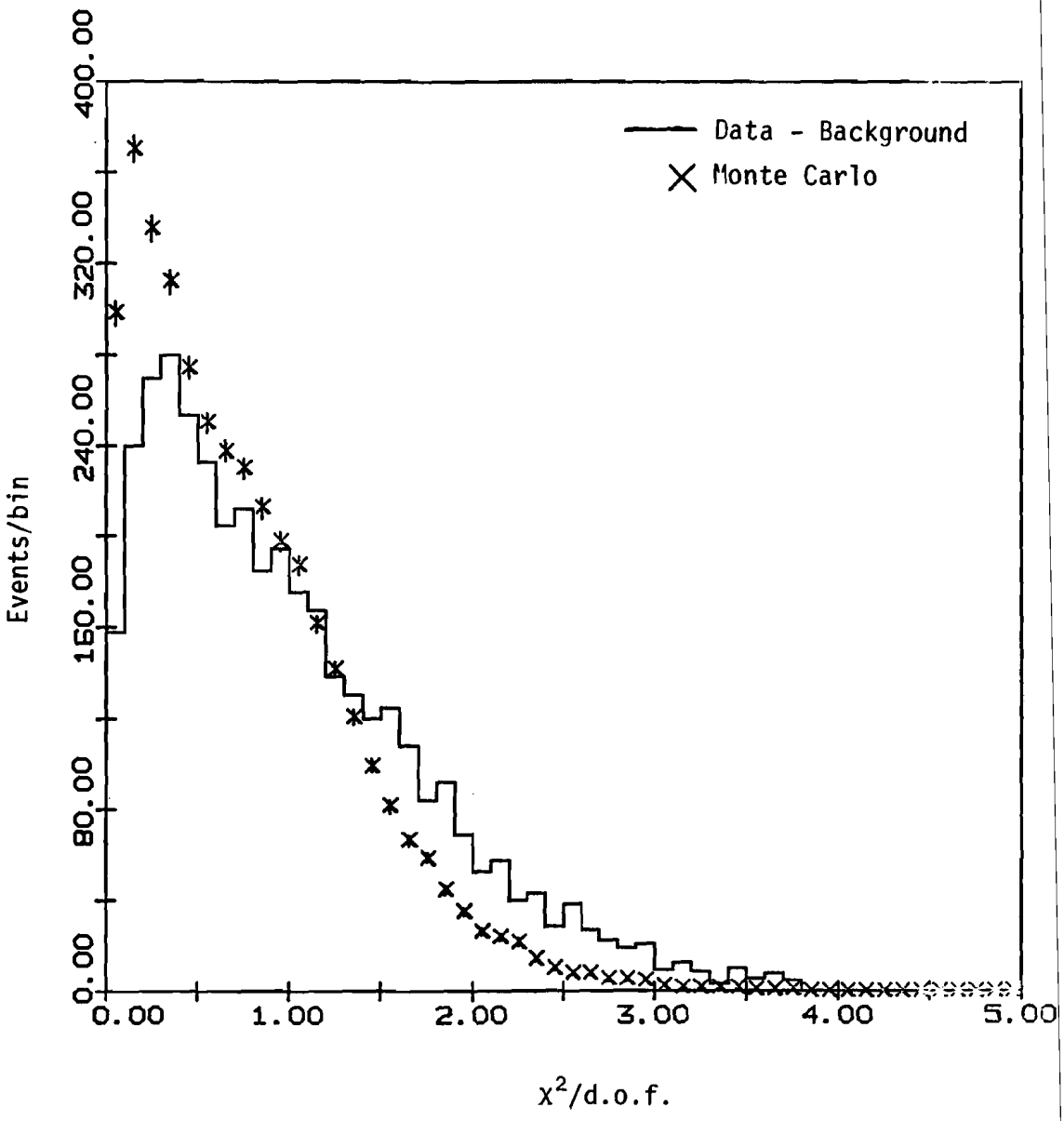
Data - Background
Monte Carlo
Events/bin
0.00
80.00
160.00
240.00
320.00
400.00
0.00
1.00
2.00
3.00
4.00
5.00
χ^2/d.o.f.

Figure 39.— A comparison of the data and Monte Carlo constrained χ^2 distributions for negative tracks.

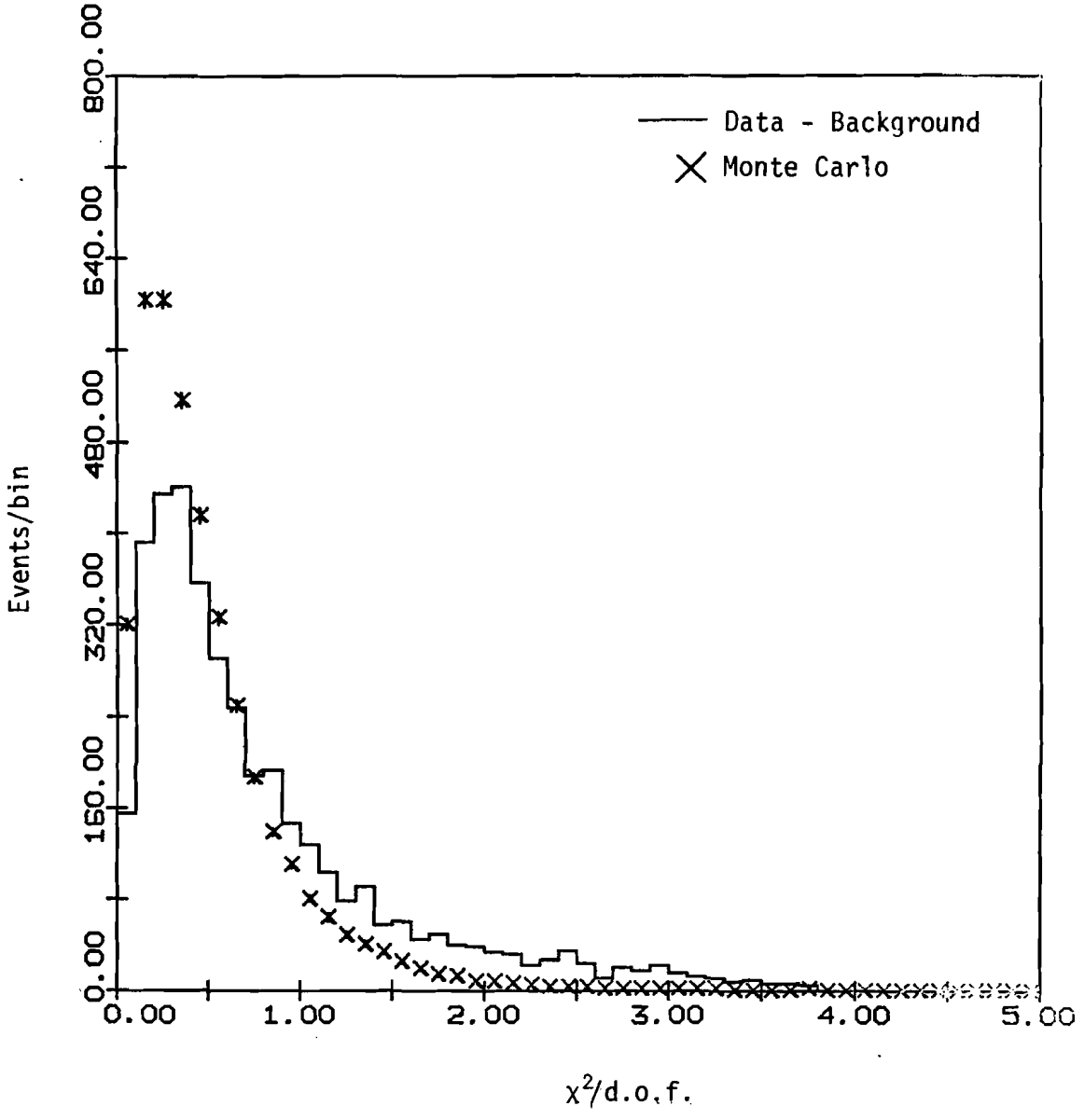
Data - Background
Monte Carlo
Events/bin
0.00
160.00
320.00
480.00
640.00
800.00
0.00
1.00
2.00
3.00
4.00
5.00
χ^2/d.o.f.

Figure 40.— A comparison of the data and Monte Carlo unconstrained χ^2 distributions for positive tracks.

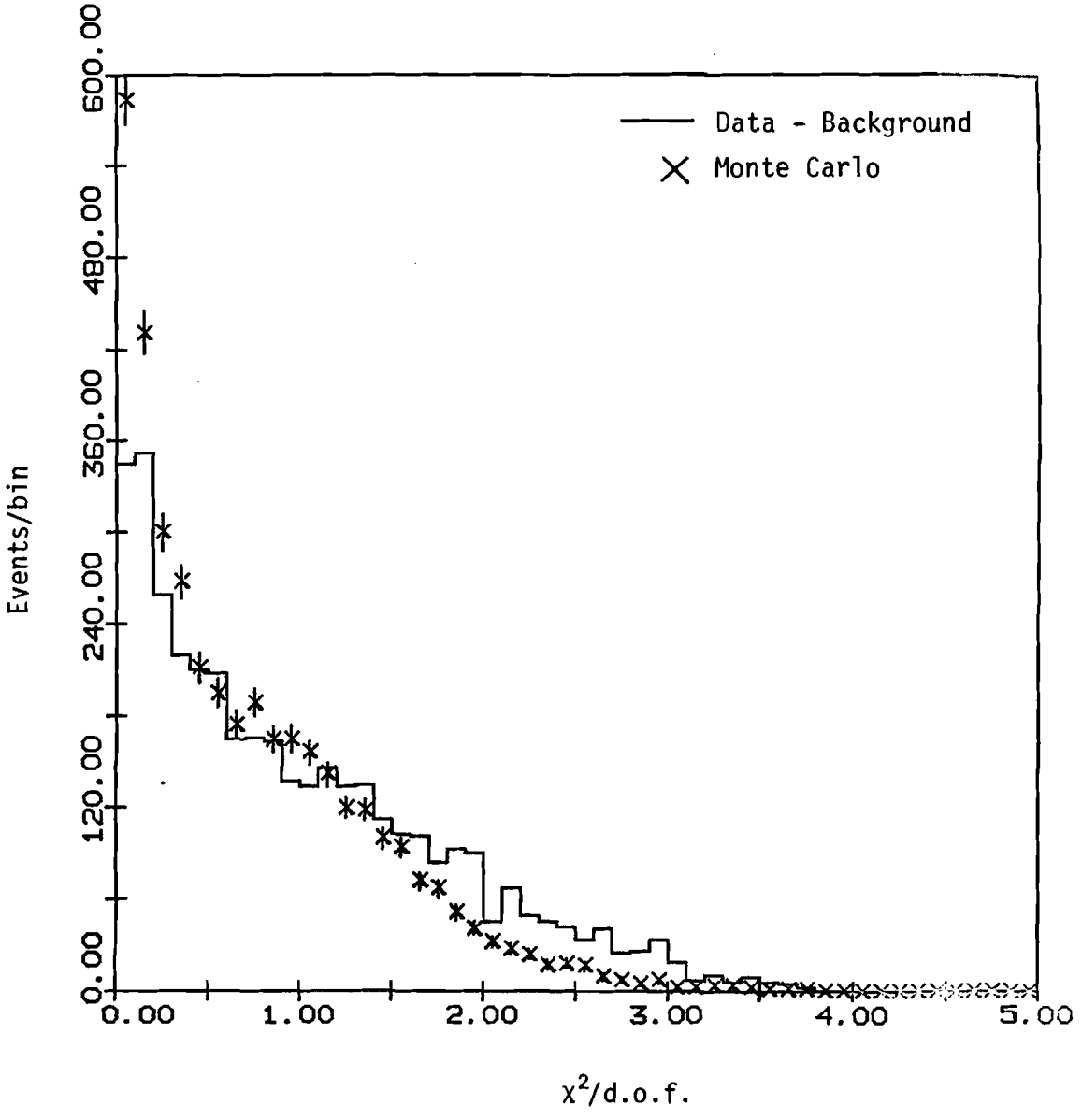
Data - Background
Monte Carlo
Events/bin
0.00
120.00
240.00
360.00
480.00
600.00
0.00
1.00
2.00
3.00
4.00
5.00
χ^2/d.o.f.

Figure 41.— A comparison of the data and Monte Carlo unconstrained χ^2 distributions for negative tracks.

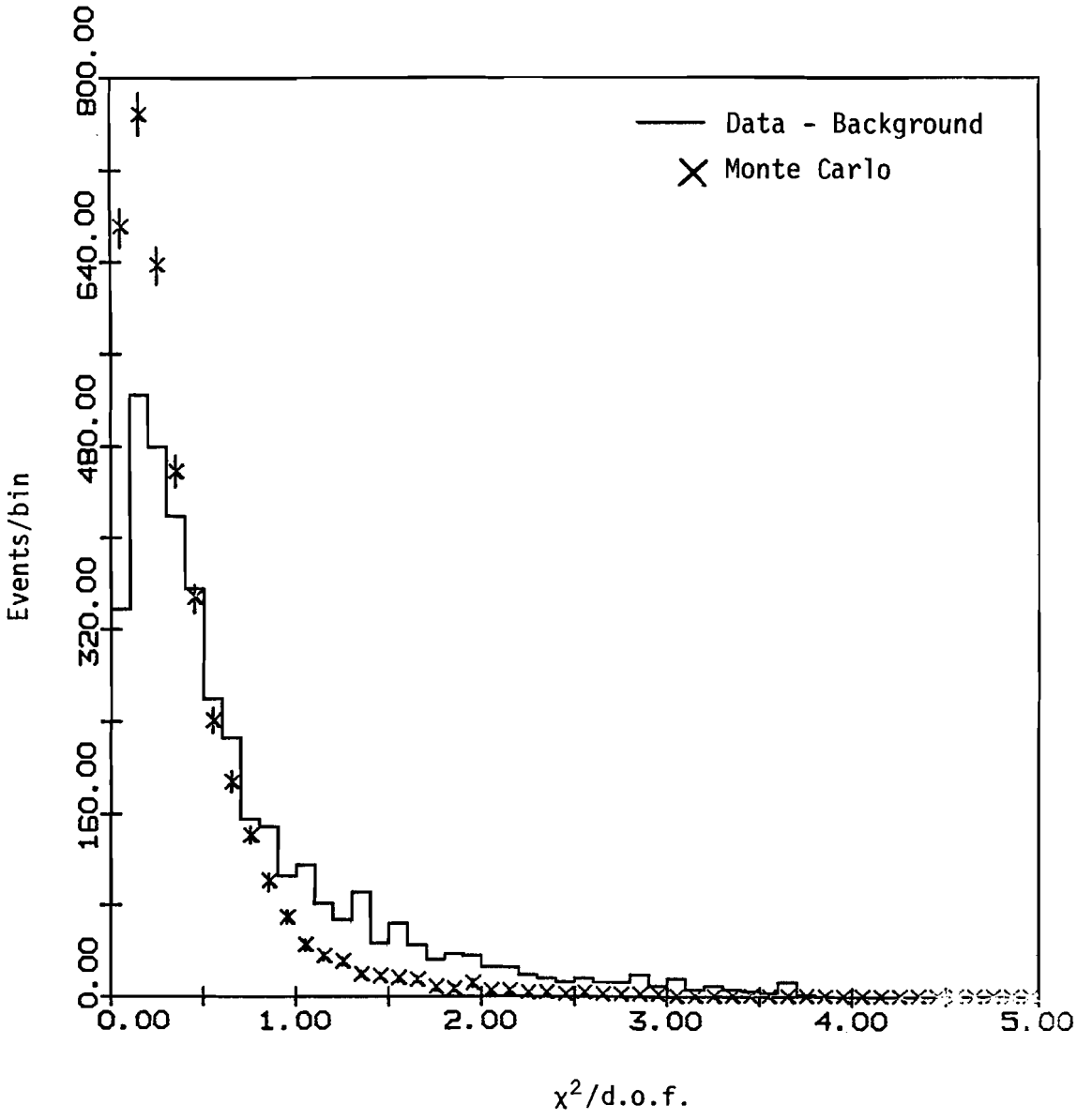
Data - Background
Monte Carlo
Events/bin
0.00
160.00
320.00
480.00
640.00
800.00
0.00
1.00
2.00
3.00
4.00
5.00
χ^2/d.o.f.

Figure 42.— A comparison of the data and Monte Carlo target distributions for positive tracks.

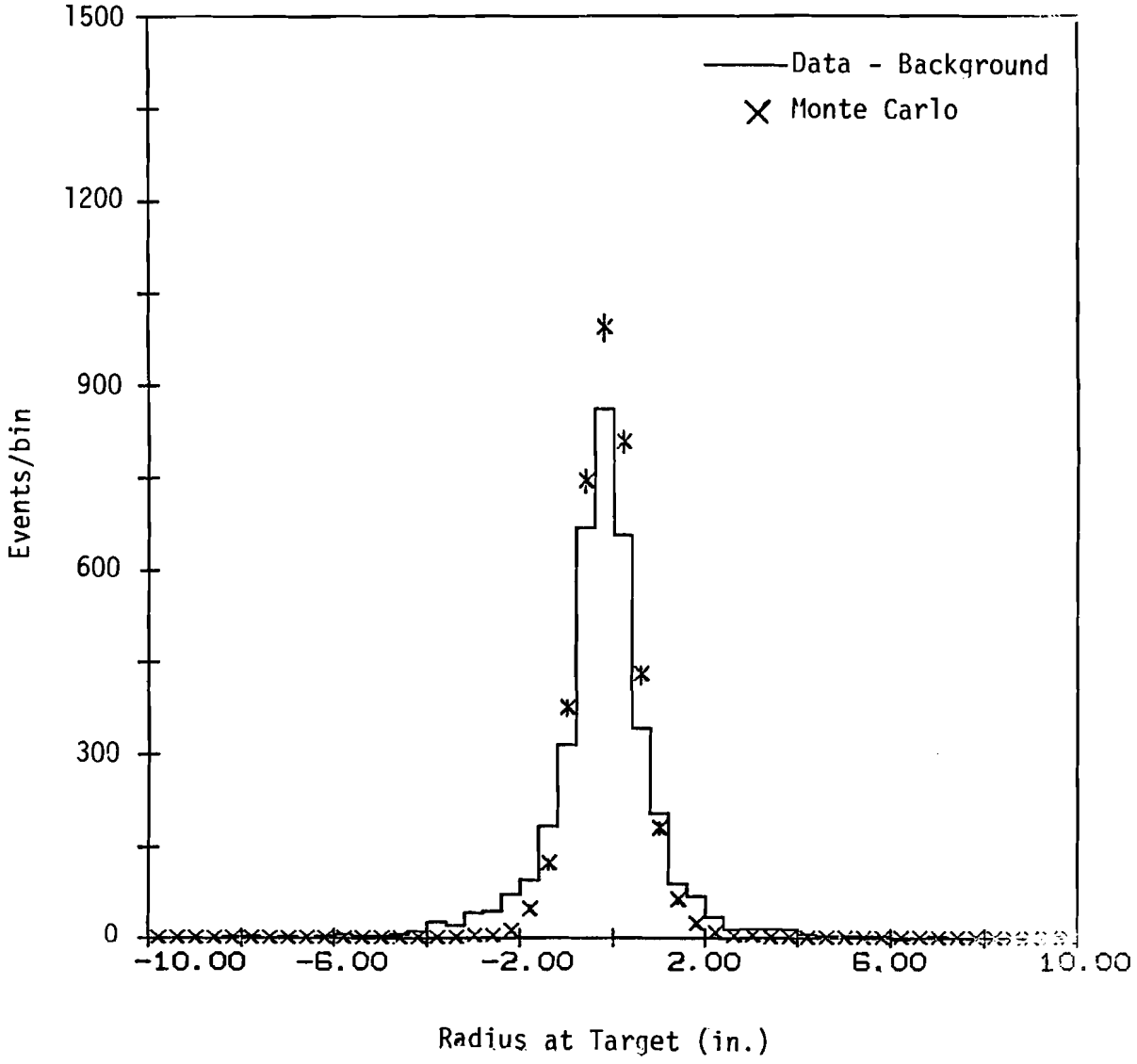
1500
1200
900
600
300
0
Events/bin
Data - Background
Monte Carlo
-10.00
-6.00
-2.00
2.00
6.00
10.00
Radius at Target (in.)

Figure 43.— A comparison of the data and Monte Carlo target distributions for negative tracks.

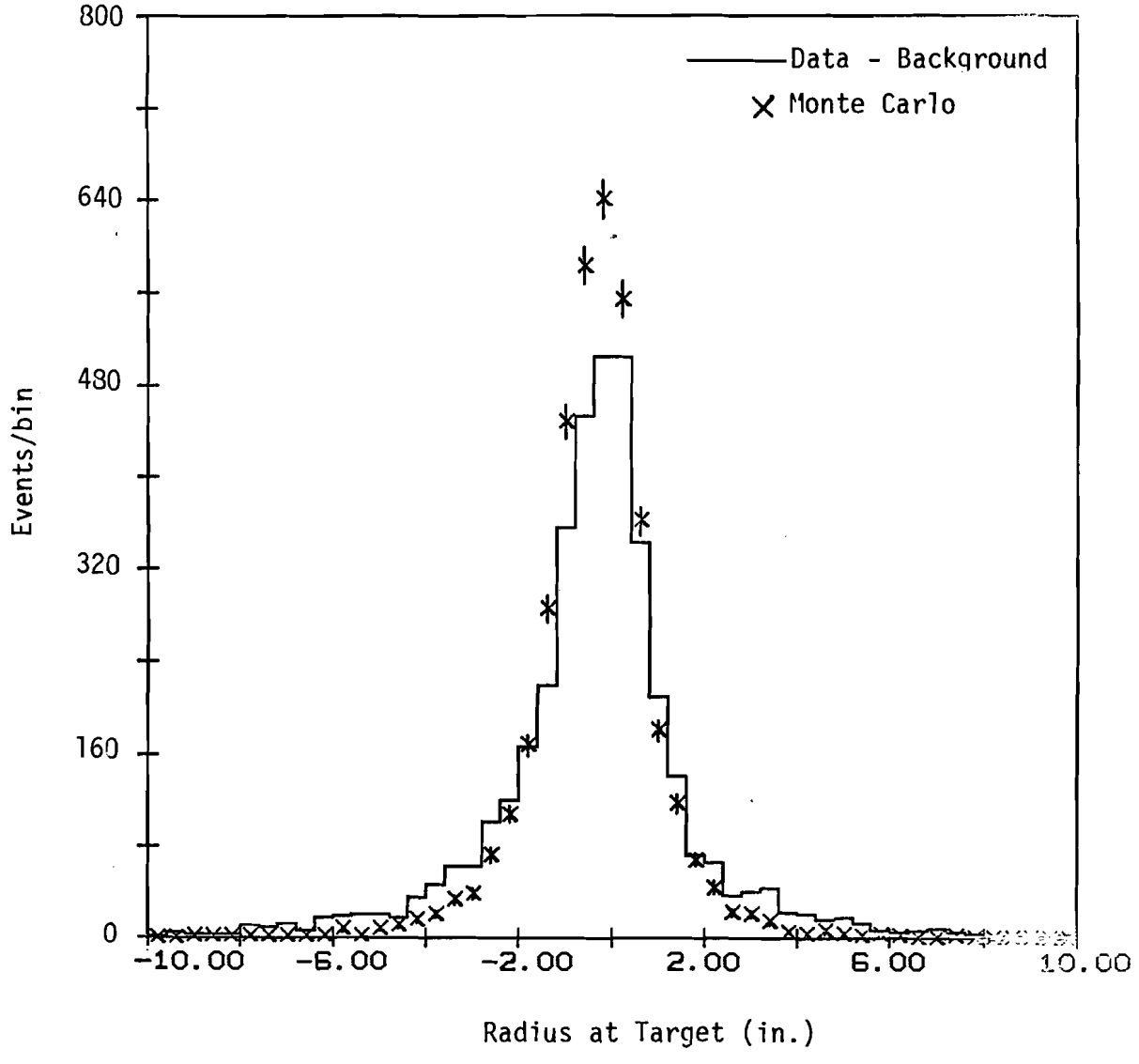
800
640
480
320
160
0
Events/bin
Data - Background
Monte Carlo
-10.00
-6.00
-2.00
2.00
6.00
10.00
Radius at Target (in.)

Figure 44.— Unsmearing corrections as a function of mass.

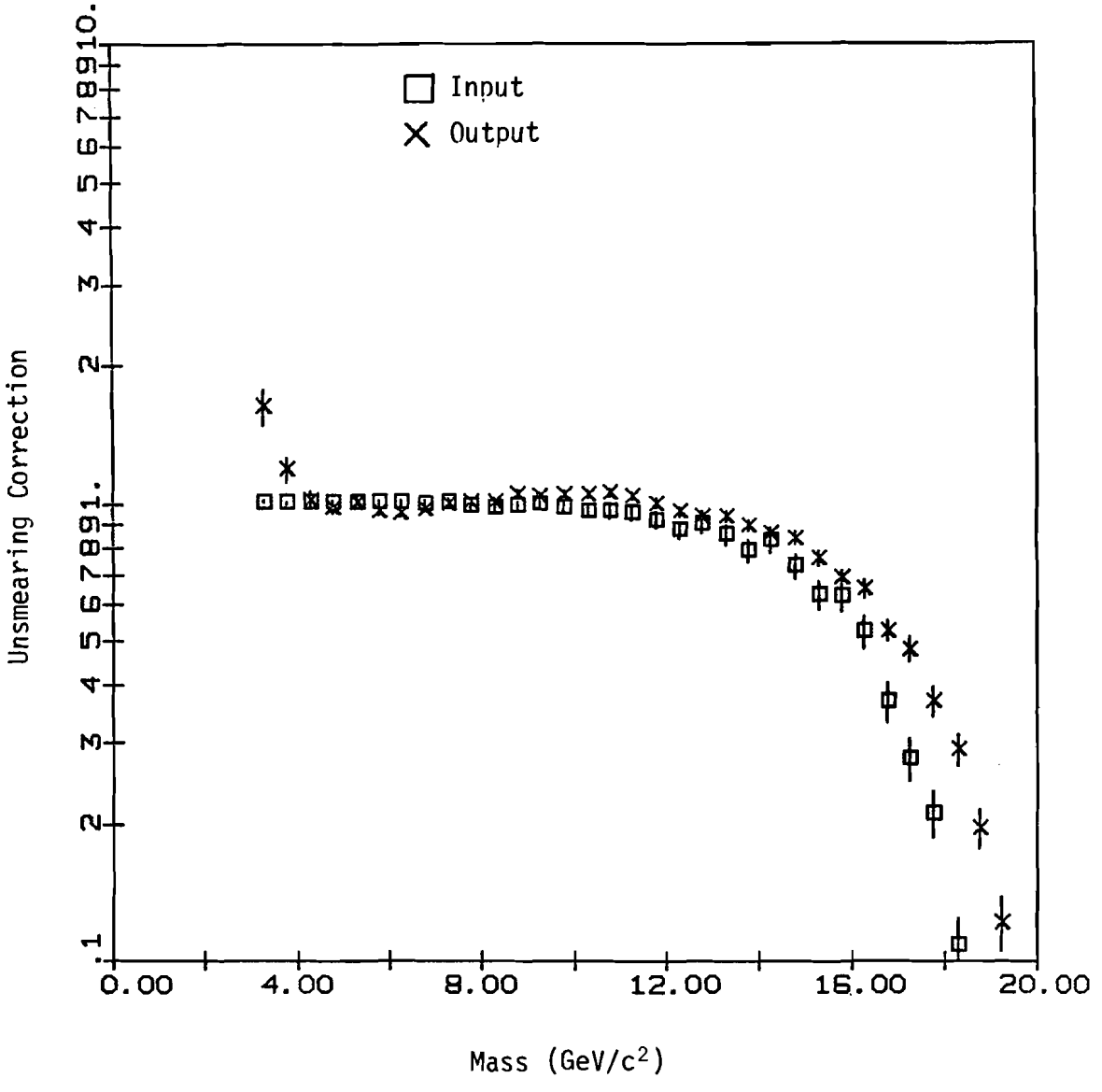
Input
Output
Unsmearing Correction
10.
9
8
7
6
5
4
3
2
1.
9
8
7
6
5
4
3
2
.1
0.00
4.00
8.00
12.00
16.00
20.00
Mass (GeV/c²)

Figure 45.— Unsmearing corrections as a function of p_T.

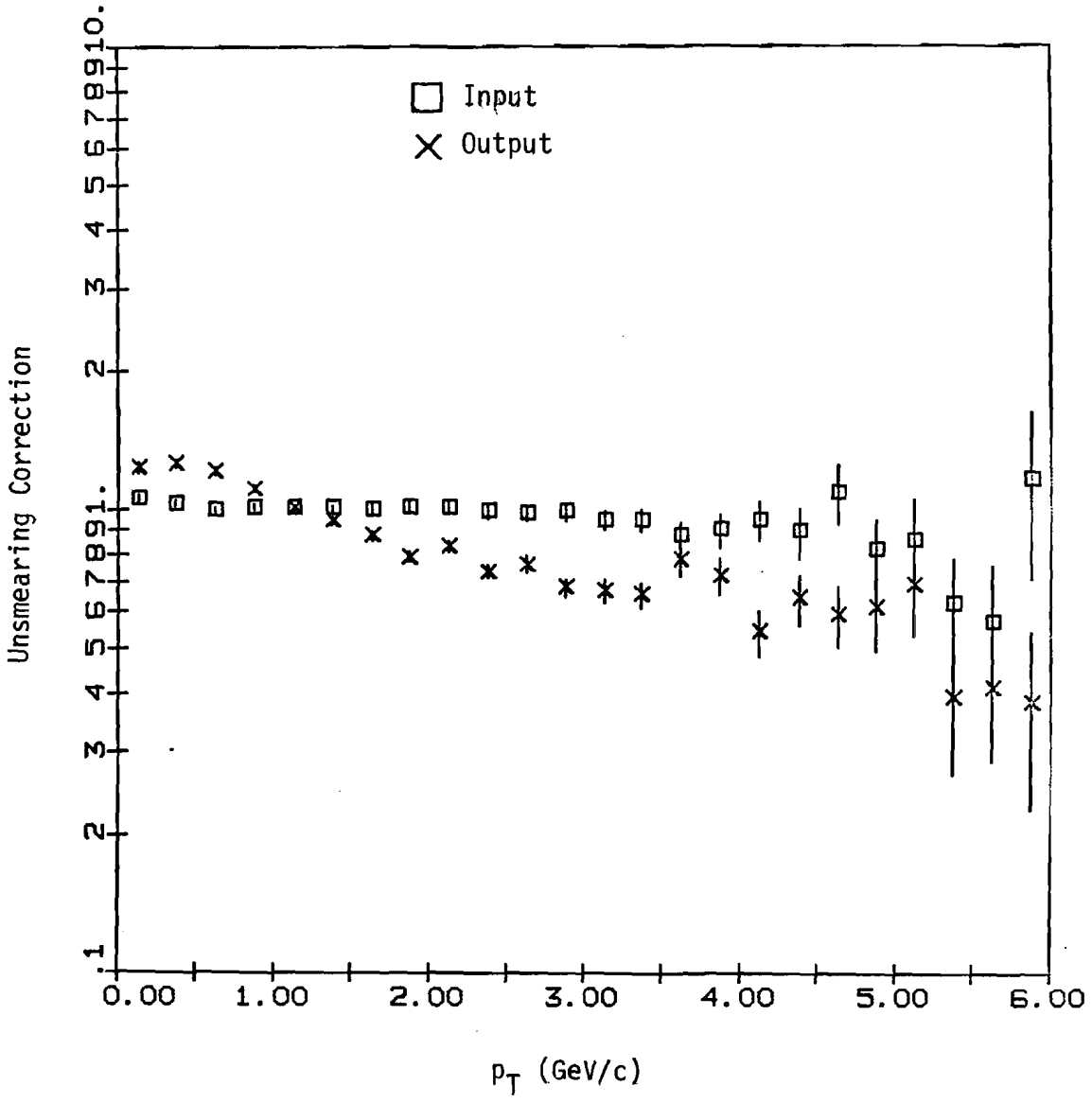
Input
Output
Unsmearing Correction
10.
9
8
7
6
5
4
3
2
1.
9
8
7
6
5
4
3
2
.1
0.00
1.00
2.00
3.00
4.00
5.00
6.00
p_T (GeV/c)

Figure 46.— Unsmearing corrections as a function of x_F.

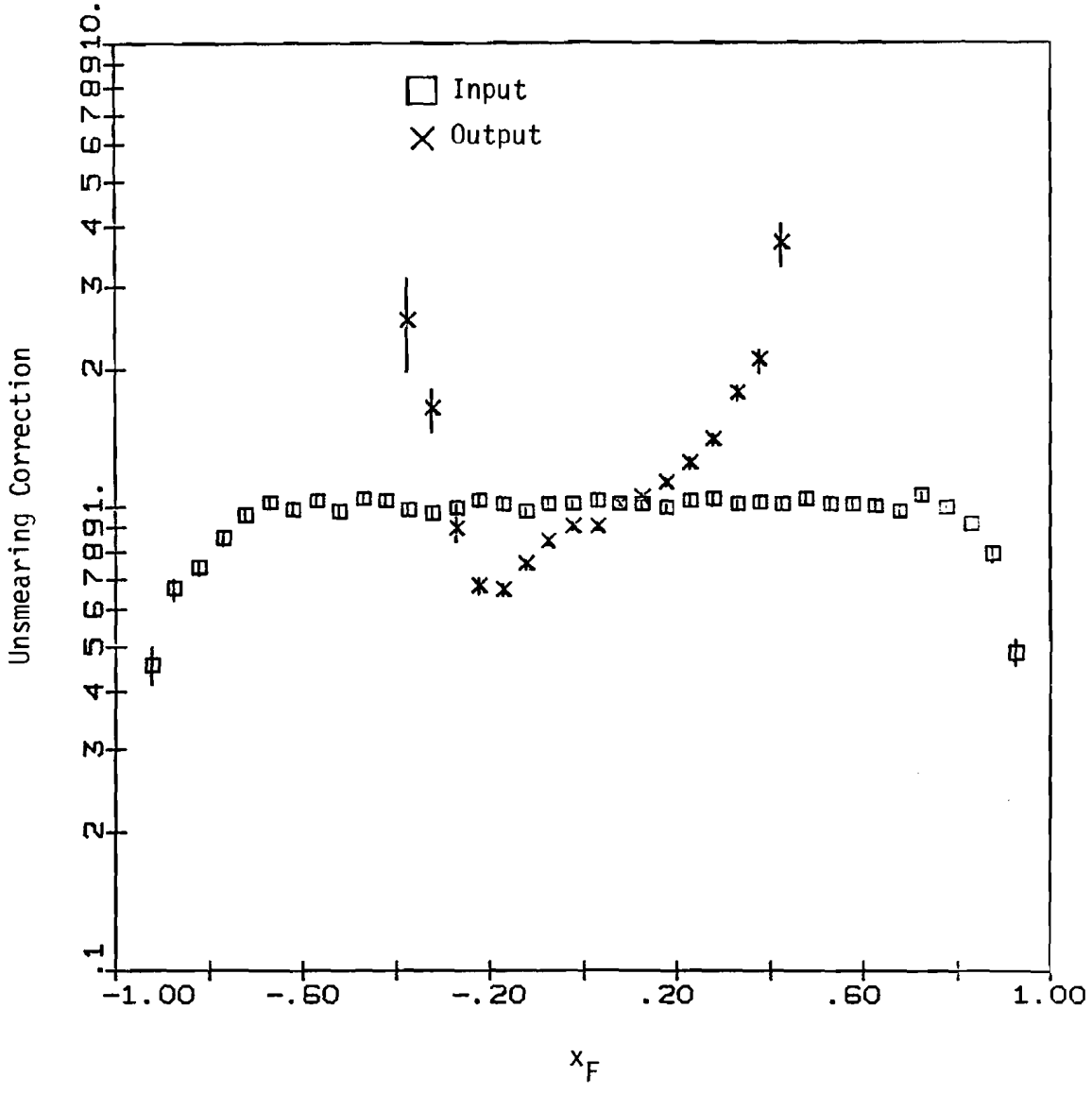
Input
Output
Unsmearing Correction
10.
9
8
7
6
5
4
3
2
1.
9
8
7
6
5
4
3
2
.1
-1.00
-.60
-.20
.20
.60
1.00
x_F

Figure 47.— A comparison of the data and Monte Carlo z vertex distributions.

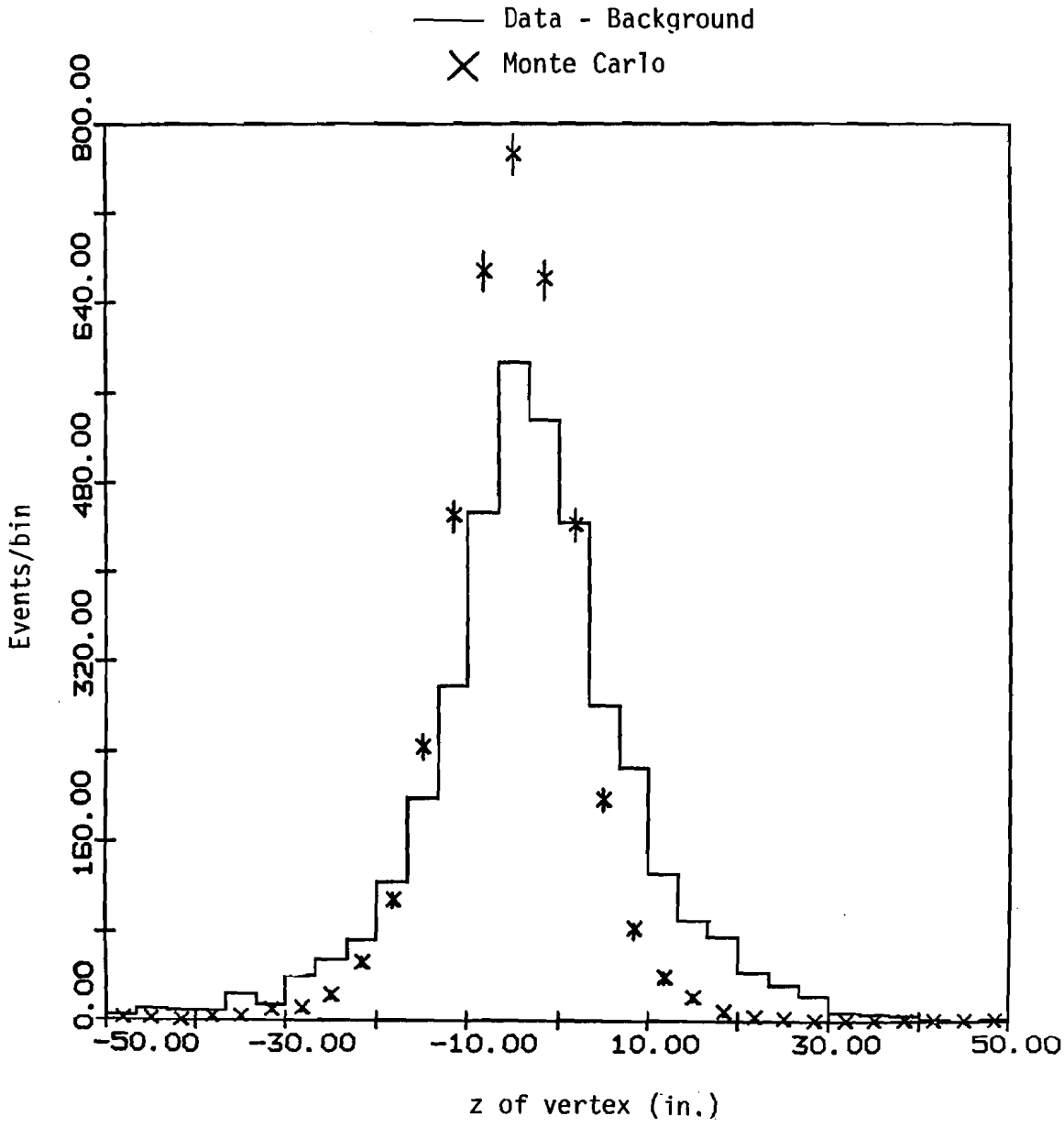
Data - Background
Monte Carlo
Events/bin
0.00
160.00
320.00
480.00
640.00
800.00
-50.00
-30.00
-10.00
10.00
30.00
50.00
z of vertex (in.)

Figure 48.— Raw mass spectrum, background and acceptance.

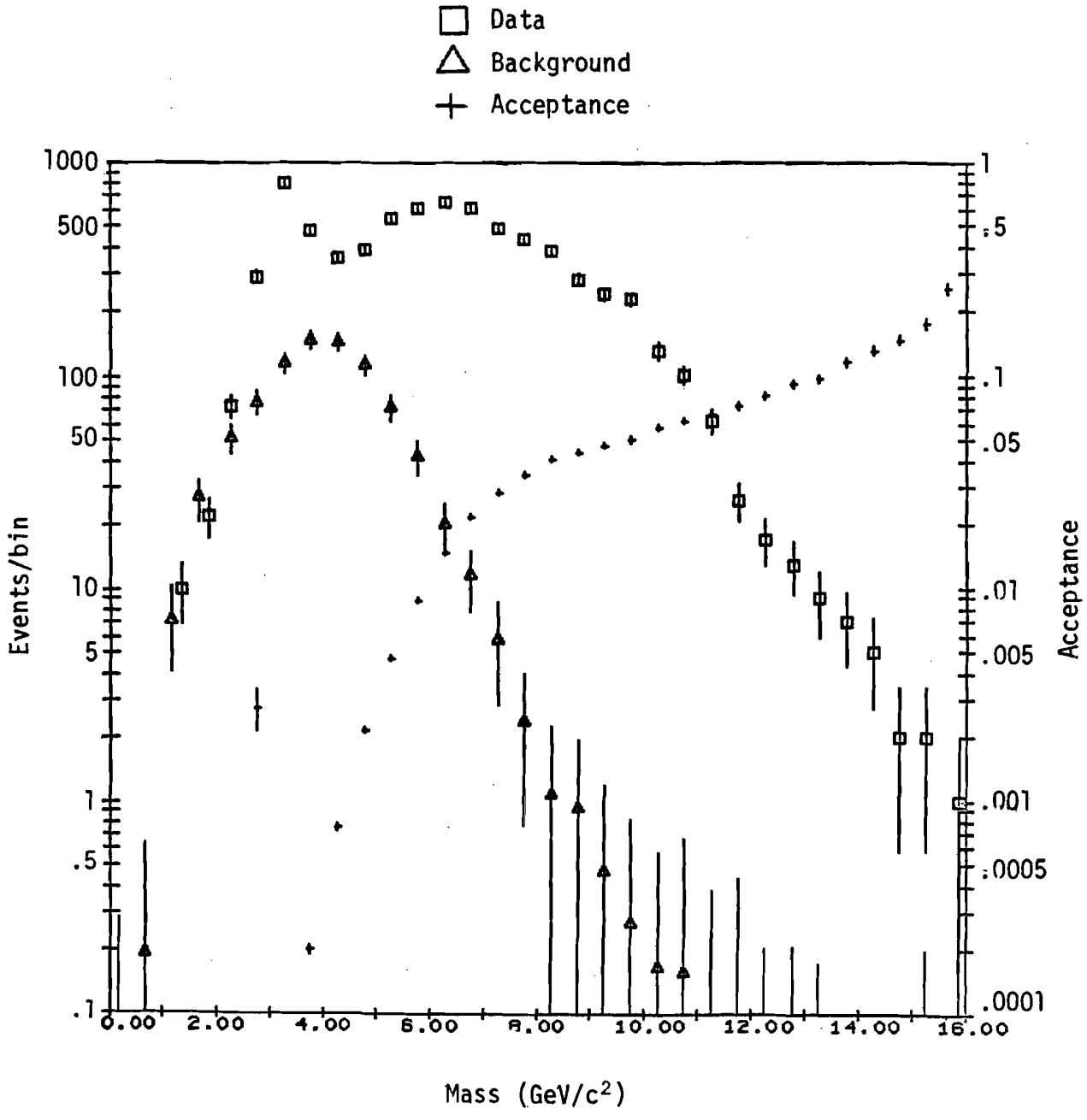
Data
Background
Acceptance
Events/bin
Acceptance
Mass (GeV/c²)
1000
500
100
50
10
5
1
.5
.1
1
.5
.1
.05
.01
.005
.001
.0005
.0001
0.00
2.00
4.00
6.00
8.00
10.00
12.00
14.00
16.00

Figure 49.— Raw p_T spectrum and background.

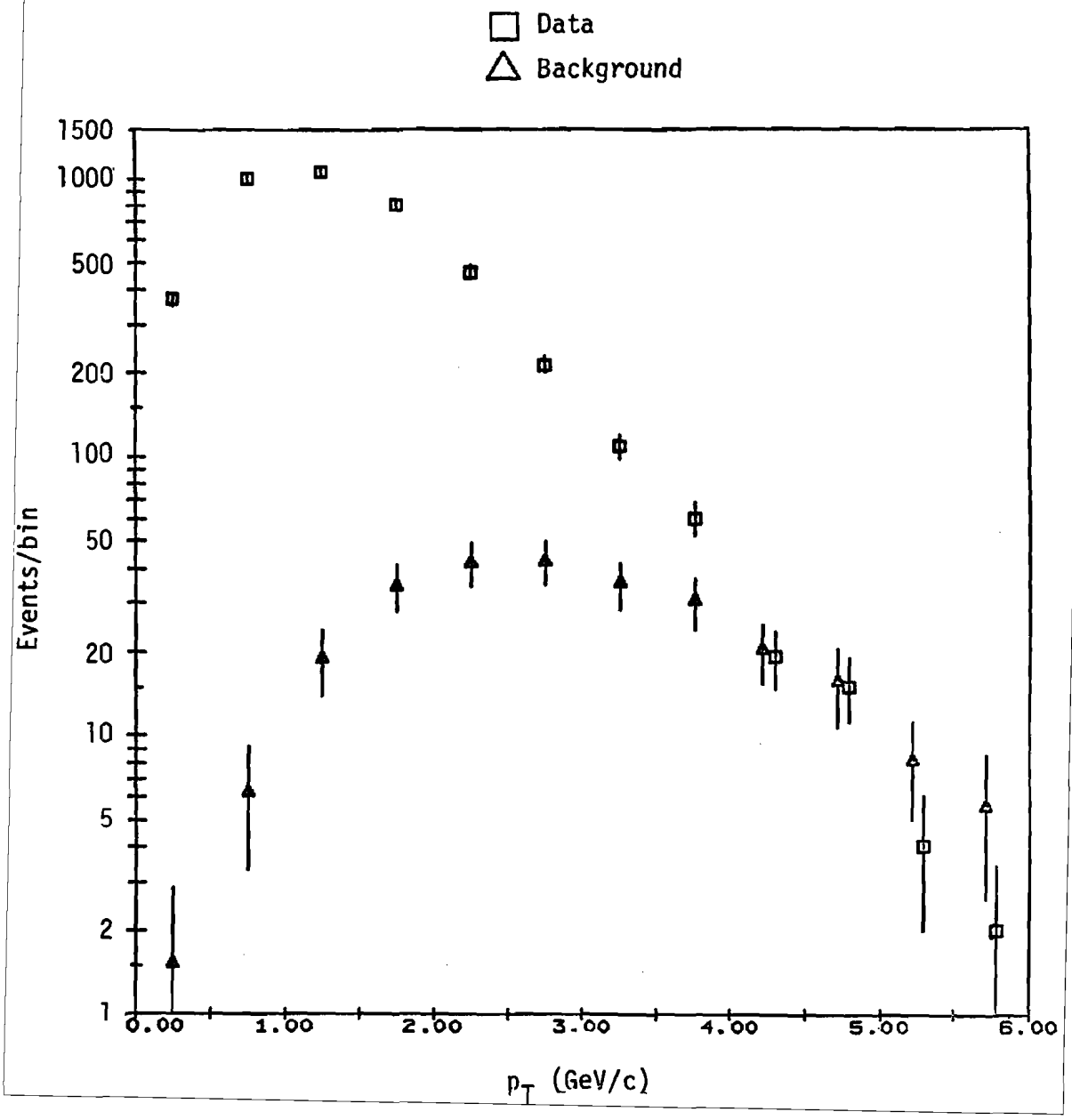
Data
Background
1500
1000
500
200
100
50
20
10
5
2
1
Events/bin
0.00
1.00
2.00
3.00
4.00
5.00
6.00
p_T (GeV/c)

Figure 50.— Raw x_F spectrum and background.

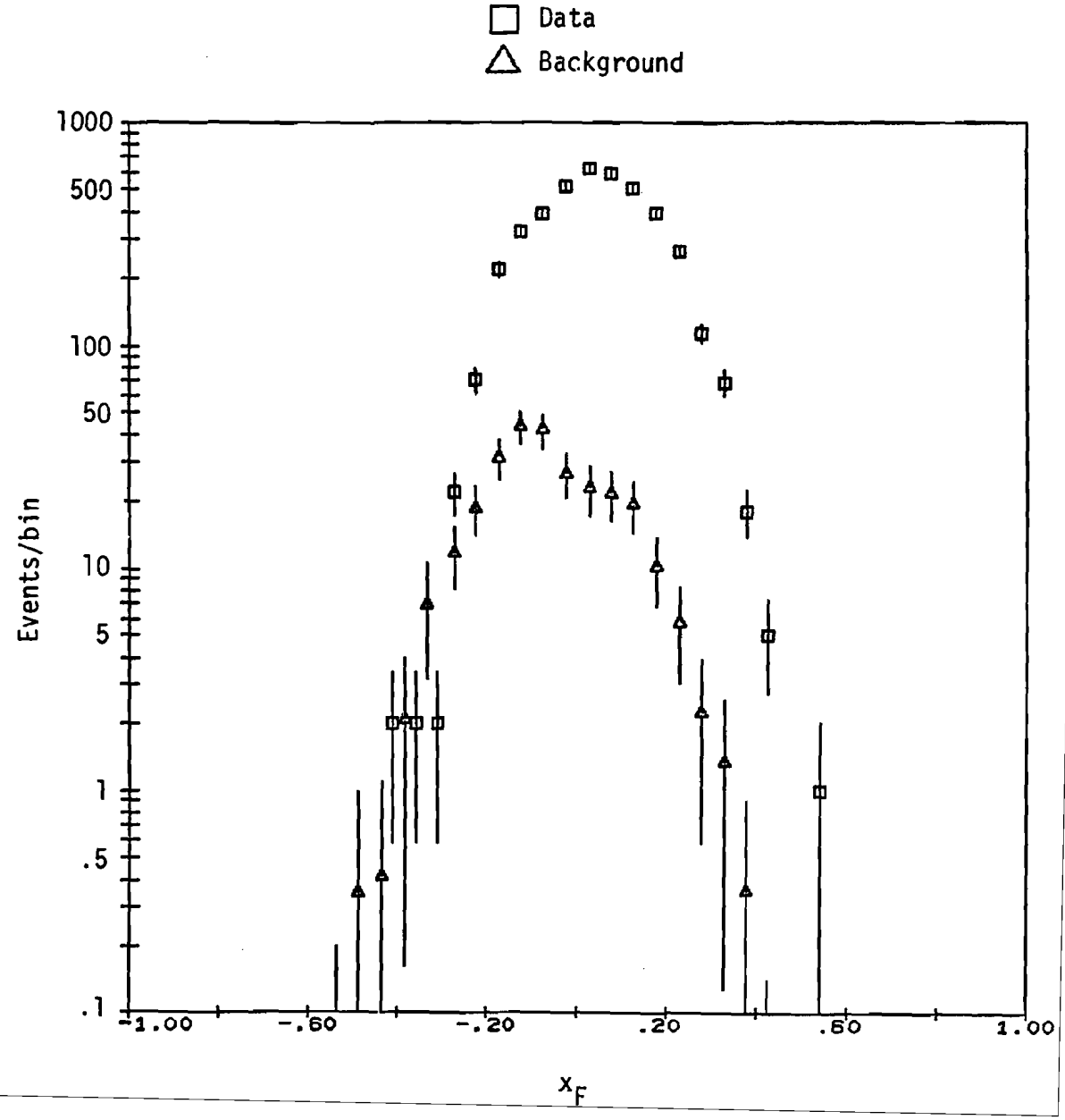
Data
Background
1000
500
100
50
10
5
1
.5
.1
Events/bin
-1.00
-.60
-.20
.20
.60
1.00
x_F

Figure 51.— p_T acceptance as a function of p_T and mass.

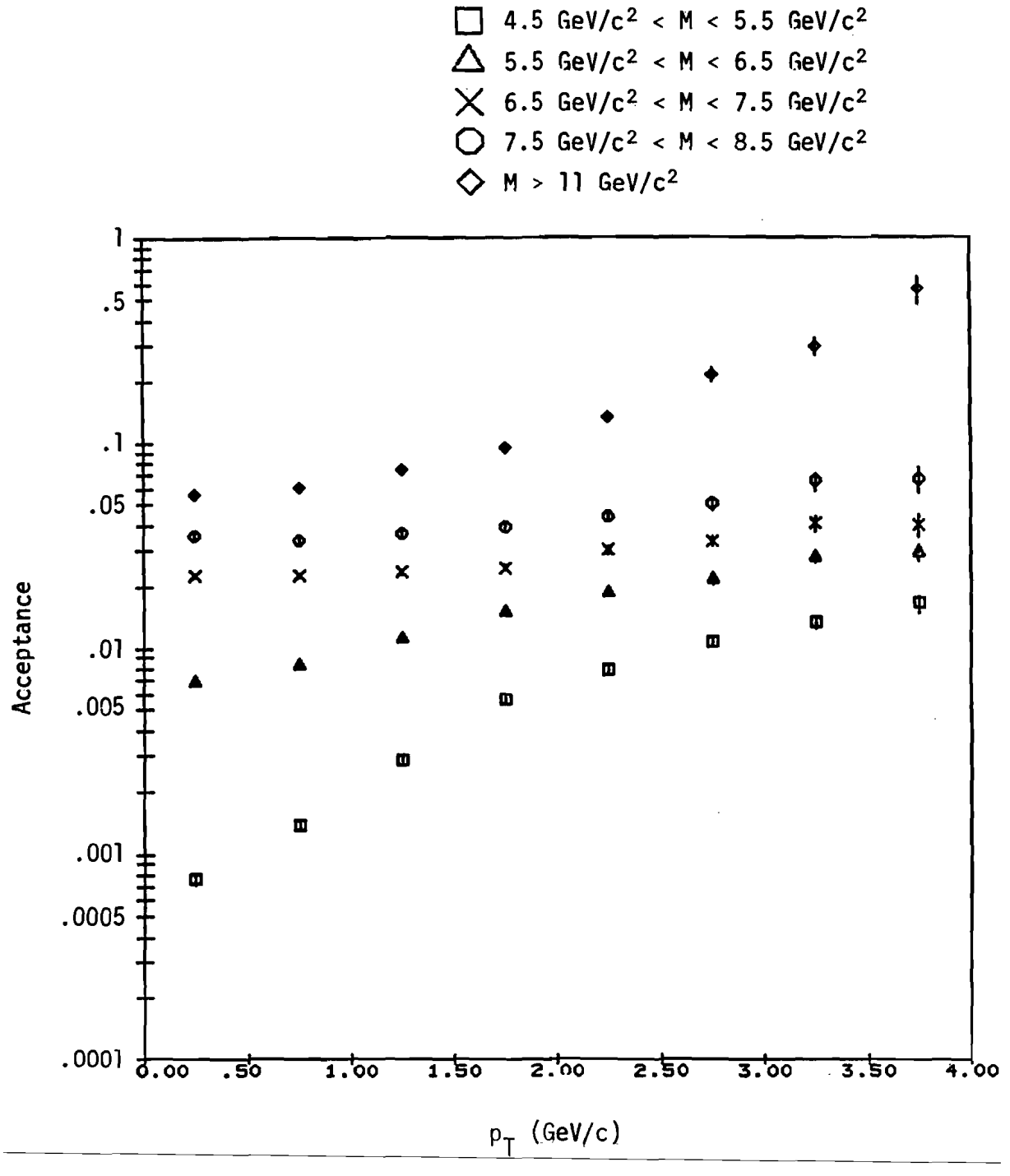
4.5 GeV/c² < M < 5.5 GeV/c²
5.5 GeV/c² < M < 6.5 GeV/c²
6.5 GeV/c² < M < 7.5 GeV/c²
7.5 GeV/c² < M < 8.5 GeV/c²
M > 11 GeV/c²
Acceptance
1
.5
.1
.05
.01
.005
.001
.0005
.0001
0.00
.50
1.00
1.50
2.00
2.50
3.00
3.50
4.00
p_T (GeV/c)

Figure 52.— x_F acceptance as a function of x_F and mass.

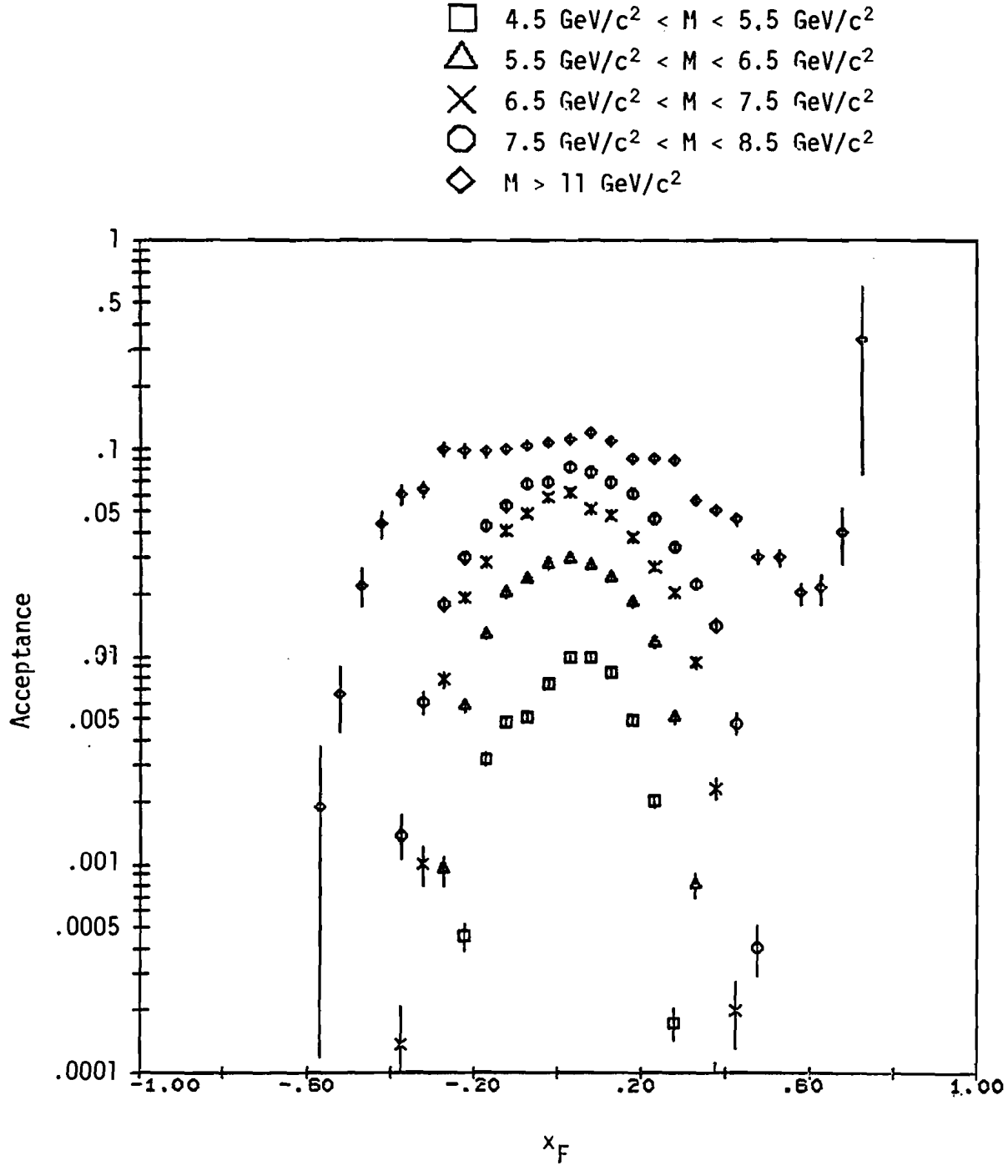
4.5 GeV/c² < M < 5.5 GeV/c²
5.5 GeV/c² < M < 6.5 GeV/c²
6.5 GeV/c² < M < 7.5 GeV/c²
7.5 GeV/c² < M < 8.5 GeV/c²
M > 11 GeV/c²
Acceptance
1
.5
.1
.05
.01
.005
.001
.0005
.0001
-1.00
-.60
-.20
.20
.60
1.00
x_F

Figure 53.— A scatter plot of events in mass vs. x_F. The binning used in the structure function analysis is superimposed.

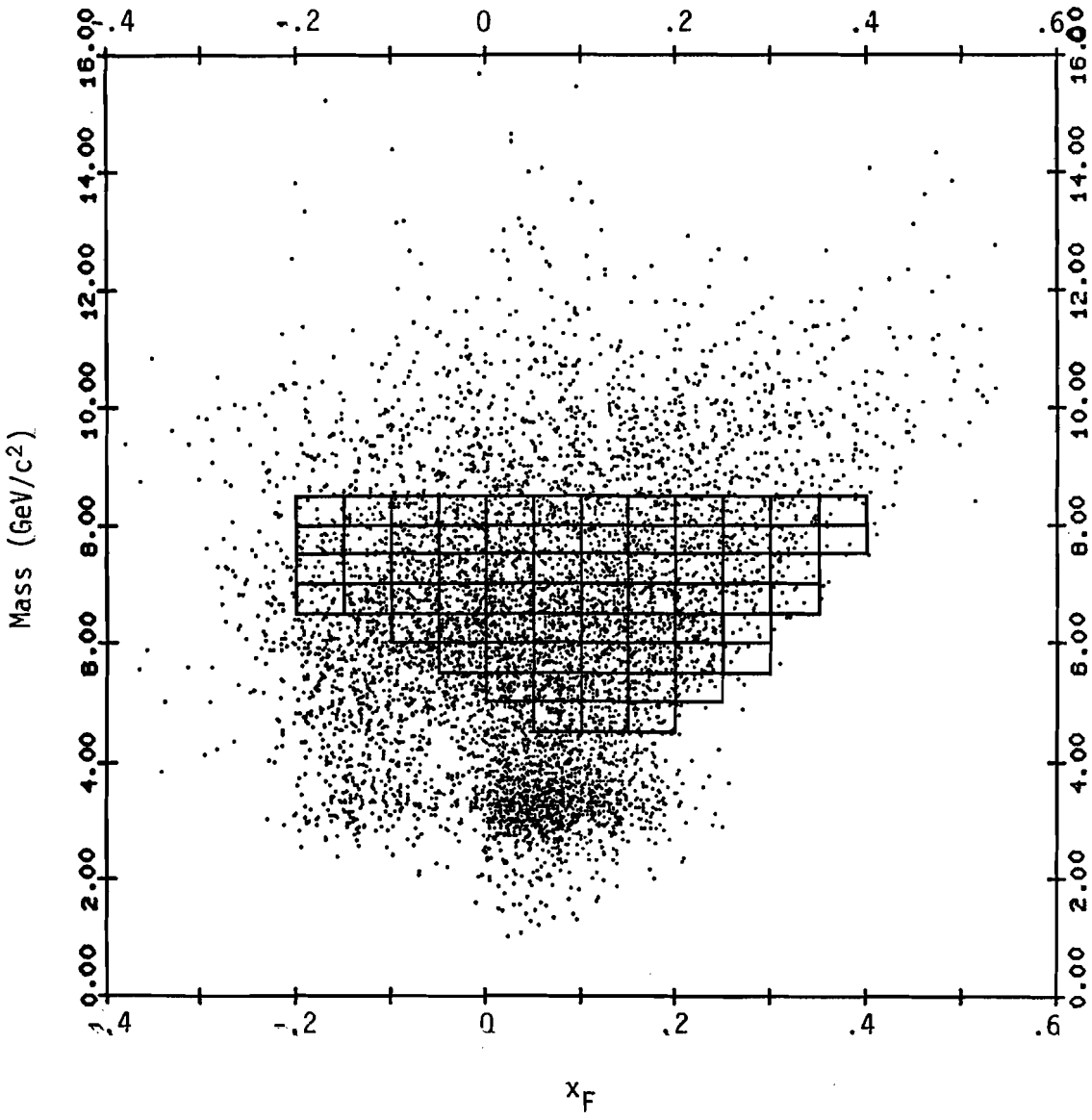
-.4
-.2
0
.2
.4
.6
16.00
14.00
12.00
10.00
8.00
6.00
4.00
2.00
0.00
Mass (GeV/c²)
x_F

Figure 54.— A plot of $d\sigma/dx_1$ comparing our data with the Drell-Yan model using our pion structure function.

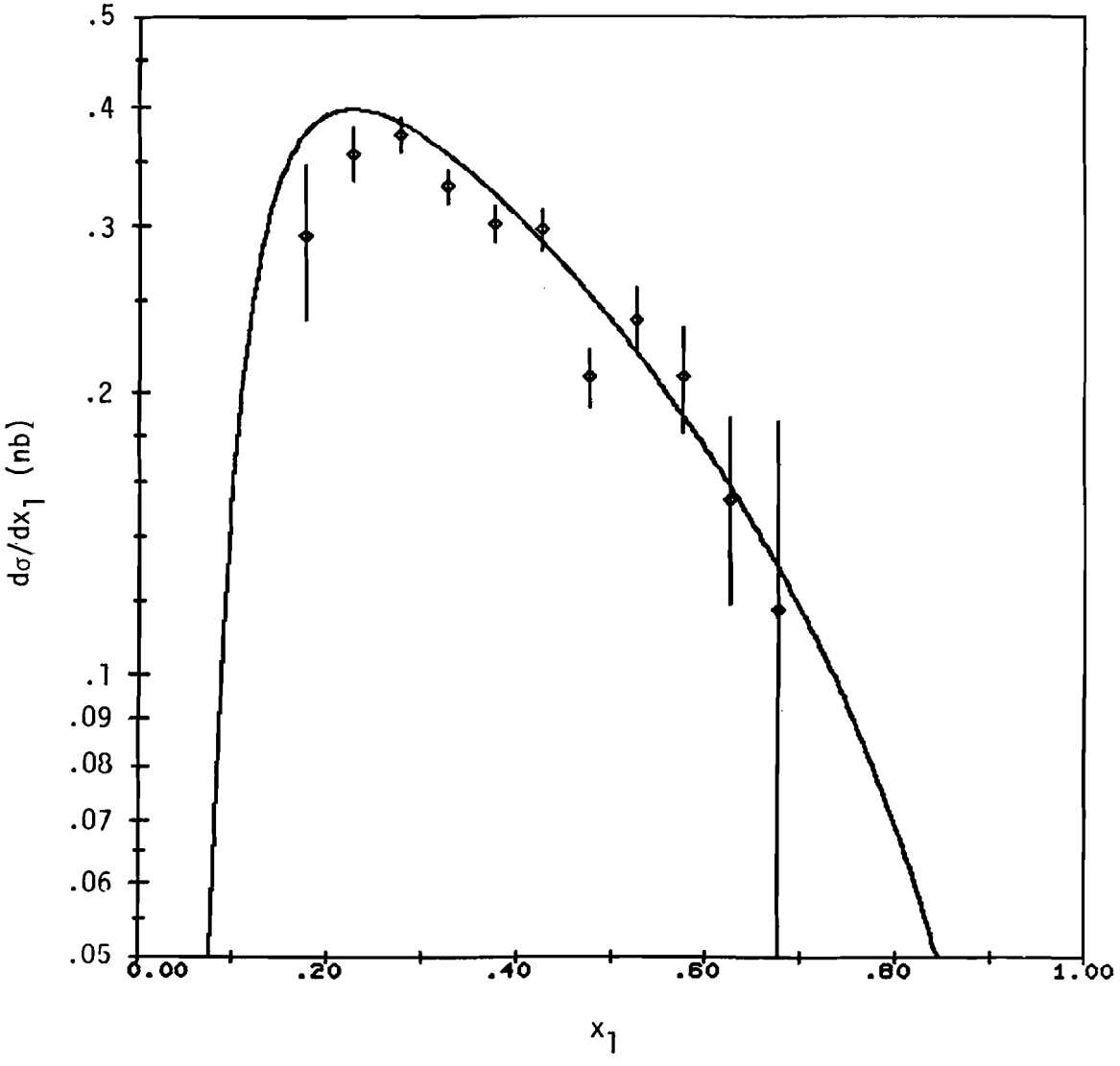
.5
.4
.3
.2
.1
.09
.08
.07
.06
.05
dσ/dx1 (nb)
0.00
.20
.40
.60
.80
1.00
x1

Figure 55.— A plot of $d\sigma/dx_2$ comparing our data with the Drell-Yan model using our pion structure function.

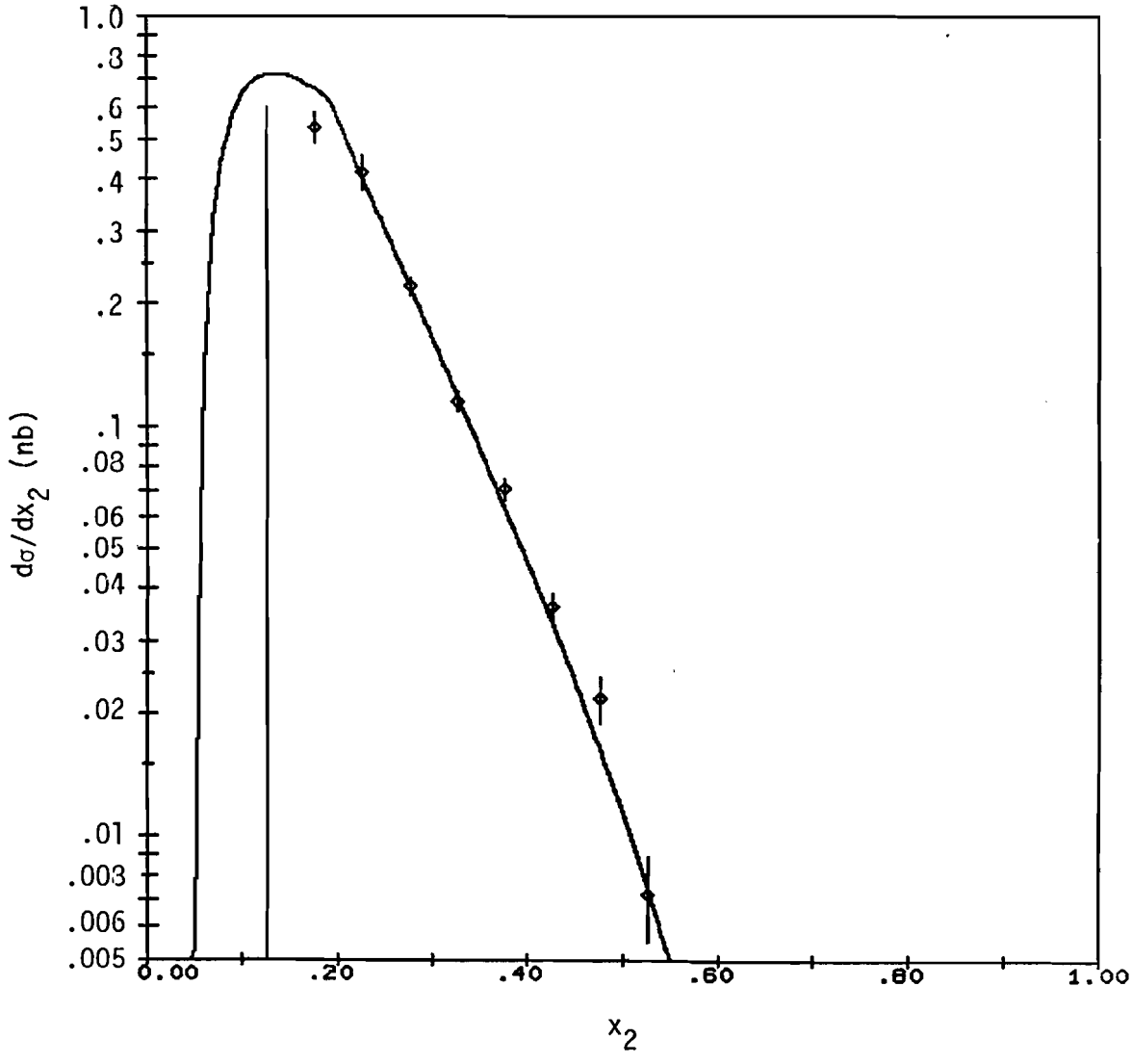
1.0
.8
.6
.5
.4
.3
.2
.1
.08
.06
.05
.04
.03
.02
.01
.003
.006
.005
0.00
.20
.40
.60
.80
1.00
$d\sigma/dx_2$ (nb)
x_2

Figure 56.— A plot of $d\sigma/dM$ comparing our data with our fit.

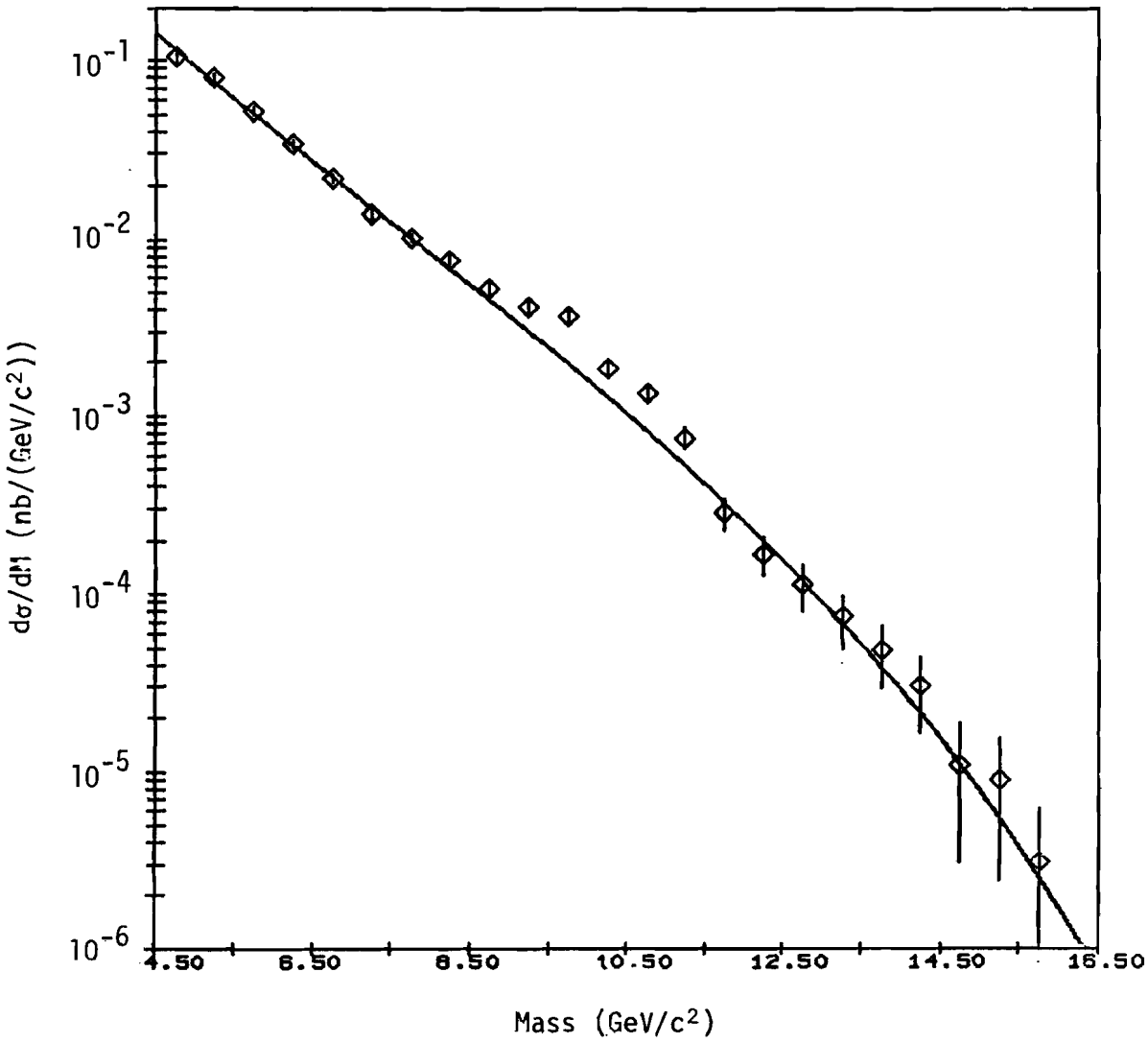
10^{-1}
10^{-2}
10^{-3}
10^{-4}
10^{-5}
10^{-6}
dσ/dM (nb/(GeV/c²))
4.50
6.50
8.50
10.50
12.50
14.50
16.50
Mass (GeV/c²)

Figure 57.— A plot of $d\sigma/dM$ comparing our data with the prediction of the naive Drell-Yan model using our pion structure function.

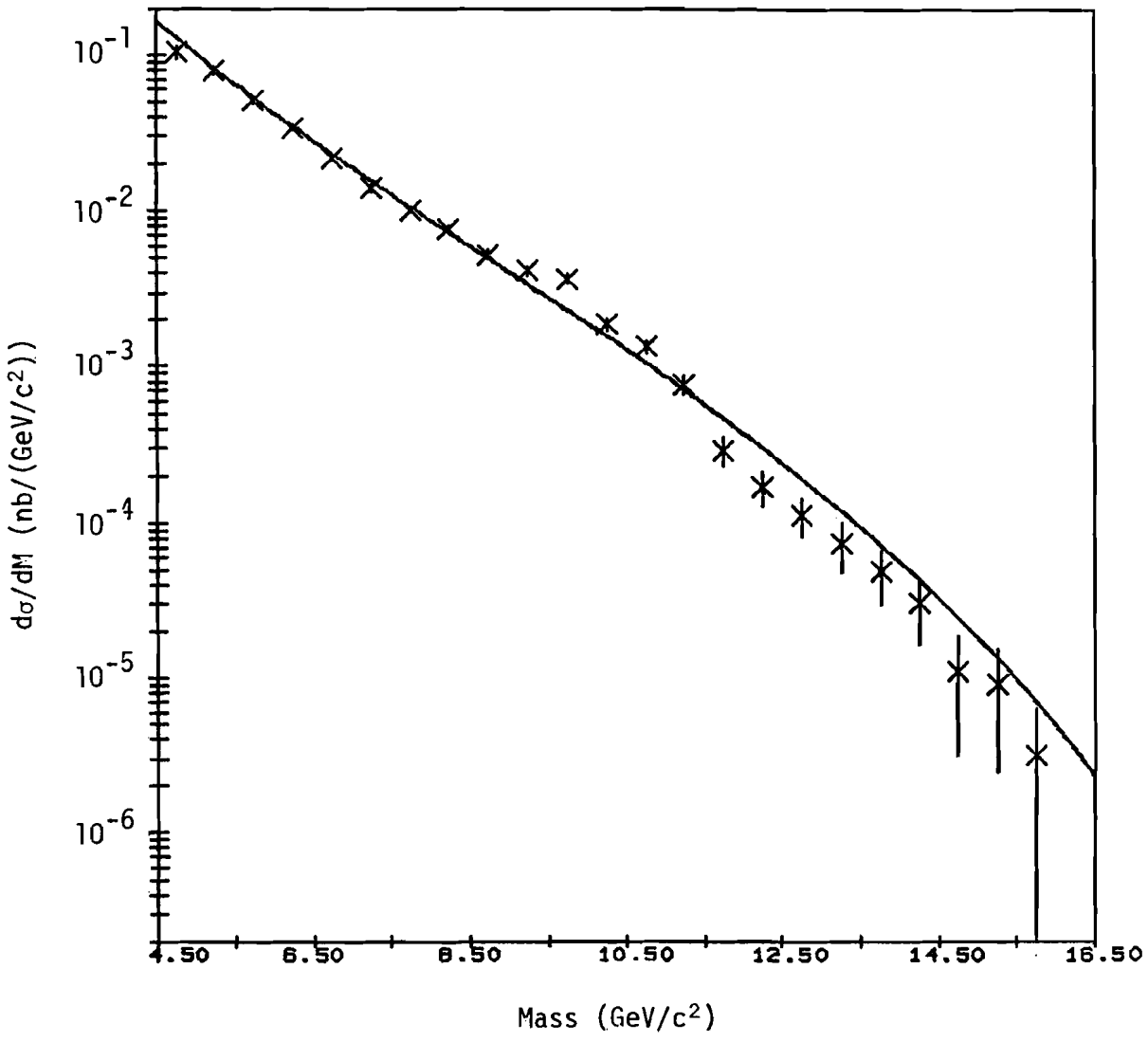
10^{-1}
10^{-2}
10^{-3}
10^{-4}
10^{-5}
10^{-6}
$d\sigma/dM$ (nb/(GeV/c^2))
4.50
6.50
8.50
10.50
12.50
14.50
16.50
Mass (GeV/c^2)

Figure 58.— A plot of $d\sigma/dM$ comparing our data with the prediction of the Drell-Yan model incorporating QCD leading log scaling violations in the structure functions and using our pion structure function.

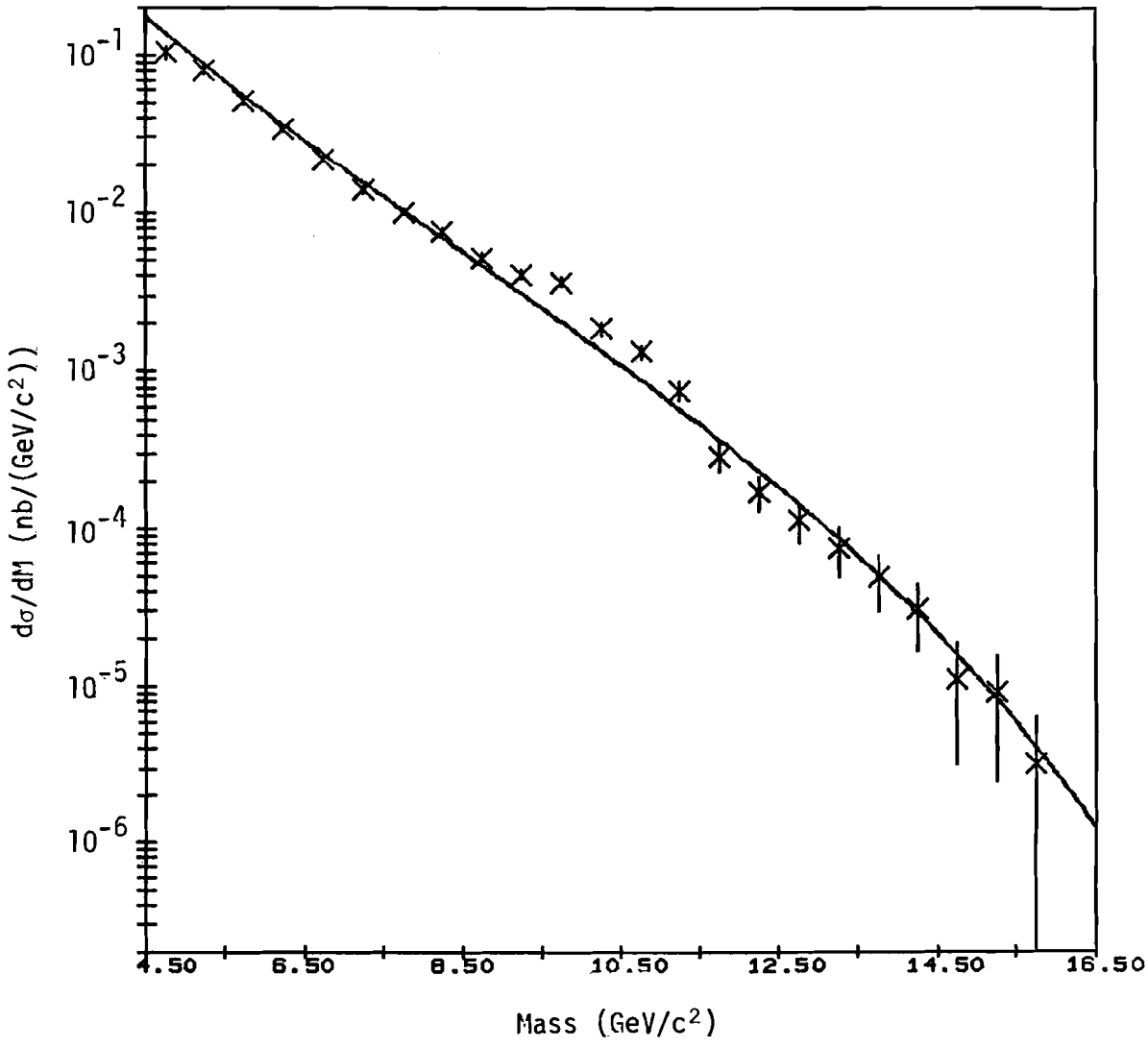
10^{-1}
10^{-2}
10^{-3}
10^{-4}
10^{-5}
10^{-6}
$d\sigma/dM$ (nb/(GeV/c^2))
4.50
6.50
8.50
10.50
12.50
14.50
16.50
Mass (GeV/c^2)

Figure 59.— A plot of $d\sigma/dM$ comparing our data with the prediction of the Drell-Yan model incorporating QCD leading log scaling violations in the structure functions and using the world average pion structure function.

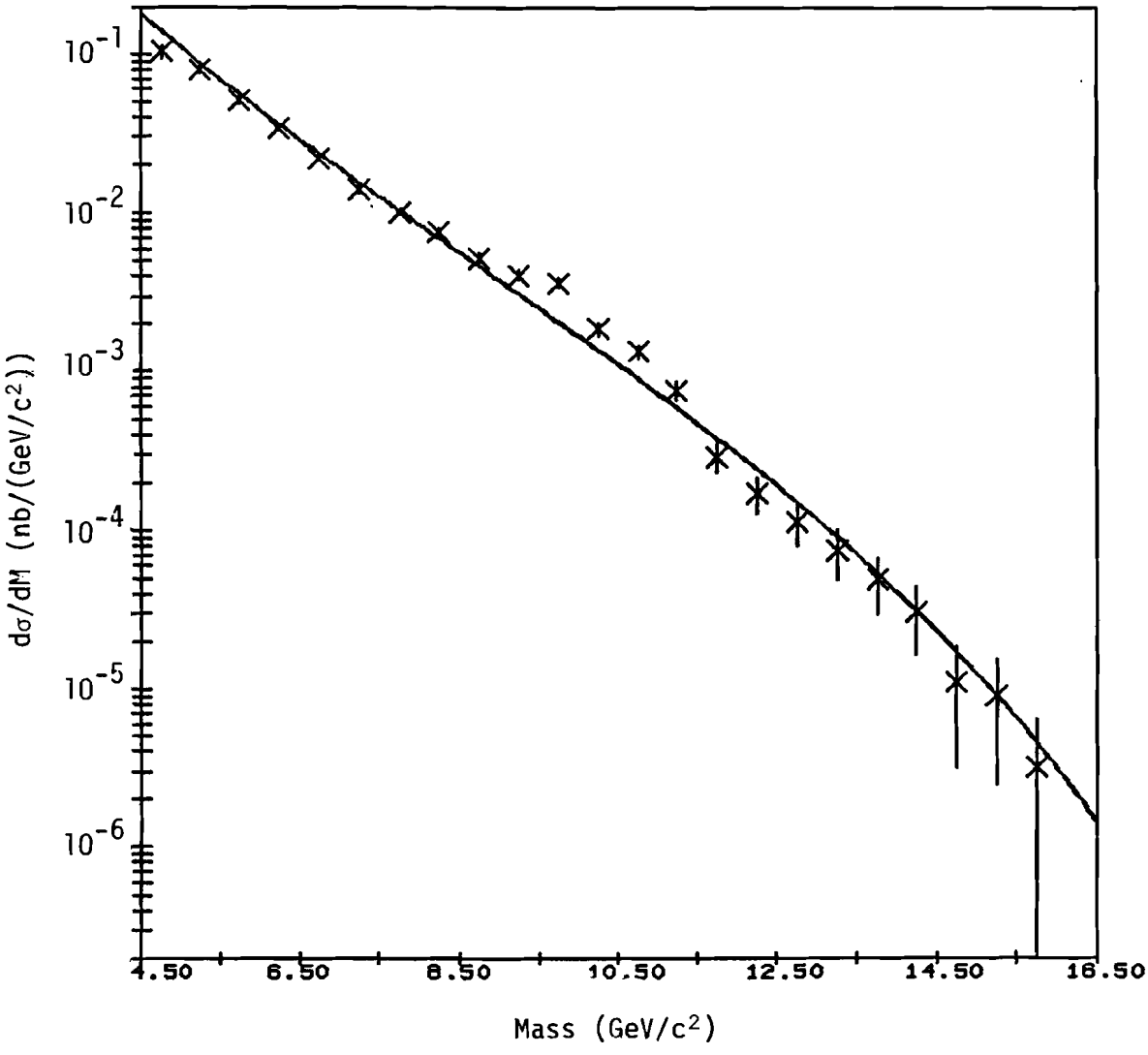
10^{-1}
10^{-2}
10^{-3}
10^{-4}
10^{-5}
10^{-6}
$d\sigma/dM$ (nb/(GeV/c^2))
4.50
6.50
8.50
10.50
12.50
14.50
16.50
Mass (GeV/c^2)

Figure 60.— A plot of $d\sigma/dx_F$ comparing our data with the prediction of the Drell-Yan model for $M>11$ GeV/c^2. The Drell-Yan model prediction incorporates QCD leading log scaling violations and uses the world average pion structure function.

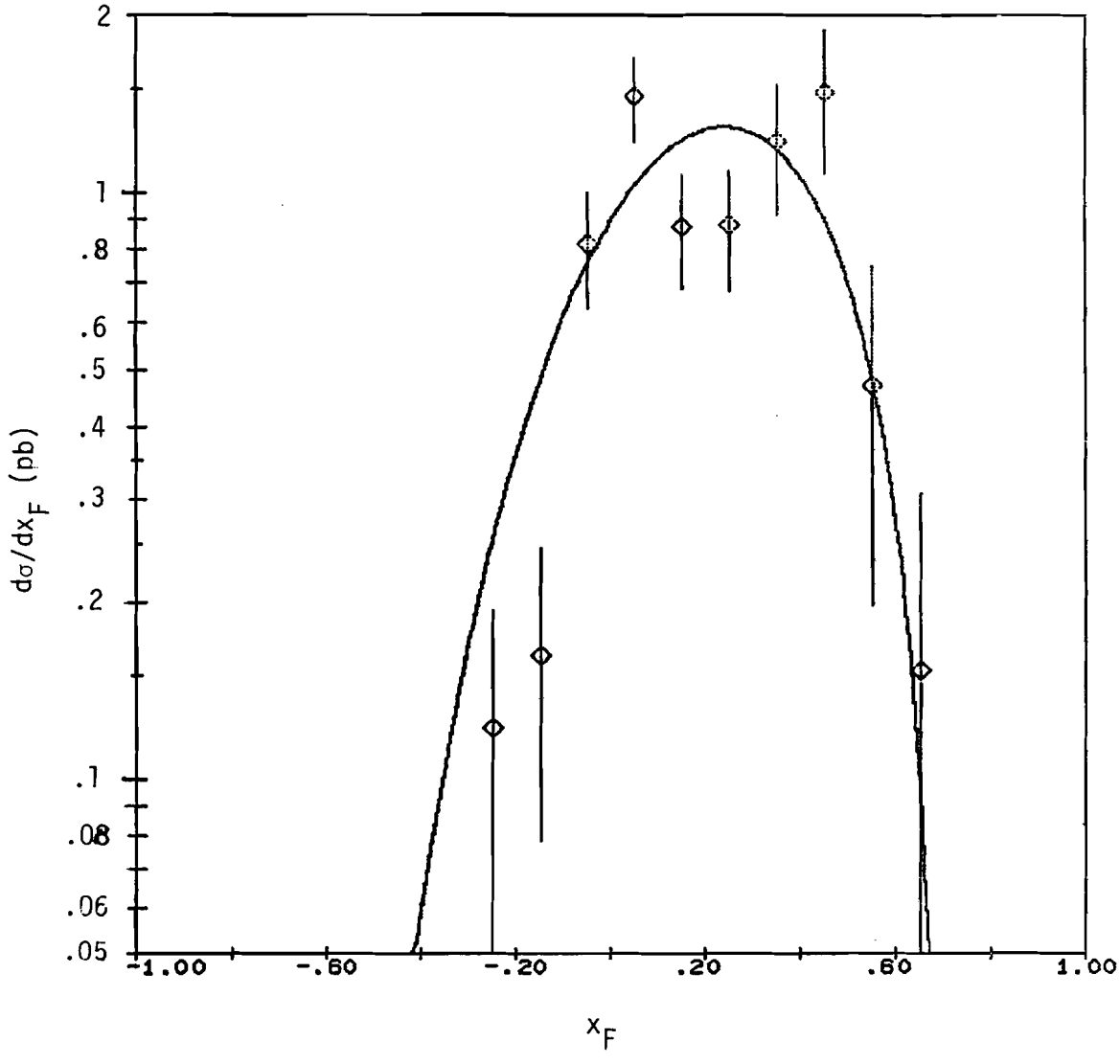
2
1
.8
.6
.5
.4
.3
.2
.1
.08
.06
.05
dσ/dx_F (pb)
-1.00
-.60
-.20
.20
.60
1.00
x_F

Figure 61.— A plot of $d\sigma/dx_F$ comparing NA10's data with the prediction of the Drell-Yan model for $M>11$ GeV/c^2. The Drell-Yan model prediction incorporates QCD leading log scaling violations and uses the world average pion structure function.

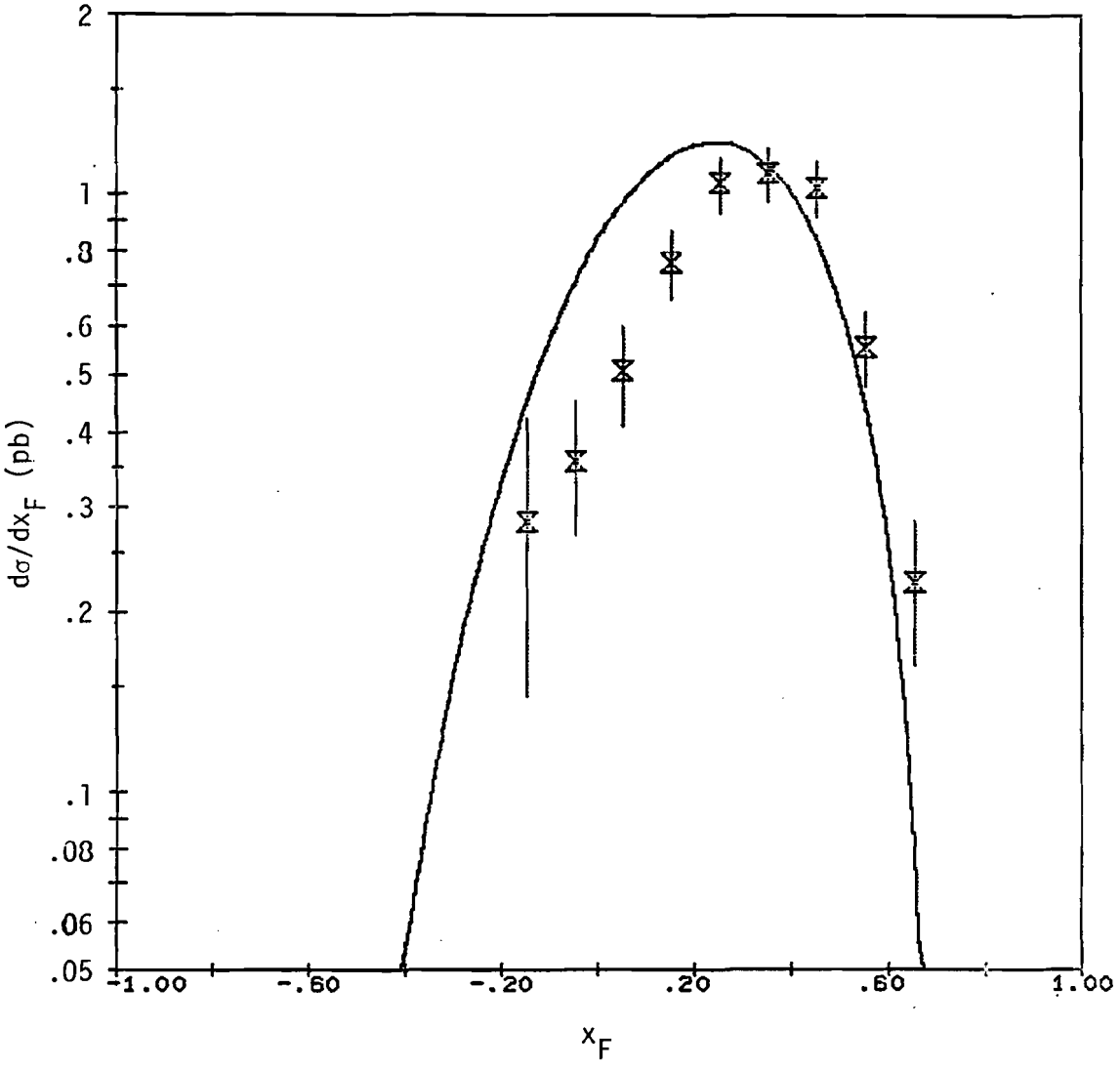
2
1
.8
.6
.5
.4
.3
.2
.1
.08
.06
.05
dσ/dx_F (pb)
-1.00
-.60
-.20
.20
.60
1.00
x_F

Figure 62.— A plot of $(1/p_T)(d\sigma/dp_T)$ comparing our data with our fit in the mass range 4.5 GeV/c^2<M<8.5 GeV/c^2.

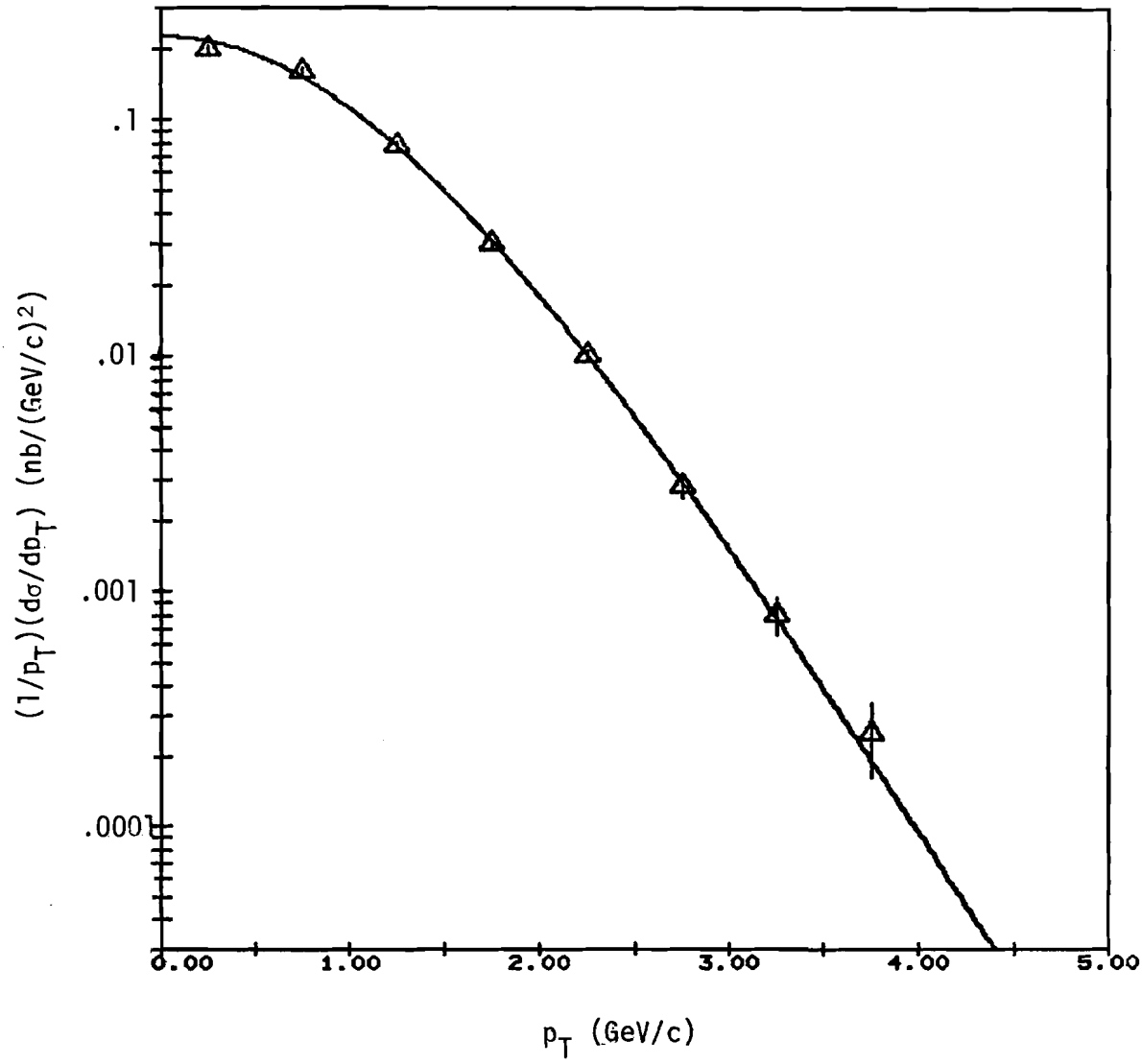
.1
.01
.001
.0001
0.00
1.00
2.00
3.00
4.00
5.00
$(1/p_T)(d\sigma/dp_T)$ (nb/(GeV/c)^2)
p_T (GeV/c)

Figure 63.— A plot of our data for $(1/p_T)(d\sigma/dp_T)$ in several mass ranges.

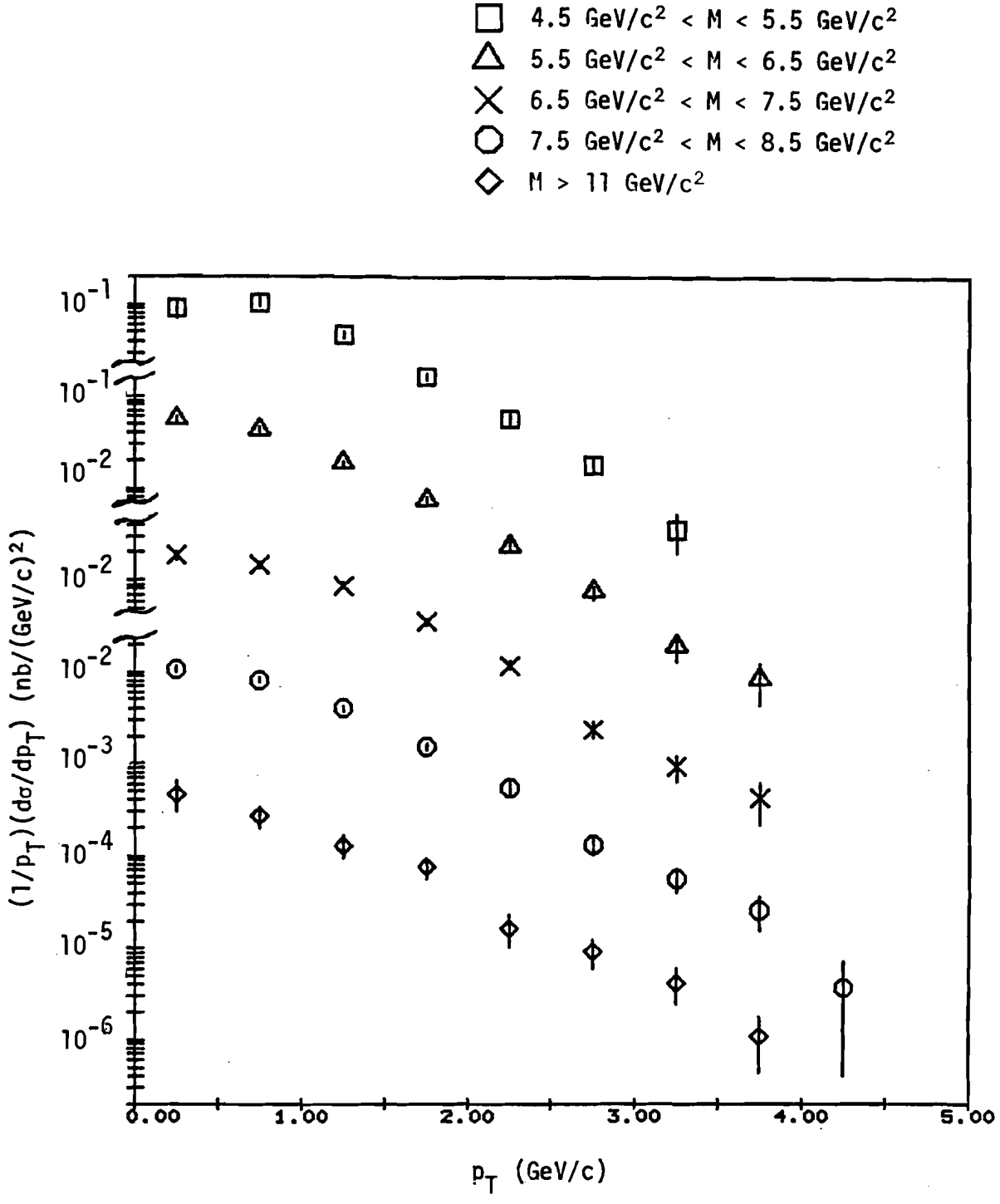
4.5 GeV/c² < M < 5.5 GeV/c²
5.5 GeV/c² < M < 6.5 GeV/c²
6.5 GeV/c² < M < 7.5 GeV/c²
7.5 GeV/c² < M < 8.5 GeV/c²
M > 11 GeV/c²
(1/p_T)(dσ/dp_T) (nb/(GeV/c)²)
10^-1
10^-1
10^-2
10^-2
10^-2
10^-3
10^-4
10^-5
10^-6
0.00
1.00
2.00
3.00
4.00
5.00
p_T (GeV/c)

Figure 64.— $<p_T>$ (bottom row) and $<p_T^2>$ (top row) as a function of mass. The horizontal error bars show the mass interval over which the cross section has been integrated. The vertical error bars are located at the mean mass in the interval.

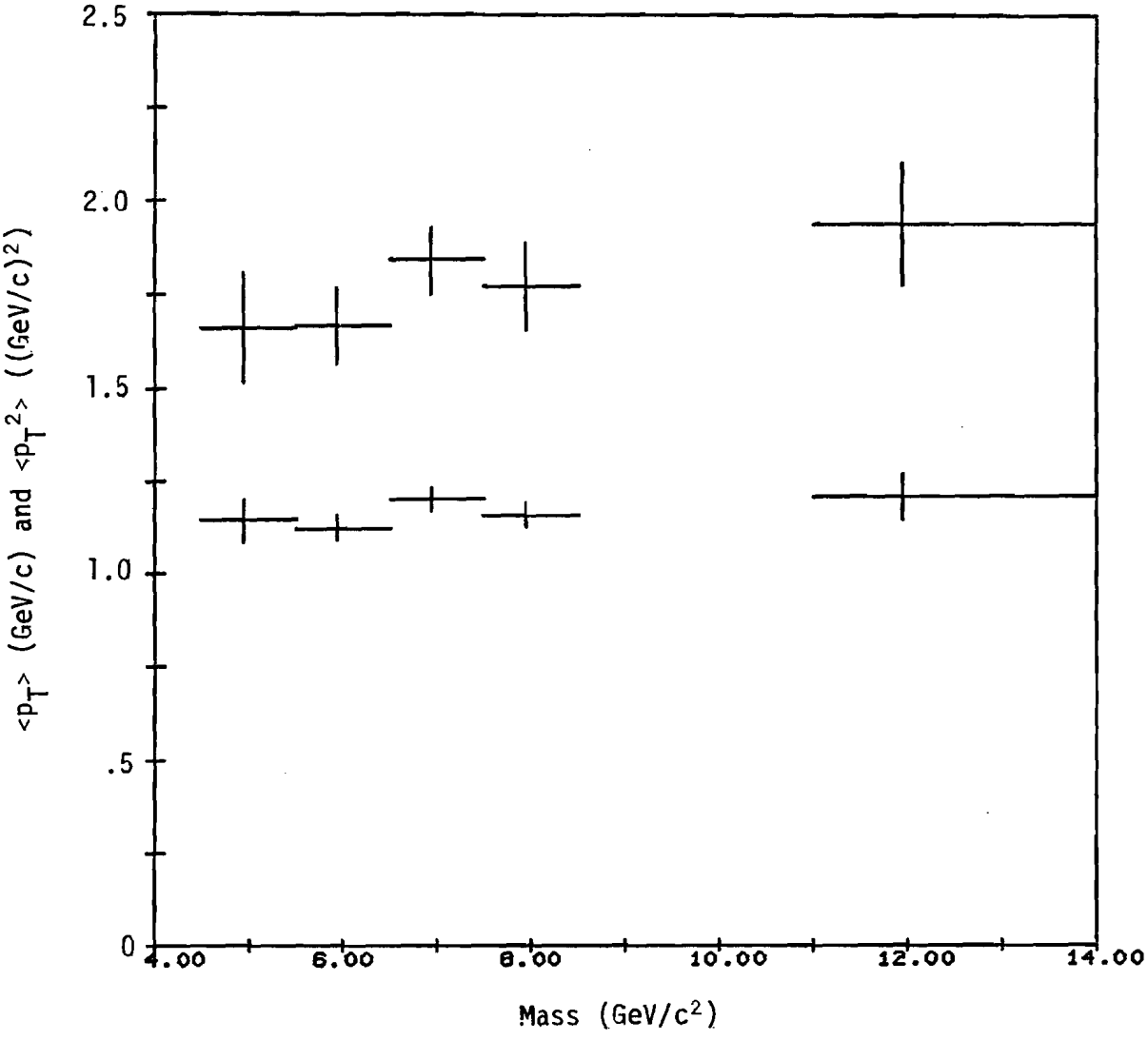
2.5
2.0
1.5
1.0
.5
0
4.00
6.00
8.00
10.00
12.00
14.00
<p_T> (GeV/c) and <p_T^2> ((GeV/c)^2)
Mass (GeV/c^2)

Figure 65.— The distribution of the square of the largest cut generalized coordinate, η^2, encountered during track-finding for positive tracks.

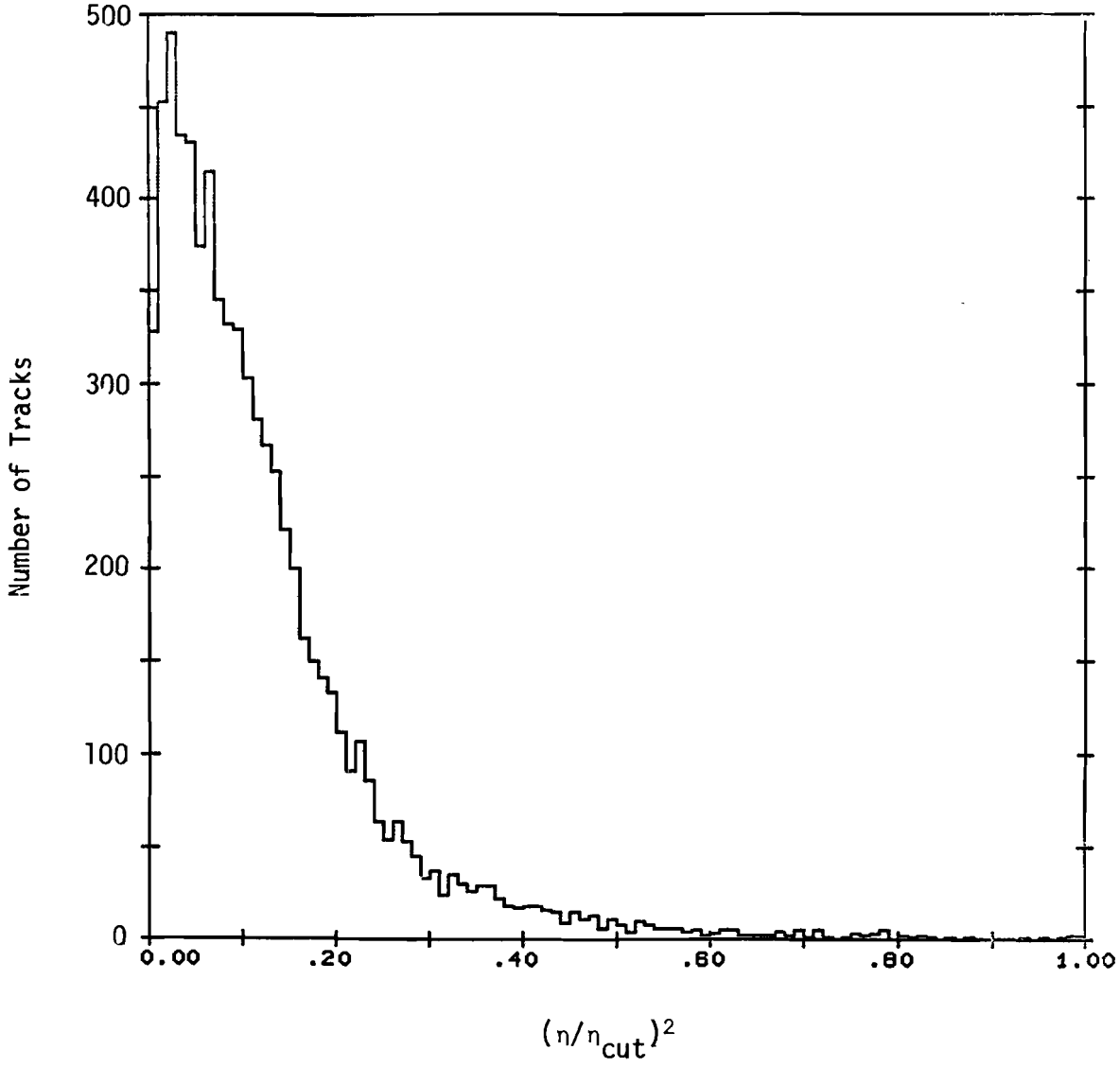
500
400
300
200
100
0
Number of Tracks
0.00
.20
.40
.60
.80
1.00
$(n/n_{cut})^2$

Figure 66.— The distribution of the square of the largest cut generalized coordinate, η^2, encountered during track-finding for negative tracks.

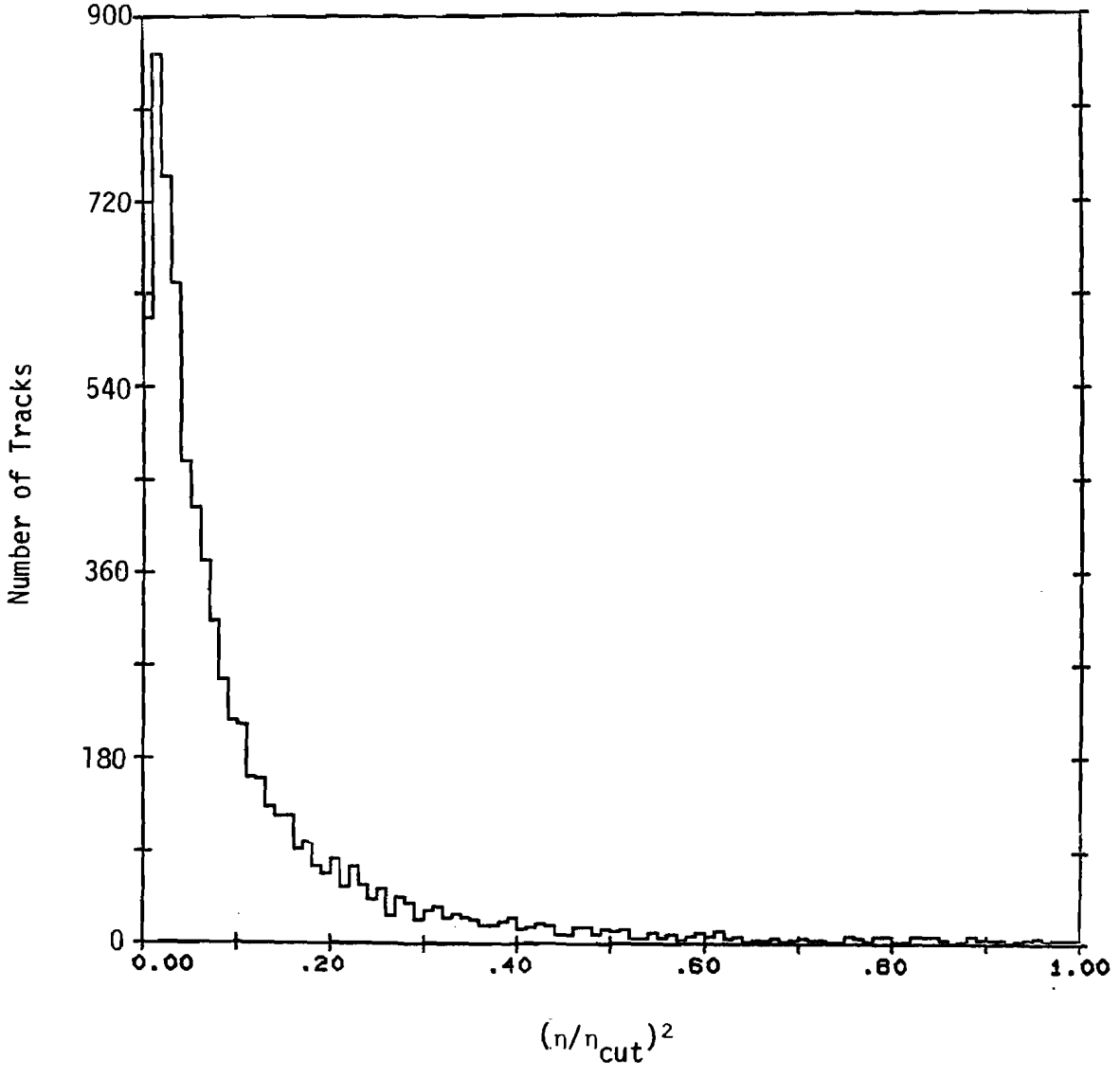
900
720
540
360
180
0
Number of Tracks
0.00
.20
.40
.60
.80
1.00
$(n/n_{cut})^2$

Figure 67.— A comparison of the three different parameterizations of the composite nucleon structure function, $G(x_2)$.

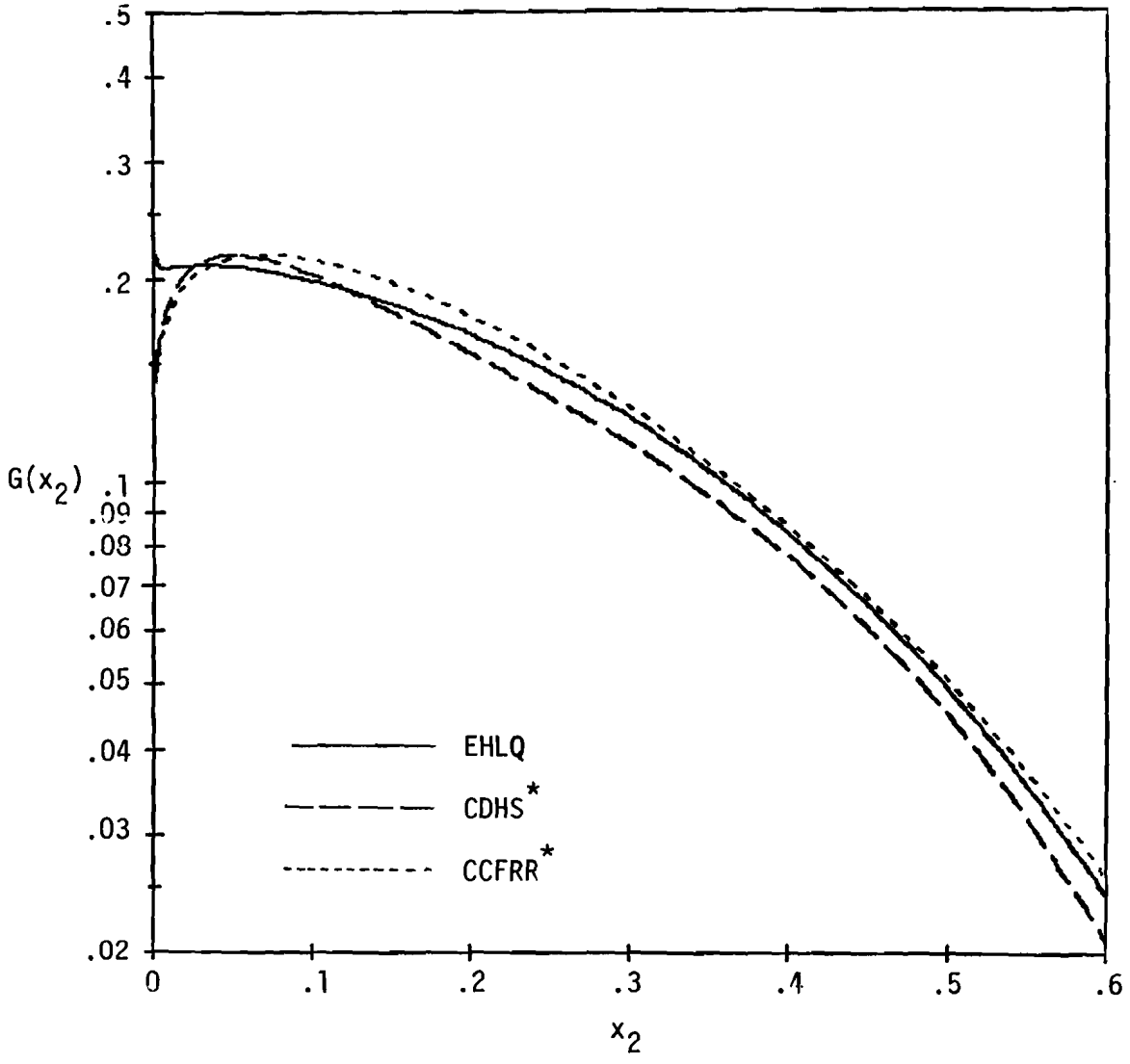

* As parameterized by NA10[36]

Figure 68.— A comparison of the three different parameterizations of the composite nucleon structure function, $H(x_2)$.

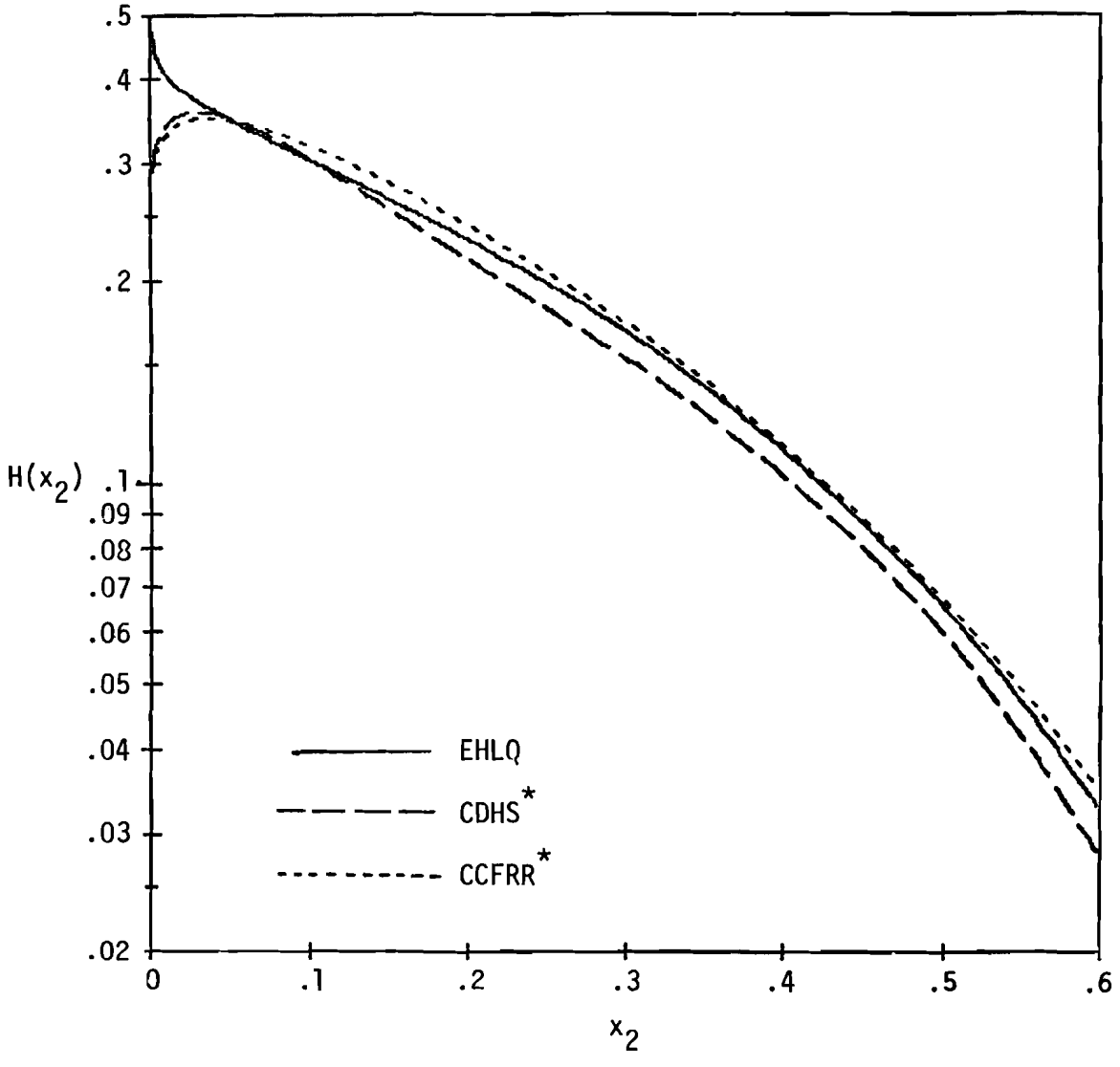

* As parameterized by NA10[36]